ISOLATION AND CHARACTERIZATION OF LOST COPPER AND MOLYBDENUM PARTICLES IN THE FLOTATION TAILINGS OF KENNECOTT COPPER PORPHYRY ORES

by

Tsend-Ayush Tserendavga

A dissertation submitted to the faculty of
The University of Utah
in partial fulfillment of the requirements for the degree of

Doctor of Philosophy

Department of Metallurgical Engineering

The University of Utah

May 2015

The University of Utah Graduate School

STATEMENT OF DISSERTATION APPROVAL

The dissertation of **Tsend-Ayush Tserendavga**

has been approved by the following supervisory committee members:

Jan D. Miller	, Chair	**01/08/2015** Date Approved
Chen Luh-Lin	, Member	**01/08/2015** Date Approved
Michael Nelson	, Member	**01/08/2015** Date Approved
Raj Rajamani	, Member	**01/08/2015** Date Approved
Sivaraman Guruswamy	, Member	**01/08/2015** Date Approved

and by **Manoranjan Misra** , Chair/Dean of

the Department/College/School of **Metallurgical Engineering**

and by David B. Kieda, Dean of The Graduate School.

ABSTRACT

The importance of flotation separation has long been, and continues to be, an important technology for the mining industry, especially to metallurgical engineers. However, the flotation process is quite complex and expensive, in addition to being influenced by many variables. Understanding the variables affecting flotation efficiency and how valuable minerals are lost to the tailings gives metallurgists an advantage in their attempts to increase efficiency by designing operations to target the areas of greatest potential value. A successful, accurate evaluation of lost minerals in the tailings and appropriate solutions to improve flotation efficiency can save millions of dollars in the effective utilization of our mineral resources.

In this dissertation research, an attempt has been made to understand the reasons for the loss of valuable mineral particles in the tailings from Kennecott Utah Copper ores. Possibilities include liberation, particle aggregation (slime coating) and surface chemistry issues associated with the flotation separation. This research generally consisted of three main aspects. The first part involved laboratory flotation experiments and factors, which affect the flotation efficiency. Results of flotation testing are reported that several factors such as mineral exposure/liberation and slime coating and surface oxidation strongly affect the flotation efficiency. The second part of this dissertation research was to develop a rapid scan dual energy (DE) methodology using 2D radiography to identify, isolate, and

prepare lost sulfide mineral particles with the advantages of simple sample preparatıon, short analysis time, statistically reliable accuracy and confident identification. The third part of this dissertation research was concerned with detailed characterization of lost particles including such factors as liberation, slime coating, and surface chemistry characteristics using advanced analytical techniques and instruments.

Based on the results from characterization, the extent to which these factors contribute to the loss of sulfide mineral particles in the tailings were determined.

TABLE OF CONTENTS

LIST OF TABLES

Tables

LIST OF FIGURES

Figures

LIST OF ABBREVIATIONS

DE	Dual Energy
FLS	FLSmidth USA, Inc
GDP	Gross Domestic Product
HRXMT	High Resolution X-ray Micro Tomography
ICSG	The International Copper Study Group
KUC	Kennecott Utah Copper
MLA	Mineral Liberation Analyzer
MRAM	Mineral Resources Authority of Mongolia
NDT	Non-Destructive Technology
QEMSCAN	Quantitative Evaluation of Minerals by Scanning Electron Microscopy
ROI	Region Of Interest
SEM	Scanning Electron Microscopy
SEM-EDS	Scanning Electron Microscopy coupled with Energy Dispersive X-ray Spectroscopy
ToF-SIMS	Time-of-Flight Secondary Ion Mass Spectrometry
USGS	U.S. Geological Survey

XPS	X-ray Photoelectron Spectroscopy
XRF	X-ray Fluorescence

ACKNOWLEDGEMENTS

I would like to express my sincere appreciation to Professor Jan D. Miller, advisor and chair of the supervisory committee, for his help, remarkable support, guidance, and encouragement during the course of this dissertation research. In addition, I would like to thank Dr. Chen-Luh Lin for his advice, knowledge and patience. Thanks are also extended to Dr. Raj Rajamani, Dr. Sivaraman Gurusvamy, and Dr. Michael Nelson, for their positive disposition as members of the supervisory committee and their valuable advice and comments on some aspects of this work.

Thanks are also extended to Phil Thompson, Perry Allen, Lorin Redden, mentors, friends, and alumni of the Department of Metallurgical Engineering, University of Utah, and employees of FLSmidth, USA. In addition, I would like to extend my appreciation to Rio Tinto for providing the research grant for this study. Without their encouragement and insistence to pursue graduate studies in this department, it would have been impossible for me to have the courage to come to the University of Utah and start this beautiful journey.

Lastly, the author would like to express his deepest gratitude and appreciation to his family. Particular thanks are expressed to his wife, Uyansanaa Udanbor, for her love, support, understanding, and tremendous patience.

CHAPTER 1

INTRODUCTION

The more efficient production and use of mineral resources is a major objective in our sustainability efforts. Resource characterization, referred to as geometallurgy, is a critical component for optimization of the mine-to-mill process, and now can be accomplished with advanced instrumentation including, for example, particle size analysis, X-ray fluorescence (XRF), X-ray diffraction (XRD), X-ray photoelectron spectroscopy (XPS), scanning electron microscopy coupled with energy dispersive X-ray spectroscopy (SEM-EDS) which includes quantitative evaluation of minerals by scanning electron microscopy (QEMSCAN) and mineral liberation analyzer (MLA) and high resolution X-ray micro tomography (HRXMT). Geometallurgy relates to the practice of combining geology with metallurgy, to create a spatially or geologically based predictive model for mineral processing plants (Bulled and McInnes, 2005). Sampling and geometallurgical information is important for exploration, deposit evaluation, mine and production planning, analysis of separation, process efficiency, etc. Improved sampling and geometallurgical analysis can save millions of dollars in the effective utilization of our mineral resources (Miller, 2012).

1.1 Copper production worldwide

Copper metal is generally produced from a multistage process, beginning with the mining and concentrating of low-grade ores containing copper sulfide minerals, and followed by smelting and electrolytic refining to produce a pure copper cathode.

The U.S. Geological Survey (USGS) provides information to the public and to policy-makers concerning the current use and flow of minerals and materials in the world economy. According to data compiled by the USGS (2012), world mine production of copper was 16.5 million metric tons (mt) in 2011; world reserves are estimated to be 540 mt, or 36 years at the 2011 rate of production. In recent times, 20 countries have produced approximately 87 % of the world copper production, which is displayed in Figure 1.1. World copper production was dominated by Chile and the United States for several decades and now increasing contributions have come from Peru, China, and Indonesia over the past two decades.

In March 2014, The International Copper Study Group (ICSG, 2014) released the 2014 Statistical Yearbook, which showed world copper production and consumption and revealing that the trends in global refined copper consumption are progressing at an alarming state. The outlook for copper demand is greatly focused on China, where copper consumption will grow as a consequence of the overall economic growth of China. For example, by 2025, one billion people are projected to live in Chinese urban areas and 221 Chinese cities will have been built (Mckinsey Global Institute, March 2009). Along with these massive increases, increased demand will be seen in buildings and infrastructure. It means that one billion Chinese will have become consumers, salaries will have increased, and domestic consumption will continue growing faster than the GDP. More consumers,

means more demand for: cars, appliances, garments, electronics, buildings and infrastructure. In other words, what does it all mean? More copper will be needed.

Industrial production is not keeping up with copper consumption and recent indications suggest that the estimates in Chinese consumption are very conservative. It now appears that in the next 25 years, the world will need to produce as much copper as has been produced in the history of humanity. Figure 1.2 presents evidence of world copper demand compiled by ICSG between 1900 and 2030. Copper consumption expanded at an annual pace of 10.1%. Surprisingly strong Chinese demand is prompting investors to rethink their dour predictions for copper demand, but this demand is not the only major factor to consider in the outlook for copper. The world is also beginning to feel the impact of supply challenges. When it comes to the production of copper, the industry is experiencing difficulties from various aspects of the production cycle:

- Discoveries of high grade deposits are less frequent;
- More underground mines are producing copper, at a smaller output capacity than open pits;
- There are greater country risks and infrastructure challenges (remote locations);
- Average grades of the ore bodies are declining;
- Funding for exploration is inadequate.

Figure 1.3 shows the distribution of known copper deposits of the world based on the ICSG (2012) world copper factbook. Porphyry copper deposits are the world's most important source of copper and molybdenum, and can contain major quantities of gold, silver and tin, with some porphyry copper deposits having by-products of platinum, palladium and tungsten. Approximately 60% of the world's copper and 95% of the

world's molybdenum is sourced from porphyry copper deposits (SolGold annual report, 2013). Porphyry copper deposits are copper ore bodies that are associated with porphyritic intrusive rocks and the fluids that accompany them during the transition and cooling of magma to rock. According to SNL metals economic group data (2013), 100 significant copper discoveries have been reported so far in the 1998-2012 period, containing almost 395 million tons of copper.

Benefiting from the largest share of the discovery-oriented exploration budgets over this period, Latin America hosts more than half of the discovered copper, followed distantly by North America, Africa, Asia, Australia-Pacific, and Europe. Overall, the industry found more copper in these significant discoveries than it produced; however, the economic viability of new resources is influenced by factors such as location and politics, capital and operating costs, and market conditions that inevitably reduce the amount of copper that reaches production. To date, only about one-tenth of the copper in these 100 discoveries has been converted to reserves with only 15 deposits having reached production. According to the SNL-Metals economic group annual report (2013), copper discoveries in reserves, resources, and past production in major copper discoveries by country during 1999-2010 are presented in Figure 1.4.

1.2 Mongolian copper production

One promising location for copper production is in Mongolia, in the South Gobi Desert, east of the Omnogovi province, where the Oyu Tolgoi deposit is located, one of the world's largest and richest copper porphyry deposits. Commercial operations began in mid-2013 and Oyu Tolgoi's open pit is now operating at full capacity under management

by Rio Tinto. In 2013, Oyu Tolgoi produced 77 thousand tons of copper and 157 thousand ounces of gold (Rio Tinto, 2013). Discussion of Mongolian copper production is included because the dissertation research was supported by Rio Tinto. Mongolia is a landlocked country in East and Central Asia, a fledgling democracy of just over 20 years old, bordered by Russia and China. When Mongolia opened its doors to foreign investment, major mining companies accepted the invitation and the incredible geological riches buried beneath the soil became immediately apparent. Despite this influx, the country's vast mineral resources remain largely unexplored and undeveloped. Mongolia currently ranks among the top 10 resource-rich nations in the world. In Mongolia, the mining sector plays a key role in industry and for the last few years, its output has been driving the country's economy. The mining sector's share in the GDP reached approximately 29.0 % in 2011 (MNSO, 2012). According to the Mongolian National Statistical Organization (NSO) monthly report (2012), mineral exports accounted for 89 % of the total exports. The largest exported product was coal, accounting for 43.4 %, followed by copper concentrate (19.1 %), crude oil (7.7 %) and gold (2.8 %). In terms of major destination countries of export, China imported 92.6 % of the total exports from Mongolia, followed by Russia (1.8 %). The real quantity of Mongolia's mineral resources cannot yet be known. Mongolia's vast territory has a great potential to hold rich mineral deposits, including gold, copper, coal, fluorspar, silver, and uranium. Only 24.8% of the Mongolian territory has been covered by general mineral exploration. There are over 8,000 individual mineral deposits in Mongolia, containing a wealth of over 440 different minerals. Of these, around 600 deposits and outcrops have been fully explored and their extent determined. These include over 180 gold deposits, 6 copper deposits, a lead

deposit, 5 tin deposits, 10 iron deposits, 4 silver deposits, 42 deposits of brown and coking coal, 42 fluorspar deposits, 12 salt and 10 sodium sulfate deposits, 6 semiprecious stone deposits, 9 crystal deposits and over 200 deposits of minerals used in the production of construction materials, as well as a wealth of rare-earth metals. By 2011, well over 200 deposits were already being exploited (MRAM, 2011). Figure 1.5 presents the location of the largest copper and other mineral deposits mapped by the mineral resources authority of Mongolia (MRAM).

Rio Tinto is a leading global mining and metals company, involved in every stage of mineral and metal production, and is applying international best practices to the Oyu tolgoi project. Rio Tinto is a major shareholder in the Oyu Tolgoi project. On October 6, 2009, Rio Tinto signed a long-term, comprehensive Investment Agreement with the government of Mongolia for the construction and operation of the Oyu Tolgoi copper-gold mining complex. The agreement creates a partnership between the Mongolian government, which acquired a 34% interest in the project, and Turquoise Hill Resources, which retained a controlling 66% interest in Oyu Tolgoi. Global miner Rio Tinto, which joined Turquoise Hill Resources as a strategic partner in October 2006, is managing the development of Oyu Tolgoi. This includes world-class health and safety standards and a commitment to sustainable development and operational excellence. The Oyu Tolgoi project is the largest financial undertaking in Mongolia's history, and working in partnership with the government of Mongolia, Rio Tinto has striven to ensure the proper training and preparation of the Mongolian workforce with the goal of developing a strong workforce for Mongolia’s future mining industry. Participants are also given a wide range of skills that will build and support a diverse economy. All of the copper projects

and operations of Rio Tinto are depicted in Figure 1.6. Rio Tinto Copper group has operating assets around the world - Kennecott, Oyu Tolgoi, Escondida and Grasberg – and two world-class greenfield projects, Resolution and La Grange. The general characteristics of alteration, mineralization, and geological settling of the Kennecott Bingham Canyon deposit and the Oyu Tolgoi deposit are quite similar and froth flotation is the main method of separating copper minerals from gangue for both operations.

1.3 Significance of flotation

Froth flotation is the most common technique used in beneficiation of complex-structured, valuable sulfide minerals such as chalcopyrite, galena, sphalerite and silver. The importance of froth flotation has long been, and continues to be, an important aspect of the mining industry, especially for metallurgical engineers. The flotation of sulfide minerals, such as chalcopyrite ($CuFeS_2$), chalcocite (Cu_2S), covellite (CuS), pyrite (FeS_2), galena (PbS) and sphalerite (ZnS), has been practiced successfully for over 100 years (Fuerstenau, 2007). The trend in the copper mining industry of today is that the total recovery of copper and associated metals in the entire process of copper production must be optimized. Optimum sulfide mineral recoveries have always been a problem because there are continuous changes in the properties of the plant feed. Tabulations of operating data also reveal some of the technical problems associated with the flotation of sulfide ores. For example, the average recovery of copper in the world flotation plants was reported to be only 82%, and only 58% recovery of the associated molybdenum (Herrera-Urbina, 2003). For meaningful improvement, new and better technology must be developed to increase recovery. During normal operations, sulfide mineral flotation is

generally satisfactory. However, the flotation response changes due to variations in the feed characteristics in an operating plant. These result in fluctuations in the concentrate grade and sometimes the recovery will be low with a significant loss of base and precious metals. Froth flotation is affected by many parameters that are beyond the control of a mineral processing engineer. As is well known, liberation of the valuable minerals is necessary for successful flotation separations. Beyond liberation, process variables such as slime coating, surface oxidation, pH, conditioning time, type of reagents (collectors, frothers, depressants, activators) and also their dosage can significantly influence the success of the flotation separation, which in turn, determines the grade and recovery of the metal in the concentrate. These factors must be considered in an attempt to determine their significance on the separation efficiency. In particular, the identification and characterization of lost (trace) particles in the flotation tailings of a copper porphyry ore must be studied. In particular, in this dissertation research the identification and characterization of chalcopyrite and molybdenite particles lost to the tailings during the flotation of Bingham Canyon ore will be studied. Babcock et al. (1997) describe the Bingham Canyon deposit as a classic porphyry copper deposit exhibiting concentric zones of alteration and mineralization.

1.4 Flotation at the Copperton concentrator

Kennecott Utah Copper (KUC), a wholly owned subsidiary of Rio Tinto, operates the Bingham Canyon mine, one of the world's largest open pit copper mines. The mine and associated Copperton concentrator are located approximately 26 miles southwest of Salt Lake City, Utah, in the eastern foothills of the Oquirrh mountain range near the city of

Copperton. The deposit is notable for its size, containing premining reserves of nearly 3 billion tons of ore at 0.67% copper (USGS, 2011). Nested within the copper ore body are overlapping zones of molybdenum, gold and silver containing 0.1% molybdenite (MoS_2), 0.3 g/t gold and 1.5 g/t silver (Triffett and Bradshaw, 2008).

In general, the main sulfide minerals are chalcopyrite, bornite, molybdenite, and pyrite. The major gangue mineral is quartz. According to Babbock et al. (1997) and Nelson (2007), the Bingham Canyon deposit contains a number of ore types that are classified based initially on lithology and on processing characteristics. The quantity of ore processed through the concentrator each day requires that several ore types will be treated at once, in a blend. The processing characteristics of individual ore types have been extensively modeled and these are arithmetically combined to estimate the expected performance of blends in the production planning process.

A brief plant description (Triffett and Bradshaw, 2008) is presented in the following paragraphs in order to understand the overall process and the relevance to this dissertation research. Processing of the ore is performed on-site using crushing, grinding, and flotation to recover copper and molybdenum concentrates. A simplified process flow diagram of KUC's Copperton concentrator is provided in Figure 1.7.

The run of mine ore is crushed with a gyratory crusher and then reduced to less than 100 mesh (150 μm) by wet grinding using semi-autogenous grinding (SAG) mills and ball mills. The grinding operation consists of three parallel SAG mills, and two ball mills corresponding to each SAG mill. The SAG mill discharge is screened on vibrating screens and the coarse material from the screen is sent back for crushing in a cone crusher (MP1000). The product of the cone crusher is returned to the SAG mill for further

grinding. The ball mill ground product is classified in cyclones of 26 inches for achieving a product size of 80% passing 100 mesh (150 μm). The cyclone overflow from the grinding circuit is combined and distributed equally to 4 parallel rougher-scavenger flotation lines containing 11 Wemco flotation cells (3000 ft^3/cell) per line. The rougher-scavenger residence time is approximately 15 minutes. The rougher concentrate is reground to 74 % passing 200 mesh (74 μm) and is further processed in a cleaner circuit with conventional mechanical cells. The cleaner circuit produces a final bulk concentrate. The bulk concentrate is further sent for separation of copper from molybdenum by depressing the copper minerals using sodium hydrosulfide (NaSH) as a depressant. The average plant recovery is usually between 80 % and 90 % for copper, and molybdenum recovery may range between 65 % and 85 % (Crozier, 1979). Tailings are sent to thickeners for water recovery and the thickened slurry is transported by a 48 inch pipeline to the tailings impoundment area. The copper concentrate is transported by pipeline for filtration. The molybdenum concentrate is filtered, dried and packed in bags at the Copperton site (Zanin et al., 2008).

1.5 Research objectives

The objectives of the dissertation research were to investigate the significance of problems associated with the flotation efficiency for selected KUC ore types. Specifically, the research included the following objectives:

- Evaluation of the flotation response for different ore types;
- Development of a rapid scan methodology using radiography to identify, isolate, and collect lost sulfide mineral particles from the flotation tailings;

- Examination of the liberation and the surface chemistry characteristics of lost particles using advanced analytical techniques such as HRXMT, XPS, SEM, ToF-SIMS and/or QEMSCAN;
- Determination of the extent to which surface chemistry, exposure/liberation and slime coating considerations contribute to the loss of sulfide mineral particles in the tailings.

Modern instrumentation and equipment were used for characterization of feed and flotation products. Based on the most significant limitation to flotation efficiency, future flotation experiments should be carried out to evaluate possible alternatives for improved flotation recovery of copper (Cu) and molybdenum (Mo).

The variability of the feed quality delivered to flotation plants in mining operations can provide challenges to the operational staff in attempting to achieve satisfactory recovery and grade efficiency. When faced with variables or difficult ores, plant operators are often required to implement operational parameter changes to maintain flotation efficiency. This research was aimed at improving the understanding of the factors affecting the flotation efficiency of copper and molybdenum minerals from porphyry copper ores and providing some possible solutions to these challenges. Specifically, the identification and characterization of lost chalcopyrite and molybdenite particles using a dual energy rapid scan radiography method for the analysis of flotation tailings was considered. Of course, working with tailings is never easy. Minor or trace concentrations of valuable elements or minerals means that sample collection and integrity become one of the major concerns in any project relating to the tailings. Research findings can be used for many applications such as fast geometallurgical

analysis, including identification of mineral zones from drill core samples and the search and isolation of trace mineral particles from the feed and tailings streams. Preliminary results verified that dual energy radiography works well to fulfill this function.

1.6 Dissertation organization

After the introduction in Chapter 1 and the literature review in Chapter 2, the dissertation research consists of three main aspects. The first part of Chapter 3 involves laboratory flotation experiments and variables that affect the flotation separation efficiencies are discussed with the aim of increasing copper and molybdenum flotation efficiencies. Later in Chapter 3, research results from batch flotation testing are reported regarding the loss of sulfide particles such as chalcopyrite and molybdenite that exists in copper flotation circuits of milling plants that treat porphyry copper ores. Results of rougher flotation conducted for several ore types of KUC are reported. The rougher flotation testing was controlled by changing the grind fineness and slime coating.

The second part of this dissertation research, presented in Chapter 4, was to develop a rapid scan methodology using 2D radiography to identify, isolate, and collect lost sulfide mineral particles in flotation tailings. In Chapter 4, the theory and procedures for rapid scan dual energy (DE) 2D radiography are described for the evaluation and isolation of trace mineral particles from samples at the ppm level. During radiography analysis, the flotation tailings samples are split into narrow size fractions, each size fraction distributed/assembled on projection plates, and then the plates placed in the sample holder of the X-ray instrument for irradiation at two energy levels (dual energy analysis). In this way, for example, more than 40,000 particles, 150x75 μm in size can be

interrogated in less than 15 minutes for identification of particles containing high and medium density mineral phases and their composition can be estimated.

The third part of this dissertation research is presented in Chapter 5 and is concerned with the characterization of lost tailings particles including the liberation and the surface chemistry characteristics of lost particles using advanced techniques such as HRXMT, SEM and XPS. Based on characterization results of advanced instrumentation, the extent to which surface chemistry, mineral exposure/liberation and slime coating contribute to the loss of sulfide mineral particles in the tailings are determined. Detailed results and recommendations will be presented in Chapter 5.

Finally, Chapter 6 presents a summary and general conclusion from research findings regarding the flotation characteristics of the KUC samples and their impact on flotation plant efficiency.

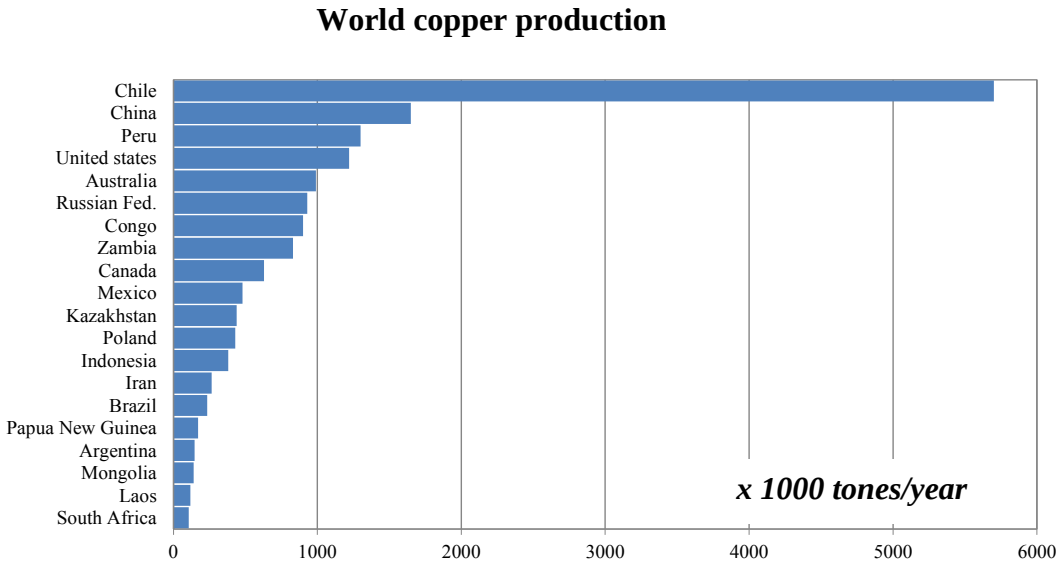

Figure 1.1 World copper production by countries (adapted from ICSG, 2012).

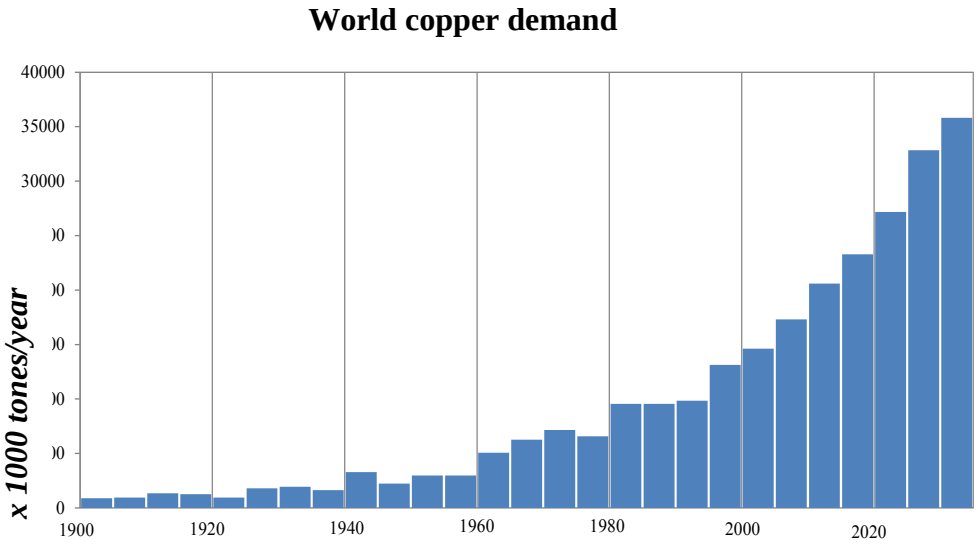

Figure 1.2 The forecast of world copper demand (adapted from ICSG, 2012).

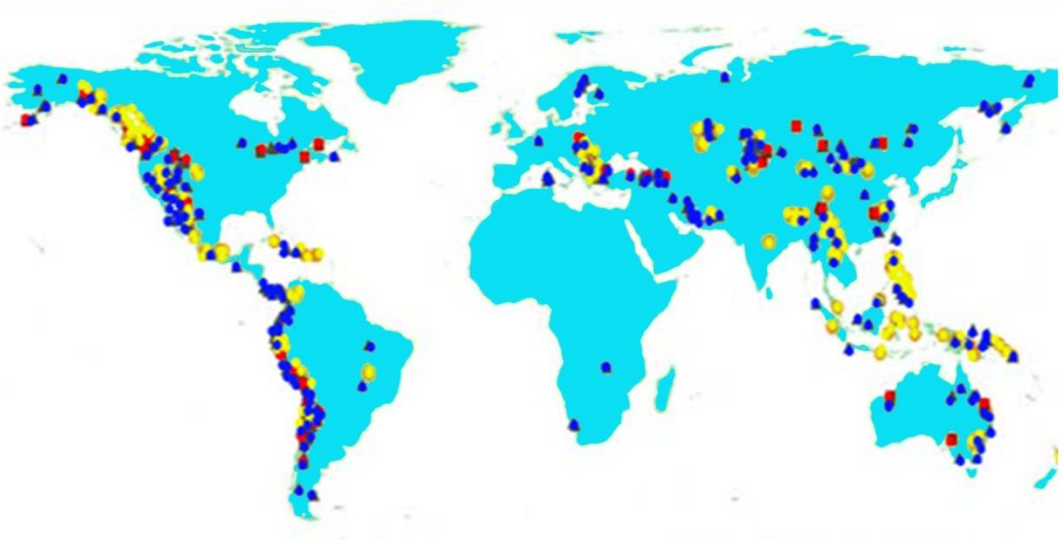

Figure 1.3 Locations of copper porphyry deposits of the world and metallogenic belts. Red indicates Cu-Mo porphyry, blue – Cu porphyry, yellow – Cu-Au porphyry deposits (adapted from USGS, 2008).

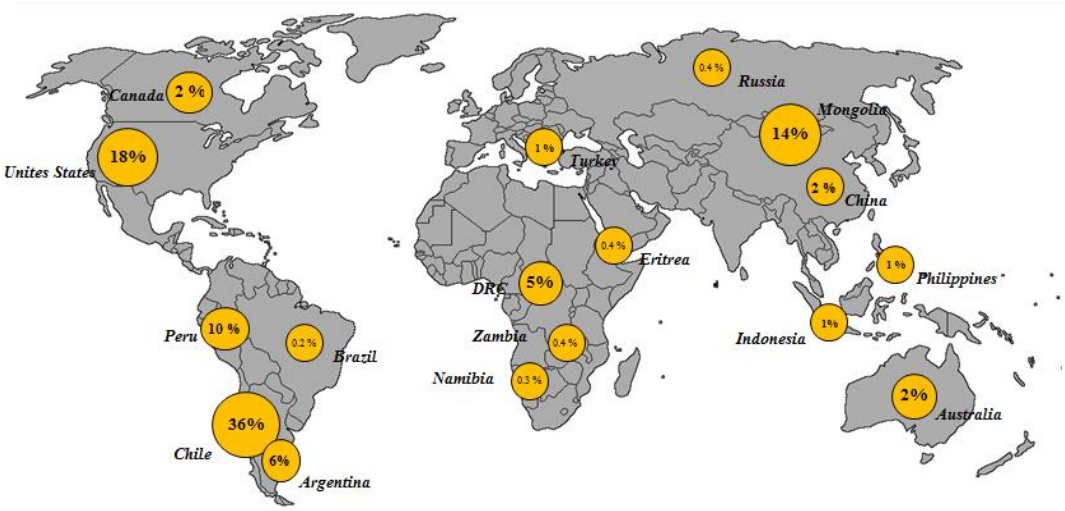

Figure 1.4 Copper in reserves, resources, and past production in major copper discoveries by country, 1999-2010 (adapted from SNL-Metals Economic Group, 2013).

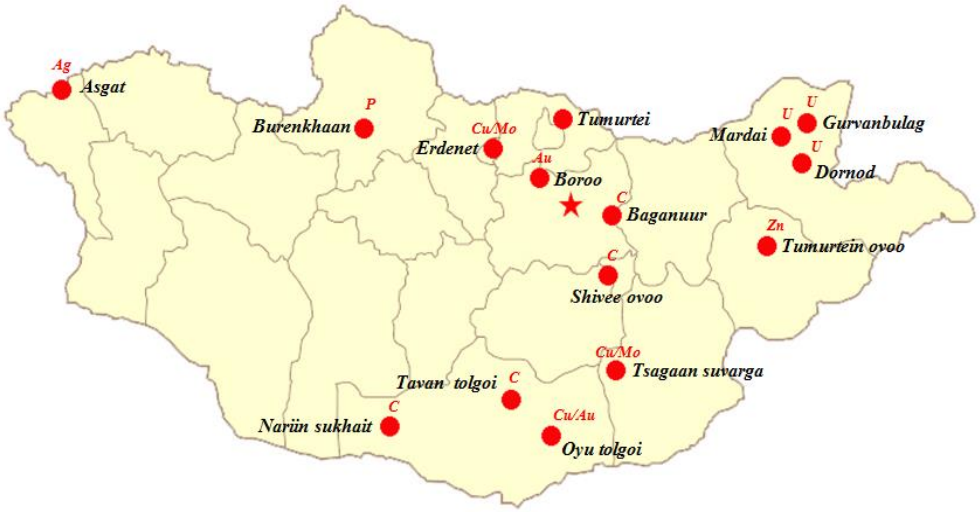

Figure 1.5 Location map of world-scale, large mineral deposits in Mongolia (adapted from MRAM, 2012).

Figure 1.6 Location map of Rio Tinto's copper projects and operations around the world. By-products may include gold, silver and molybdenum. Operations: 1- Escondida; 2 – Grasberg; 3 - Kennecott; 4 - Oyu Tolgoi; Copper projects: 5 - La Grange; 6 –Resolution; 7-Bougainville (adapted from Rio Tinto Annual Report, 2013).

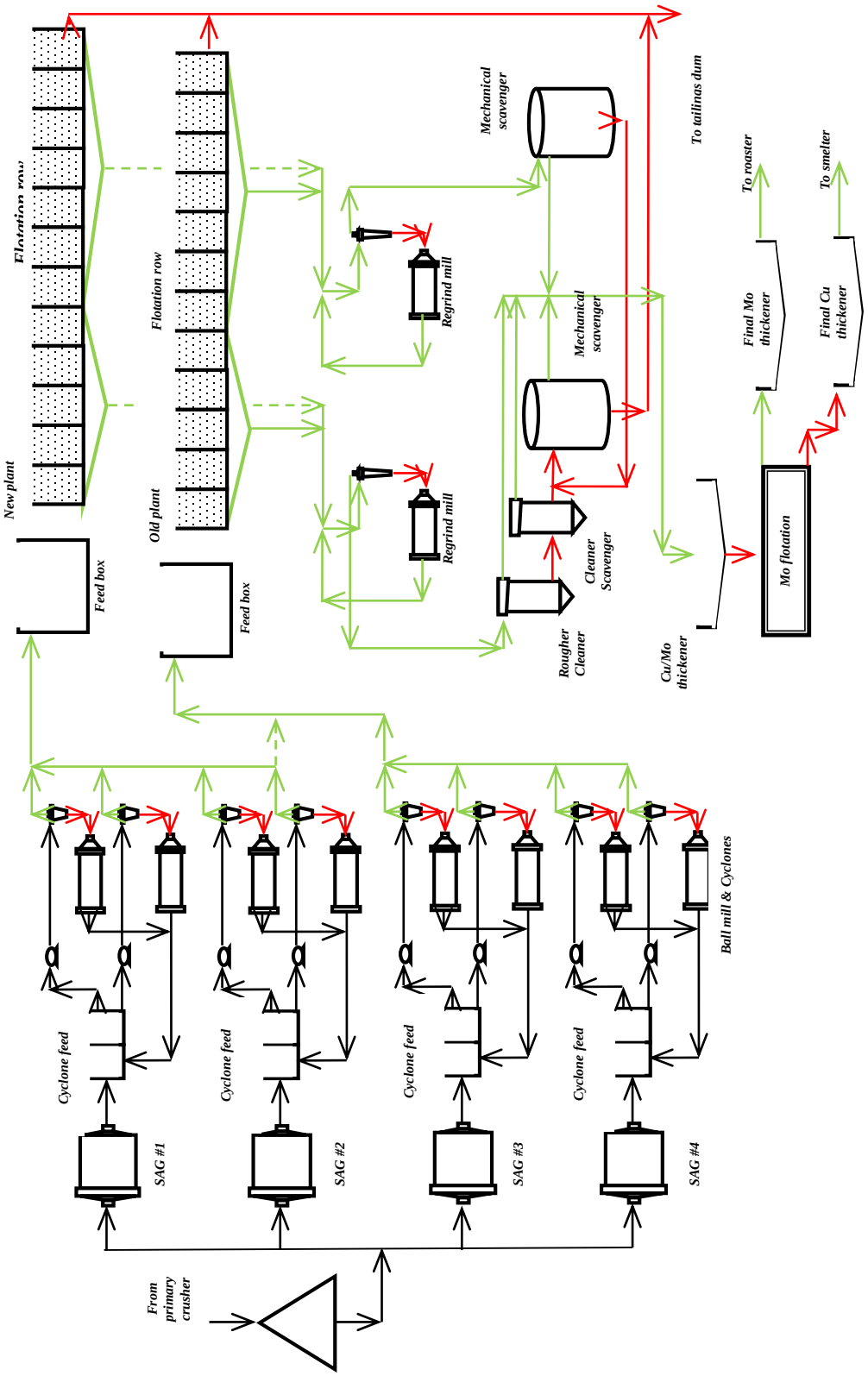

Figure 1.7 Simplified process flow diagram of KUC's Copperton Concentrator (Data source: Kennecott Annual Report, 2012).

CHAPTER 2

FLOTATION OF COPPER-MOLYBDENUM ORES

2.1 Introduction

Froth flotation is a key unit process in the recovery of most of the world's copper, lead, molybdenum, nickel, platinum group elements, silver, and zinc, and in the treatment of certain gold and tin ores. Flotation for the recovery of copper sulfide minerals has long been, and continues to be, of significant importance to the mining industry, especially to metallurgical engineers. Flotation is the preferred method for the recovery of most sulfide minerals. The flotation of sulfide minerals, such as chalcopyrite ($CuFeS_2$), chalcocite (Cu_2S), pyrite (FeS_2), galena (PbS) and sphalerite (ZnS), has been practiced for over 100 years (Fuerstenau, 2005). Bulatovic (2007) reported that copper ores can be divided into the following groups with regard to processing:

- Copper sulfide ores, where the pyrite content can vary from 10% to 90%. Some copper sulfide ores also contain significant quantities of gold and silver. According to mineral composition, these ores can be subdivided into three main groups including (a) copper–gold ore, (b) copper sulfide ore with moderate pyrite content and (c) massive sulfide copper ores;
- Copper porphyry ores are the most abundant copper ores; these ores most often

contain molybdenum, which is recovered as a by-product. More than 60% of the world's copper production and approximately 90 % of the world's molybdenum production comes from copper porphyry ores.

Copper (Cu) and molybdenum (Mo) usually occur as chalcopyrite ($CuFeS_2$) and molybdenite (MoS_2) minerals in copper porphyry ores and are usually associated with pyrite (FeS_2) and silicate gangue minerals. These Cu and Mo sulfide minerals are generally recovered by froth flotation (Fuerstenau and Herrera-Urbina, 1989). During flotation, some amounts of Cu and Mo are lost to tailings streams, as these metals may be entrapped in gangue materials and remain unliberated, may be present as fine slimes, or may report to tailings due to problems in process operations. For example, the average recovery of copper in US flotation plants was reported to be only 82%, with only 50 – 85 % average recovery of the associated molybdenum (Herrera-Urbina, 2003). Huge amounts of such tailings are generated at many copper porphyry mines around the world.

Due to the increased utilization of Cu and Mo in many industries and the rapid depletion of existing ore deposits, development of new deposits will continue to receive further attention (Herrera-Urbina, 2003).

The application of flotation to concentrate valuable minerals is environmentally friendly and economically feasible since generally the ore has been reduced to a liberation size suitable for flotation. However, when the size becomes too fine other challenges, such as surface oxidation and slime coating may affect the flotation separation variables, including collector/frother selections and concentrations, extent of surface modification by attrition or addition of promoters and depressants, among others (Bulatovic, 2007).

Flotation properties of individual copper minerals and associated sulfides such as chalcopyrite, bornite, molybdenite, and pyrite from natural ores differ significantly. These differences are briefly described in some textbooks, for example, in Bulatovic (2007). The mineralogy of the ore, mineral impurities in a crystal structure, variation in crystal structure, other interfering gangue minerals, and the liberation characteristics of individual minerals in a particular ore are some of the factors that influence the efficiency of the flotation separation.

2.2 Reagent schemes in the flotation of copper porphyry ores

The factors which determine a reagent schedule and flow diagram for porphyry copper ores include ore nature and mineralogy, flotation behavior of gangue minerals, what minerals are present, the amount and occurrence of pyrite and the presence of clay in the ore. A typical flow diagram used in the flotation of porphyry copper ores is shown in Figure 2.1. Reagent schemes used for the treatment of porphyry copper ores are relatively simple and usually involve lime as a modifier, xanthate as the primary collector, and a secondary collector that includes dithiophosphates, mercaptans, thionocarbamates and xanthogen formates. The next important issue is separation of the Cu–Mo rougher concentrate. In this research, rougher flotation of Cu-Mo is considered rather than the separation of Mo from the copper rougher concentrate.

2.3 Factors affecting the flotation recovery of copper porphyry ore

Due to the many variables that influence flotation and affect the process of mineralization of air bubbles, considerable attention has been given to the development

of sulfide flotation technology in the past century (Maksimov and Emeljanov, 1983; Xu and Changlian, 1985; Szatkowski and Freyberger, 1985a,b; Vanangamudi and Rao, 1986; Lazic and Calic, 2000; Brozek and Mlynarczykowska, 2006). Unfortunately, because froth flotation is a complex engineering system, incorporating several highly interrelated parameters such as chemistry, operational performance and equipment, (see Figure 2.2), it is a difficult process to study. Changes in one setting will inevitably cause a demand for changes in other parts of the system. Therefore, isolating the effect of a single factor becomes problematic. For meaningful improvement, new and better technology must be developed to increase the recovery. During recent years, the mining industry has focused on implementing new technologies such as equipment, expert control systems and new chemical reagents in order to increase the operational performance of the flotation circuits. Optimum sulfide mineral recoveries have always been a problem because there are continuous changes in the properties of plant feed. Of course, the development of new ore deposits generally requires special attention to establish appropriate reagent schedules and operating conditions.

The focus of this dissertation will be on the operational features such as characterization of lost particles in the tailings, including mineral exposure/liberation, slime coating/aggregation, and surface chemistry issues. A better understanding of these factors is an important key to achieving improved flotation recovery (Roman, 2008). The process of flotation is a sequence of several steps, some of which are done in the ore preparation stage and some in the flotation cell itself (Harris, 1976; Klimpel et al., 1986). From a survey of the literature, it has been observed that following sequence is followed for the processing of copper ore:

- Liberation of desired material (using ore preparation methods such as crushing and grinding);
- Adsorption of reagents on particle surfaces through conditioning (conditioning of the slurry done with appropriate reagents);
- Generation of air bubbles (injection of finely disseminated air bubbles through the slurry);
- Collision of particles with bubbles and their attachment;
- Generation of an air-water-mineral aggregation in the presence of reagents;
- Transport of the air-water-mineral aggregate to the surface.

Laboratory experimental results are used to evaluate particle characteristics and their response to flotation. These tests are also useful in improving the existing process in operating plants through evaluation of possible changes, including reagent schedules, aeration, cleaning steps and regrinding (Roman, 2008).

Leja (1982), Shirley and Sutulov (1985), Raghavan and Hsu (1984), Triffett and Bradshaw (2008), Triffett et al. (2008), and Zanin et al. (2009) summarized a number of difficulties encountered in the treatment of Cu and Mo minerals in the flotation process and these difficulties can be grouped under the following headings:

- Effect of mineral exposure and liberation (especially if there is a high degree of interlocking and fine dissemination of the valuable sulfides within the gangue matrix);
- Effect of particle interactions (the coexistence and attachment of hydrophilic clay minerals producing interference, and coexistence of hydrophobic gangue minerals such as talc, graphite, and other carbonaceous minerals);

- Effect of surface and pulp chemistry (surface oxidation, coexistence of sulfide and oxidized minerals such as oxides, carbonates, and sulfates, and the effect of dissolved ions and residual reagents).

Few reports are available addressing all of the above limiting characteristics on the recovery of sulfide minerals. In the present study, attempts are made to understand the significance of mineral exposure/liberation, slime coating and surface chemistry in the flotation of difficult-to-float ore types from the Bingham Canyon deposit, KUC. These factors will be discussed in more detail in the next sections.

2.3.1 Particle size

Particle size is one of the most important parameters in flotation and its significance in the flotation process was recognized early on (Trahar, 1981). It was generally found that for a particular flotation system there is an optimum particle size range, usually 10–100 μm, where high flotation response and efficiency are observed. Outside this range, recovery drops significantly (King, 1982; Klimpel and Hansen, 1988). The result is a curve between flotation recoveries vs. particle size, resembling an inverted U shape. The particle size range, in turn, affects response to flotation variables. For instance, due to lower mass and inertial force, fine particles exhibit low collision efficiencies. On the other hand, maximum floatability for coarse particle size is determined by the detachment process. There have been many studies conducted to investigate the positive and negative effects caused by fine and coarse particles in flotation efficiency (Santana et al., 2008; Muganda et al., 2011). Triffett et al. (2008) investigated the particle size vs. recovery for molybdenite and copper in the rougher flotation circuit, which are routinely measured on

the weekly production composites at the Copperton plant, KUC. Figure 2.3 presents the average size vs. recoveries of Cu and Mo for the 18 months from April 2005 until October 2006 at the Copperton plant.

As can be seen in Figure 2.3, both metals display a recovery curve according to particle size with the maximum recovery being achieved in the intermediate size fractions and the coarse and fine particles being recovered at a lower rate (Triffett et al., 2008). In addition, Triffett and Bradshaw (2008) found that the recovery of molybdenite peaks in the 38 to 75 μm size range, while the copper recovery is high across a broader range of sizes from 38 to 106 μm. The recovery of molybdenite also drops to a greater extent than the copper in the coarse and fine sizes. Raghavan and Hsu (1984) reported that the effect of particle size on the kinetics of flotation can be explained as follows:

- Theoretically, the larger particles of molybdenite are characterized by a much higher face-to-edge ratio and hence are likely to exhibit better floatability;
- For smaller particles, which possess a lower face-to-edge ratio, the face-to-edge ratio and charge established by the broken bonds on the edges will play a decisive role. Increased particle charge due to smaller particles sizes leads to cohesion, agglomeration and segregation.

2.3.2 Mineral liberation/exposure

The efficiency of sulfide mineral flotation is controlled by another important variable, mineral liberation. Basically, liberation is the release of valuable minerals from waste gangue minerals during comminution and is desired to happen at the coarsest possible particle size. In practice, complete liberation is seldom achieved, even if the ore is ground

to the desired particle size. Of course, some degree of liberation is necessary if separation and concentration are to be achieved in mineral processing operations. The degree of liberation is expressed as the percentage of the mineral occurring as free particles, in relation to the total mineral content, in the particle population. The degree of liberation is typically based on the volume percent of the desired mineral grain in a whole particle. Generally, mineral liberation characteristics are described in several ways:

- *Mineral locking* indicates weight % of the given phase, which is associated with other phases in composite particles;
- *Mineral liberation analysis by particle composition* indicates the weight percentage of a given phase in a given liberation class. For example, the fraction of the mineral in the liberation class, 95-100 %, describes particles composed of 95 weight % of Cu sulfide mineral and 5 weight % of gangue minerals up to liberated particles of 100 % copper sulfide minerals;
- *Mineral exposure analysis* indicates a fraction of grains exposed for a given particle size class.

Since flotation is based on particle surface features, not all locked particles have an equal chance to float. Locked particles that contain 50 % copper sulfide mineral may float very well if the particle surface consists exclusively of the copper sulfide mineral. On the other hand, the opposite may be true and a composite particle containing 80 % copper sulfide may not float at all. The surface composition is more important than the extent of liberation.

Several attempts have been made to quantitatively estimate the degree of liberation as a function of particle size. The foundation for liberation prediction models is the

Andrews-Mika diagram, which describes what type of progeny particles will be generated when a single particle breaks during comminution (King and Schneider, 1998). An example of an Andrews-Mika diagram is illustrated in Figure 2.4.

Models for liberation prediction developed by King and Schneider (1998), Schneider (1995; 2003), Davy (1984), Gay and Latti (2006), Miller and Lin (1988; 2004, Miller et al. (2009), Lin et al. (1987; 2001; 2013) and Goodall et al. (2005) are based on mineral composition and texture analysis.

Basically, these models were developed for binary systems and they may not apply to multiphase ores, and all prediction models rely on 2D polished section measurements and 3D estimations based on stereological correction. In 2D, the degree of mineral liberation is done by two methods: an area method or a linear intercept method (Lin et al., 1987). In either case, the 2D analysis will overestimate the extent of liberation. Figure 2.5 presents the cross section of ore particles classified by mineral composition and exposed area. The flotation of sulfide minerals requires a highly exposed surface area of the minerals to improve the interaction and dispersion of reagents on the mineral surface. Thus, the exposed surface area also has a significant impact on the sulfide recovery by flotation.

In 2D, the exposed surface area can be associated with the perimeter exposed and the area of the mineral on the particle. The combination of these geometrical properties can be used for the calculation of the mineral exposure factor, (MEF), which can be defined as (Roman, 2008):

$$A_i = \sum_{i=1} (A_i P_i / 100n) \tag{1}$$

where n is the total number of particles, A_i is the percent area and P_i is the percent exposed perimeter of the mineral in the particle. The maximum value of MEF corresponds to 100 %, which is equivalent to a fully liberated mineral. For a population of particles, the area and perimeter are calculated for each mineral in each particle by optical microscopy and/or SEM with image analysis software.

There have been several systems developed in the past for mineral liberation analysis (Lin et al 1987; Roman, 2008). However, previous industrial applications of liberation data have been limited because data acquisition has been difficult, expensive and time intensive. Recent advances in technology, especially in electronics and computing, have allowed for the development of accurate, fast and user friendly mineral liberation analytical techniques. Basic instrumentation used for evaluating mineral liberation and mineral exposure characteristics include: optical microscopy, transmitted and reflected-light microscopy (Gribble and Hall, 1992), and SEM equipped with energy dispersive spectroscopy (EDS). Nowadays, the two SEM based automated image analysis systems including QEMSCAN (Goodall et al., 2005) and the mineral liberation analyzer (Gu, 2003) are the most commonly used systems in mineral liberation studies. In either case, the liberation analysis of polished sections overestimates the extent of liberation because some sectioned particles can appear to be fully liberated, as is exemplified in Figure 2.6

In order to estimate the volumetric liberation from polished section analysis, stereological models are applied. However, the stereological models are not satisfactory because model parameters depend on the ore texture, which is unique for each ore type (Miller and Lin 1988, 2004, 2013). Now, it is possible to make 3D X-ray microtomography (XMT) measurements of liberation.

Such measurements and data analysis are presented in Chapter 5. High-resolution 3D images revealing the internal structure of multiphase particulate samples can now be obtained through modern techniques such as XMT (Garcia et al., 2009; Medina, 2012; Hsieh, 2012,).

2.3.3 Particle-particle interactions

The difficulty of treating ores in the presence of clay minerals is well known in the mineral processing industry. There have been several studies conducted to investigate the negative effects caused by fine particles, which include surface coating (Raghavan and Hsu 1984, Bulatovic, 2007; Triffet and Bradshaw, 2008; Zanin, et al., 2009; Peng and Grano, 2010), increased reagent consumption due to the high surface area of clays (Guy and Trahar, 1984), transferring large quantities of clay minerals into the concentrate, increasing pulp viscosity, and changing froth stability. Bulatovic (2007) and Raghavan and Hsu (1984) briefly explained that the presence of clay in copper porphyry ores causes a loss in recovery, possibly due to the presence of slime coatings on mineral surfaces or on air bubbles. Clay minerals such as talc, kaolinite, bentonite, and smectite, which are often associated with copper, gold, and other valuable minerals, increase reagent consumption and can create serious frothing/nonfrothing problems at the Copperton concentrator. This phenomenon is discussed by Triffett et al., (2008), Zanin et al., (2009), and Peng (2010), who noted that there have been numerous observations of these clay minerals having a deleterious effect on mineral flotation grade, recovery, and pulp viscosity. However, rigorous investigations on how clay minerals affect flotation are still not available. Basically, major studies show that the slime coating of the mineral surface

occurs due to electrostatic attraction and explain that the fine clay particles are electrostatically attracted to the surface of mineral particles and the attachment is heavily dependent on the magnitude and sign of the zeta potentials of the mineral particles and the fines (Arnold and Aplan, 1986).

The surface charges and electrophoresis mobility can be measured using a zeta potential meter. Visual evidence for the presence or absence of slime coating can be studied with the use of a scanning electron microscope (SEM).

Another important problem generated by the presence of slime is when the fine particles of a gangue mineral adhere to each other by creating electrostatic and/or steric repulsion forces, which counterbalance the contribution of the Van Der Waals attraction to the total net force. Dispersants are widely used to modify the colloidal interactions between gangue particles. These dispersants are mostly anionic polymers and adsorb on mineral surfaces, making them more negative (Huynh et al., 2000). Classification methods such as cyclones are more economical and efficient for separating fine particles from coarse minerals (Greet and Smart, 1996). In addition, ultrasonic treatment can disperse the clay particles, increase the flotation recovery, and reduce the required collector dosage (Celik, 1988). Finally, the best and most economical way to treat these types of ores is to blend them in a small proportion with normal ores.

2.3.4 Surface oxidation

Sillitoe and Petersen (1996) mentioned that the formation of copper ore bodies occurs in the following way. Copper is dissolved deep underground and geothermal activity brings the copper near surface environments to cool. Copper and associated metals then

precipitate into veins and disseminate within rock. Oxidation occurs as the deposits are exposed to air or oxygen-rich water flowing over them. Oxidation in turn alters the mineralogy. When sulfur is oxidized, it becomes soluble and is carried away in acid solution, thus copper and iron sulfides are replaced by carbonates and oxides.

The flotation of copper sulfide minerals is intimately associated with their surface oxidation. Extensive studies have been conducted to understand how oxidation influences sulfide flotation behavior (Chander and Fuerstenau, 1974; Senior and Trahar, 1991). Fullston et al. (1999) measured the zeta potential of copper sulfide minerals including chalcocite, covellite, chalcopyrite, bornite, enargite and tennantite as a function of pH and the oxidation condition. They found that chalcopyrite was the most electrochemically noble while chalcocite was the most electrochemically active in terms of surface oxidation. As mentioned by Senior and Trahar (1991), metal hydroxides on the mineral surface decrease the flotation of copper sulfide minerals even in the presence of collector. Barzyk et al. (1981) found that chalcocite surface oxidation had a strong effect on both xanthate adsorption and chalcocite floatability, and the most oxidized chalcocite sample required 100 times more collector consumption to obtain the same flotation results than as the least oxidized sample. There is a strong relationship between copper recovery and the electrochemical potential in flotation.

2.3.5 Process water influence

Because of its impact on the quality of human life and the environment, water resource management has become an important issue in the world. Several research studies indicate that recycling of process water is a potential option. Recycled process

water may be treated and then re-introduced into various sections of flotation operations depending on its effect on mineral surface reactions (Broman, 1980; Forssberg et al., 1985; Rao and Finch, 1989; Basilio et al., 1996; Leavay et al., 2001; Wei et al., 2006).

In mineral processing plants, the processed water is recycled from the tailings dams, thickener overflows, and dewatering and filtration units. In these streams, the dissolved ions, suspended solids and flotation reagents have insufficient time to decompose and precipitate. In this case, the concentration of the contaminants can adversely affect flotation performance. Typical contaminants in the process water are the colloid materials (silicates, clays, precipitated metal hydroxides, etc.), ions of base metals, thiosalts, sulfides, sulfites, sulfates, chlorides, magnesium, calcium, sodium and potassium, as well as residual reagents such as frothers, collectors and depressants (Leavay et al., 2001; Roman, 2008). Gerson et al. (2012) reported on the effects of synthetic water samples with increasing concentrations of cations (Cu^{2+}, Fe^{2+}, Zn^{2+}, Pb^{2+}) and anions (SO_4^{2-} and $S_2O_3^{2-}$) on several ore types of KUC. Then, they calculated ion speciation/solubility and precipitation/dissolution of solid phases on these ore types using the MINTEK geochemical program. Also, Lui et al. (1993) reported that the presence of calcium ions and thiosalts improved copper flotation in a copper porphyry ore by enhanced depression of pyrite. Rao and Finch (1989), Castro et al. (2010), and Muzenda (2010) reported that an accumulation of both organic and inorganic ions primarily affect the froth stability in flotation. As mentioned by these authors, bubbles become stable and do not coalescence even in the absence of frother at high concentrations of residual reagents. It is well known that the recycled water becomes progressively more contaminated over time and results in an accumulation of dissolved ions in the processed water due to the

oxidation/dissolution of the sulfide minerals and repeated reagent addition (Rey and Raffinot, 1966; Laskowski and Castro, 2008).

2.4 Summary

The mining industry is constantly looking for ways in which to drive process efficiency in operations, reduce operating costs and maximize output. For managers and process metallurgists, there is often an expectation for continual process improvement and special tools are required to achieve this. The smart use of characterization analysis can provide a beneficial tool for increasing the effectiveness of process improvement initiatives and overall process efficiency. Understanding the composition of feed material and how valuable minerals are associated with waste gives an advantage in any bid to increase efficiency by allowing operations to target the areas of greatest potential value. Due to the many variables that influence flotation and affect the process of mineralization of air bubbles, considerable attention has been given to the development of sulfide flotation technology. In the present study, attempts have been made to understand the significance of mineral exposure/liberation, slime coating and surface chemistry in the flotation of ore types from the Bingham Canyon deposit, KUC.

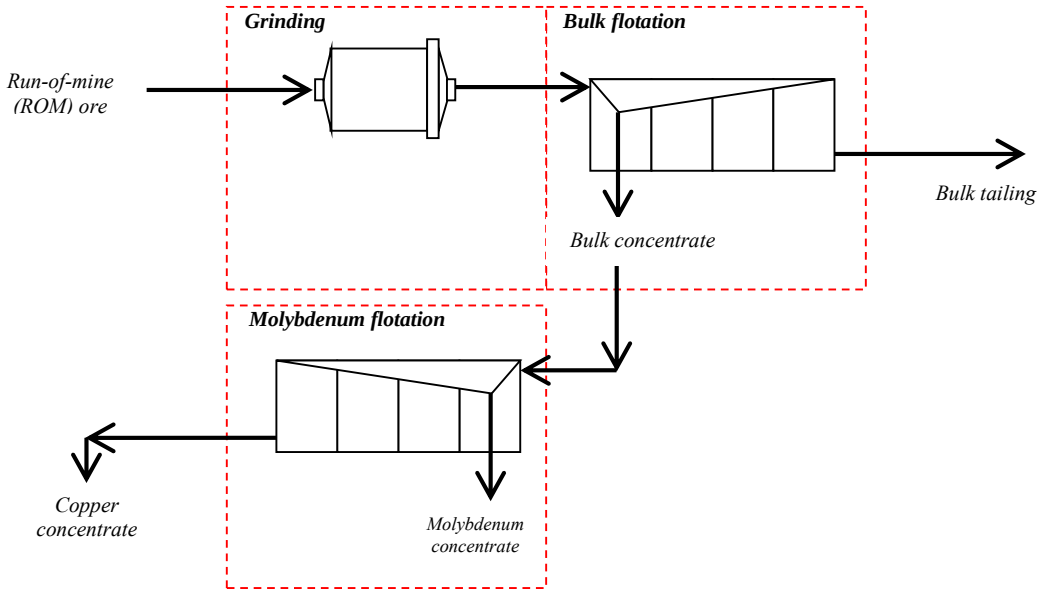

Figure 2.1 A typical flow diagram used in the flotation of porphyry copper ores (Data source: Kennecott Annual Report, 2012)

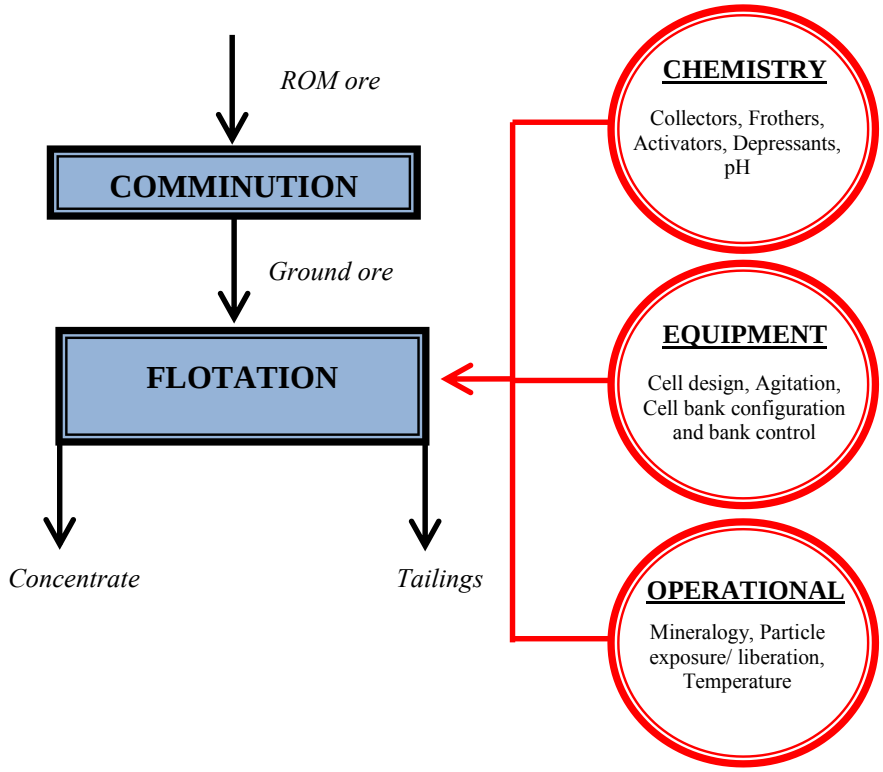

Figure 2.2 An illustration of the three main factors of flotation science and engineering (adapted from Fuerstenau, 2007).

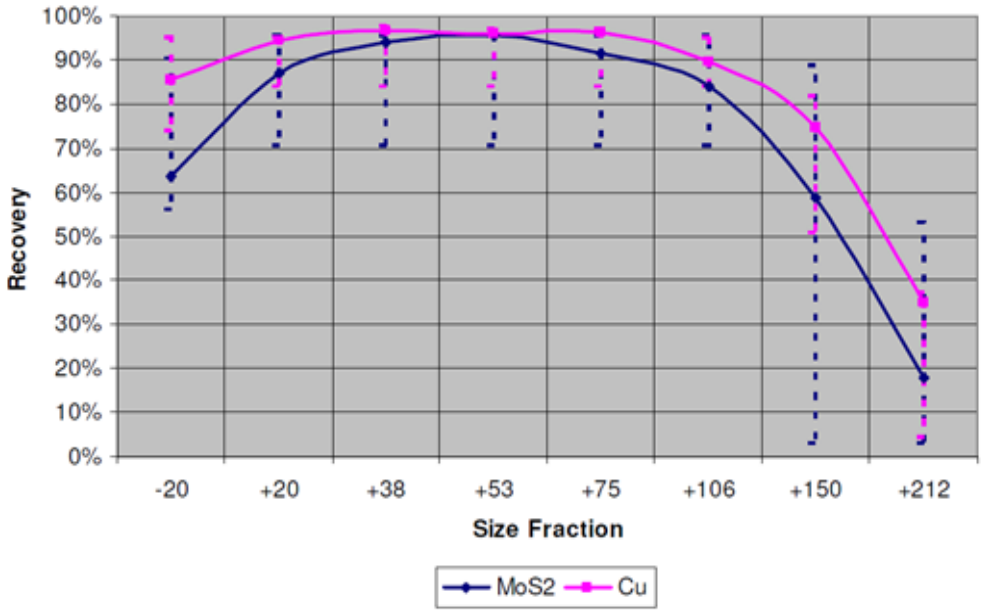

Figure 2.3 Average molybdenum recovery according to particle size for the 18 months from April 2005 until October 2006 at the Copperton plant. The curves are calculated based on analysis of weekly composites of feed and tails (Data source: Triffett et al. 2008).

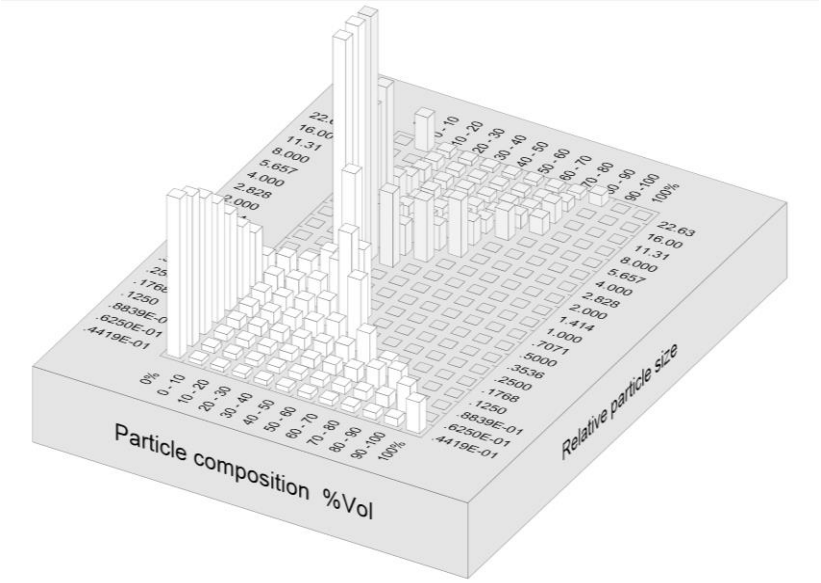

Figure 2.4 An example of a typical Andrews-Mika diagram (adapted from King and Schneider, 1998).

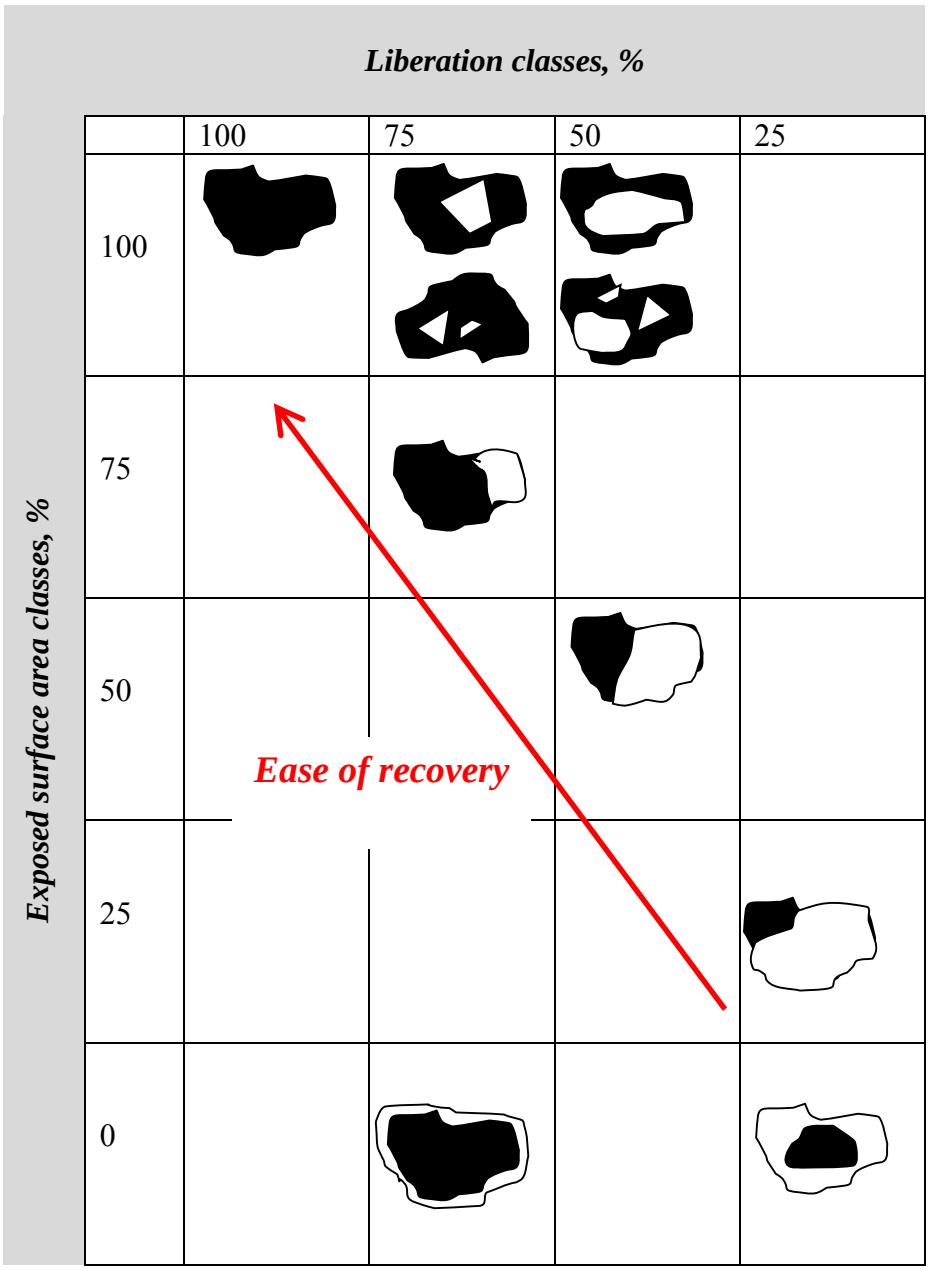

Figure 2.5 Cross section of ore particles classified by mineral composition and exposed area (adapted from the work of Goodall et al., 2005).

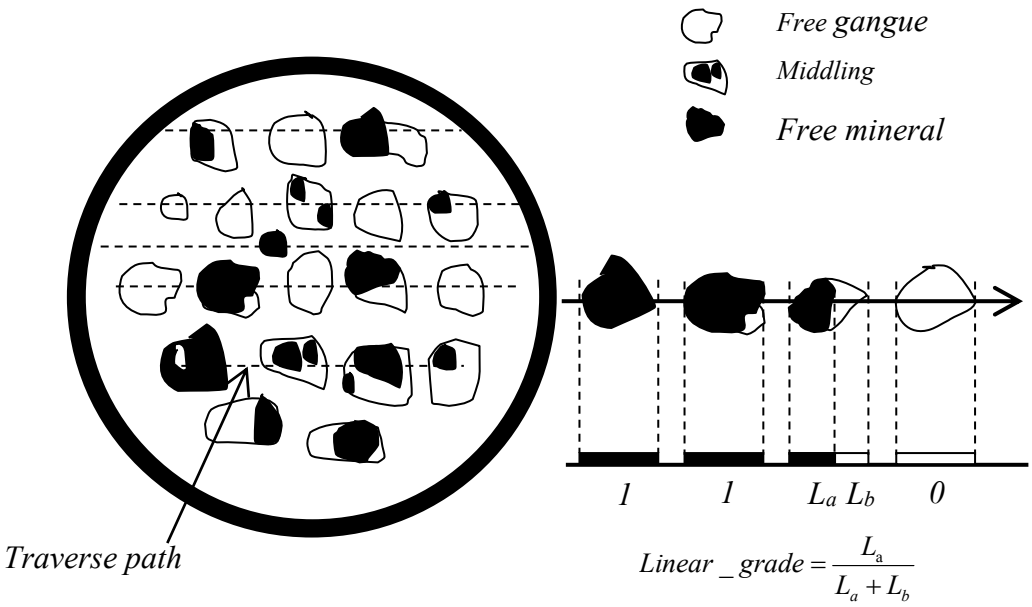

Figure 2.6 Schematic representation of the 2D scan of a polished section for liberation analysis and the basis for the calculation of linear grade (adapted from the work of Miller and Lin, 1987)

CHAPTER 3

EVALUATION OF THE FLOTATION RESPONSE OF KENNECOTT UTAH COPPER ORE SAMPLES

3.1 Introduction

The ore feeding a flotation circuit is continually changing as rock is extracted from different areas of the mine. The properties of the ore have significant impact on the ultimate grade and recovery achievable in the flotation circuit. Laboratory batch testing is a valuable tool for comparing the floatability of different ore types or predicting the metallurgical performance that will be achieved when a particular ore is processed. Flotation testing techniques described in the literature (Coleman et al., 2007) are used for batch testing in order to determine the variation in flotation response.

At the Copperton concentrator, Cu recoveries are in the 78-83% range and Mo in the 55-60% range (Triffet and Bradshaw, 2008; Zanin et al. 2009). Ametov et al. (2008) found that the recovery of molybdenite in the bulk Cu/Mo flotation circuit was consistently less than the recovery of copper sulfide, with differences ranging from 2% to 12%, based on a series of surveys at the Copperton flotation plant. According to an FLSmidth technical report (2012), the flotation recovery of Cu and Mo from several certain ore types is far inferior to the Cu and Mo recovery from the more traditional,

well-behaved ore types at the Copperton concentrator. It was reported that liberation, slime coating, surface oxidation and variation in process water chemistry could reduce the hydrophobicity of chalcopyrite and molybdenite and thus limit their flotation recovery. The objective of the flotation tests reported in this research work was to demonstrate the value of a multifaceted experimental approach, to identify difficult-to-float ore types.

3.2 Materials and methods

3.2.1 Sample identification

Between 2010 and 2012, an opportunity to work on a project at FLSmidth USA, Inc - Dawson Metallurgical Lab (FLS/DML) led directly to the premise for this dissertation. Based on a discussion in a preliminary meeting between the KUC staff and FLS/DML, flotation variability tests were performed on samples of the South Pushback ore from the Bingham Pit, KUC to evaluate metallurgical performance.

Several ore samples were received at FLS/DML on March 3, 2011 for testing and they represent different ore types from the Bingham Pit, KUC. From this meeting, it was determined that the ore would be represented by seven (7) ore types. Six to eight (6-8) individual samples (charges) of each ore type were tested, for a total of 64 samples.

A test procedure furnished by KUC, which is described in Section 3.2.3, was employed and it has been used in previous geologic variability testing of KUC ore by FLS/DML (KUC-Cornerstone project dated January 12, 2012). In that project, the main focus was to understand the variability of the basic test parameters that affect flotation performance and optimize or forecast plant performance based on these parameters.

Tables 3.1 and 3.2 contain the chemical analyses of the KUC head samples measured by FLSmidth and KUC Analytical Laboratories. The atomic absorption (AA) spectrophotometer and/or the inductively coupled plasma atomic emission spectroscopy (ICP-AES) techniques were used to determine the weight percentages of Cu and Mo, and other minor elements were scanned using the ICP-AES method. Blanks and repeat samples were carried with each batch of assays for the quality control and quality assurance (QA/QC) purposes.

Batch flotation testing was performed on each sample to determine maximum flotation recovery of Cu and Mo, at a grind target of 25% plus 100 mesh (KUC - Cornerstone project, 2012). The laboratory batch test, which is widely used to assess the flotation response of ores under particular conditions, was used to evaluate variation in mineralogy and head grade; liberation and grind size requirements; surface oxidation and slime coating effects, water quality effects and flow sheet alternatives. These tests could also estimate the recycled process water performance in the plant (Runge et al., 2007).

Batch testing results of the Cornerstone project are summarized for Cu and Mo recovery, and presented in Figure 3.1 (a) and (b) using a Box–Whisker diagram. The Box–Whisker diagram shows lower and upper quartile, median, the lowest and highest outlet values of Cu and Mo recovery of seven different KUC ore types. In addition, the size of the box represents variability of tests results; a small box indicates greater reliability of results, which in turn implies a limited number of factors affecting recovery. Conversely, a large box indicates that there may be many factors affecting recovery such as technological and statistical factors such as ore variability and sample size.

In some ore samples from the Bingham Pit, South Pushback, the recovery of Mo is

significantly lower than that of Cu, indicating more Mo is being lost in the tailings. These tailings could be reprocessed for the recovery of Cu and Mo. The loss of sulfide minerals in flotation tailings can be attributed to many factors, including particle size, insufficient retention time, incomplete liberation, slime coatings, and surface chemistry issues.

As can be seen in Figure 3.1 (a), results indicate an average of 90-95% Cu recovery was obtained for most of the ore types except LSE and MZ2S in the rougher flotation stage. For LSE and MZ2S ores, the average Cu recovery was lower than other ore types, and it was approximately 82-85% for the MZ2S and for LSE ore types, respectively. Also, results presented in Figure 3.1 (b) indicated that the lowest Mo recovery with 68-75% was obtained for these two ore types.

The first step to improve the recovery of Cu and Mo is the development of a methodology to identify the limitations to their recovery. Looking at the data, one can easily observe that LSE and MZ2S are both difficult-to-float ore types.

The question still remains, however, as to what the main contributors were that affected low flotation efficiency. In order to better understand the reasons behind normal and difficult floating, a detailed analysis on these two ore types is required. For purposes of comparison, the one baseline ore, MZ2HE, was chosen for reference.

3.2.2 Sample preparation

The samples used in this research work were obtained from the Bingham Canyon mine, KUC. Each of the samples was individually crushed in a jaw crusher, in closed circuit with screening, to produce 100 % passing 2 inch size particles, then blended by cone and quartering before removing 1/4 of each sample for reserve. The remaining 3/4

of the samples was stage crushed using a roll crusher in closed circuit with vibratory screen to minus 10 mesh (< 1.7 mm) size. The minus 10 mesh size material was blended and divided into eight (8) 2.1 kg charges. Each charge was sealed in a plastic bag and stored in the freezer at 10 ^{o}F (-12 ^{o}C).

Two splits were pulverized using a disc pulverizer and submitted to FLSmidth and KUC analytical laboratories for head analysis. The schematic flowsheet for sample preparation and subsequent characterization analysis is briefly described in Figure 3.2. Four (2.1 kg) charges were used for grind calibration, batch experiments, rougher kinetic testing and reflotation after characterization analysis. The prepared samples were divided into 12 splits on a rotary splitter for various analyses such as chemical, mineralogical, liberation analysis and surface characterization (see Figure 3.2). Remaining charges were kept for possible further analysis.

Also, two unpulverized splits were submitted to KUC for MLA analysis and to the University of Utah for liberation analysis. Results of the samples submitted for a detailed characterization analysis at the University of Utah are briefly described in Chapter 4 and Chapter 5. Sample preparation included all of the steps taken in the laboratory to provide a sample in a form that is suitable for experimental analysis. Correct sample preparation results in subsamples that are representative of the total sample. Obtaining a representative sample of dried flotation products for analysis requires particular care. Thorough mixing of the material is particularly important, since the test products are usually quite fine.

3.2.3 Flotation reagents

The types and quantity of the reagents are the most important part of the flotation process (Bulatovic, 2007).

The reagents used during the flotation experiment were mainly collectors (Cytec 8989, burner oil) and a frother (F-549). The pH was regulated using hydrated lime Ca $(OH)_2$ at pH 10.2. All reagents used were of commercial grade.

The Cytec 8989 collector received from the Copperton concentrator was 65% by weight in solution. The addition of Cytec 8989 was adjusted accordingly to report the active collector. The collector and frother were added only in the flotation stages such as in the rougher and reflotation stages.

Depending on the flotation stage and purpose, the desired reagent dosages used in this test work are shown in Table 3.3. An example of the calculation of reagent dosage for Cytec 8989 in the rougher flotation stage is presented below. The designed dosage of Cytec 8989 in the rougher flotation stage was 0.035 lb. /ton ore. The ore charge was 2100 grams.

$$\frac{M_{Cytec8989}}{M_{sample}} = \frac{X\mu L \cdot 1.166\, {}^{g}\!/_{cc} \cdot 0.65 \cdot 2000\, {}^{lbs}\!/_{ton}}{1000\, {}^{\mu L}\!/_{cc} \cdot 2100 g}$$

$$\frac{M_{Cytec8989}}{M_{sample}} = 0.035\, {}^{lbs}\!/_{ton} = 48.5\mu L(Cytec8989) \qquad (2)$$

3.3 Experimental procedure

The equipment and experimental procedures for the grind calibration, rougher kinetic test and reflotation after desliming are described in this section.

3.3.1 Grinding fineness test

The purpose of grinding fineness tests is to determine the optimum size of grind at which efficient floating of the Cu and Mo ore may be achieved at an acceptable separation rate. Mineralogical examination should indicate the particle size required to provide satisfactory exposure or liberation of copper and molybdenum mineralization.

A grind fineness test was performed on a charge of each sample to determine the approximate laboratory rod-mill grind time and mill lime addition required to obtain the desired grind fineness and slurry pH. The grind time to obtain 35, 25, and 15 % plus 100 mesh was extrapolated from the grind study, and updated where possible. The grind time was chosen for desired levels at a grind target of 25 % (fine grinding) and 35 % (coarse grinding) plus 100 mesh with 0.040 lb./t burner oil, and lime added to obtain 10.2 pH ground slurry based on the grind calibration curve. The sample was ground at a pulp density of 67 % solids. Grinding was performed in a laboratory rod mill, by wet grinding 2.1 kg of nominal minus 10-mesh sample, at a 67 % by weight solids content.

Test grinds were conducted on each sample to determine the necessary grind time required to achieve the specified target of 80 % (p80) passing sizes. A standard laboratory Denver rod mill was used as shown in Figure 3.3. A typical charge to the mill could be:

- Steel rods (19 mm diameter) kg 12.9

- Ore (- 10 mesh) g 2100
- Lime (initial) g 2.2
- Water mL 1050

The grind fineness sample was charged in the laboratory rod mill and initially ground for approximately 8 minutes followed by a screen analysis. The sample used for the screen analysis was returned to the rod mill and the calibration test progressively continued for a total of 16, 24 and, if necessary, 32 minutes with screen analyses conducted at each grind time.

Screen analyses were carried out in a Rotap™ sieve shaker, equipped with 20 cm (8”) diameter test sieves, stacked in ascending mesh sizes. After each step of grinding, the sample was initially wet screened at 37 µm (400 Tyler mesh) size class. The + 37 µm fractions were then dry screened through a stack of 37 µm to 400 µm sieves. Each sieved fraction was collected and weighed for calculating the size distribution. The screen analysis test results were used to determine the particle size distribution and calculate the related p80 (80% passing size) for achieving the required period of grinding.

3.3.2 Flotation procedure

Basically, two stages of flotation experiments, as described in Figure 3.4, were performed to evaluate Cu and Mo recovery in the flotation testing; the first stage was (1) a rougher flotation test, and the second stage was (2) a reflotation test after detailed characterization analysis. The rougher tailings were deslimed to remove fines (less than 400 meshes) before the reflotation test.

The rougher flotation test was completed on each ore type and was routinely

conducted using Galigher Agitair forced air cells for all flotation runs. The sample charge for all tests was fixed at 2.1 kg. The grind time was chosen from desired levels based on the grind calibration curve. Based on the flotation conditions, the slurry was rinsed after grinding with tap water into a 5.4 L volume flotation cell (± 30 % solids) and the pH was re-adjusted with lime, $Ca(OH)_2$, to 10.2 – 10.3. The impeller rotation speed and air consumption were kept constant at 900 rpm and 7 l/min, respectively. The total duration of the flotation test was about 10 minutes to achieve the maximum amount of Cu and Mo recovery. During the second stage of testing, fines in some ores and/or flotation products after grinding, cause slime problems during rougher flotation. The removal of such slimes is necessary to decrease reagent consumption. To clean the surfaces of Cu and Mo minerals of the flotation test was about 10 minutes to achieve the maximum amount of Cu and Mo recovery. During the rougher flotation test, four concentrates were collected at 0 – 1; 1 – 3; 3 – 5; 5 – 10 minutes. It is ideal to collect the first concentrate at 1 minutes. If this is not possible then collection from 0 – 2 minutes is acceptable, but not beyond that. The test must be run long enough to ensure that the cumulative recovery vs. flotation time curve flattens out and is at, or is approaching, a plateau. Froth was collected every 15 seconds. The first concentrate had four collections, at 15, 30, 45 and 60 seconds. The second concentrate also had four collections at 75, 90, 105 and finally 120 seconds and so on. The pulp level was constantly maintained at 1.5 to 2.0 cm below the cell lip, and improved metal recovery in flotation. For example, if slime coating accounts for Cu and Mo loss, desliming was performed with the tailings from the rougher kinetic flotation using a 400 mesh (37 μm) screen to remove the -400 mesh slime fraction.

Half of the rougher tailings were used in this stage followed by desliming flotation with the addition of reagents to collect more froth at a second flotation stage.

Representative amounts of each of the flotation products such as feed, rougher concentrate, rougher, and scavenger tailings were split, prepared and submitted for chemical assays for Cu, Mo, Fe and total S. All chemical analyses were done in industrial analytical laboratories, specifically those of FLSmidth and Rio Tinto. Detailed characterization such as mineralogical and liberation analysis, surface oxidation and slime coating were done in laboratories at the University of Utah. The main analytical techniques were X-ray computed tomography, optical microscopy, SEM-EDS, and XPS.

3.4 Results and discussion

3.4.1 Grind fineness test

The grind fineness test was carried out under the same conditions at 8, 16 and 24 minutes for each ore type. In this case, the LSE and MZ2S ore samples were predominantly used in this research and the experimental conditions and the corresponding results are presented in Tables 3.4 and 3.5, and are plotted in Figure 3.5.

Based on the grind fineness results, both the LSE and MZ2S ore types were very slimy and soft ores. For example, in the case of the LSE ore, it can be easily seen from Table 3.5, that the amount of the fines below 400 mesh for the LSE ore is about 22.5 % after 8 minutes and 34.8 % after 16 minutes of grinding, respectively.

Thus, it is shown that the slime content significantly increased during the slight increase in grinding time for the LSE and MZ2S samples. The results are demonstrated in Figure 3.5 (a) and (b).

As observed from Figure 3.6, the particle size distributions of these ore samples are very similar. There was a slight difference in size distribution during the first 15 minutes of grinding but noticeable difference after 15 minutes of grinding, as shown in Figure 3.6. Figure 3.6 also shows the percentage of + 100 mesh material as a function of grind time. The appropriate grind time required to produce 25 % and 35 % plus 100 mesh were estimated from the grinding calibration curves and this was approximately 9.45 and 12.45 minutes, respectively.

The grind sizes of p80 = 132 μm and p80 = 195 μm were selected to present fine and coarse grind sizes in order to compare the effect of grind fineness on coarse and fine grinding recovery in the case of the LSE ore. In addition, Figure 3.6 indicates a linear correlation between the material passing 100 mesh sizes and grinding time for all ore types. Based on grind calibration test results, the calibration curve of the LSE ore was significantly lower than other ore types, indicating that the LSE ore is softer than the other ore types. Soft ore, generally, creates more slime during grinding, which in turn, means more slime problems could occur during flotation of this ore type.

3.4.2 Effect of grind size

The appropriate grind fineness is the key to improving the quality of the flotation concentrate. Two different kinds of grinds were tested on the LSE, MZ2S and MZ2HE ore types to evaluate the effect of the lithological characteristic on flotation. In total, eight rougher flotation kinetic tests were done. The test objectives, experimental conditions and summary of results for these tests are presented in Appendix A. This section is more focused on comparative results of the more significant variables tested. The influence of

grind fineness on flotation of these ore types is illustrated in Figure 3.7. The average Cu recovery for all samples generally increased from 79.12 % to 92.34 % as the grind fineness became finer from 35 % to 25%, plus 100 mesh size in the rougher flotation stage. As seen from Figure 3.7, an increase of Cu recovery during fine grinding is evident. The sensitivity of Cu recovery is generally significant, which means that liberation could be a main issue for Cu recovery for nearly all ore types. A more detailed analysis is presented in Chapter 5.

In mineral processing, grinding not only reduces the particle size and liberates minerals, but also provides differential surface on valuable and gangue minerals. This allows effective separation of these minerals in subsequent separation processes such as flotation, which exploits the difference in surface wettability of valuable and gangue minerals (Grano et al., 2009). As displayed in Figure 3.7, Mo recoveries are very unpredictable. The baseline ore, MZ2HE, shows a characteristic slight increase in Mo recovery with an increase in grind time. When comparing the LSE and MZ2S samples with the reference ore, the Mo recovery of the LSE sample showed an unusual increase with grind time, from 74 % to 86 %.

Conversely, in the case of the MZ2S ore, the fine grinding had the reverse effect on the Mo recovery and it was more slowly floated than other ore types. As is widely known, molybdenite is one of the most readily floatable minerals of all sulfide minerals, but enrichment of its ore by flotation is not always simple. In particular, a number of chemical mechanisms including the oxidation of minerals and media, oxygen reduction and galvanic coupling occur and govern the surface properties of molybdenite minerals at the Copperton concentrator. There have been numerous research activities on Cu and Mo

loss in the tailings of the Copperton concentrator. In Triffett et al. (2008), molybdenite particles collected from different stages in the Copperton plant were analyzed using time-of-flight secondary ion mass spectrometry (ToF-SIMS), showing that the surface oxidation or contaminants in the water, as well as residual flotation reagents such as frothers, collectors and depressants are the main cause of molybdenite loss.

Zanin et al. (2009) studied the slow molybdenite flotation behavior and attributed it to fine hydrophilic gangue particles or adsorbed ions interfering with the molybdenite surface and reducing the available hydrophobicity. Ametov et al. (2008), Roman (2008) and Zhou (2010) discussed particle size; edge-to-face ratio; morphology and water chemistry (pH, cations); slime coating and surface oxidation; all variables related to the structural properties of molybdenite, which may cause a significant change in the flotation recovery of molybdenite. In his research, Zhou (2010) discussed the finding that the fine molybdenite, which has a large face-to-edge ratio, was easily affected by pulp conditions.

Based on the literature, several detailed analyses were performed on the selected KUC ore types to investigate the reasons for Cu and Mo loss. Rougher flotation testing including grade-recovery analysis, detailed characterization analysis of lost particles in rougher tailings, and scavenging reflotation, was done.

Detailed characterization analysis of lost particles in rougher tailings including size-by-size recovery analysis, surface oxidation, slime coating and liberation analysis have been done on each of the rougher flotation tailings and the corresponding results are described in Chapter 5.

3.4.2.1 MZ2HE ore

Tests T5a and T6a on the MZ2HE ore, show that the primary grind size affects the final rougher concentrate grade and recovery, as summarized in Table 3.6. At the coarsest grind (T6a), the rougher flotation tailings analyzed 0.11 % Cu and 0.009 % Mo with rougher concentrate recoveries of 82.9 % Cu and 84.6 % Mo. Recoveries at the finer grind (T5a) were 92.5 % Cu and around 85.8 % Mo, with flotation tailings grades of 0.05 % Cu and 0.008 % Mo. When p80 decreased from 195 to 132 μm, the recovery of Cu and Mo increased 9.6 % and 1.2 %, respectively. Table 3.6 shows that Cu and Mo recoveries and concentrate grades improved at the finer grind size.

Flotation rate, grade/recovery and selectivity curves are graphs that were constructed from the results collected during the rougher flotation kinetic tests, and are presented in Appendix A. These curves are ideal for comparing the results of different tests. The flotation rate curve displays the cumulative recovery of the mineral (on a percentage basis) recovered at each time interval during a test. The slope of this curve is the rate of flotation recovery and the recovery value at which the curve asymptotes is an indicator of the proportion of floatable mineral in the tested sample. It is desirable that the valuable mineral in a sample exhibit fast flotation kinetics (steep slope) and the proportion of nonfloating mineral in the sample be minimized.

The proportion of nonfloating valuable mineral is an indicator of the amount of mineral that is either in particles too large or too small for flotation, locked with nonfloating particles or with a hydrophilic surface state due to insufficient collector coverage or depressant coatings. As expected, a finer grind resulted in greater recovery for both Mo and Cu. The optimum grind size p80 for Cu and Mo flotation was

approximately 132 μm. For MZ2HE, the rougher kinetic results for Cu and Mo recovery are displayed in Figure 3.8. Furthermore, the slope and tendency of the flotation rate of both fine and coarse grinding are quite similar, which indicates that there are no more than one or two factors that account for their recovery. Results indicate that generally, the Cu flotation rate for the fine grinding was much better than that for the coarse grinding. The flotation rates were stabilized after 3 minutes in both cases. Particle morphology such as size and liberation state could be the main issue affecting Cu loss for the MZ2HE ore.

However, with Mo, there is no significant difference in Mo recovery between fine and coarse grinding. It is difficult to speculate on the reason for the loss of Mo. However, the nature of the lost particles have been examined using advanced characterization instruments, and an explanation for the difference in the flotation response is presented in Chapter 5. Also, separation efficiency of any concentration operation can be expressed by a curve showing the recovery attainable for any value of concentrate grade. The theoretical grade/recovery curve for an ore is a definition of the maximum expected recovery by flotation of a mineral at a given grade. To establish the theoretical grade/recovery curve for a mineral, a mineralogical liberation study should be undertaken using tools such as QEMSCAN, MLA and HRXMT.

Using these tools in combination with standard flotation tests can quickly and efficiently define the efficiency of a process and show where potential improvements may be made. In the current research, the experimental grade/recovery curve obtained from flotation kinetic data and chemical composition were created at each time interval. This curve does not, however, give an estimate of the grade and recovery achievable in a

multiple stage flotation circuit. However, this curve does give a good relative measure of selectivity. The experimental grade/recovery curves of the MZ2HE ore based on flotation kinetic data when the p80 grind size was reduced from 195 μm to 132 μm are presented in Figure 3.9. There exists an inverse relationship between concentrate grade and cumulative recovery. If the concentrate grade is very high, it implies that it has minimal contamination with gangue material and inevitably some of the valuable minerals lost to the tailings and cumulative recovery will be low. Separation efficiency increases in the direction defined by the arrow in Figure 3.9. Figure 3.9 shows cumulative grade/recovery curves in which Cu and Mo were floated after coarse grinding (solid line) and then after fine grinding (dashed line), to determine if grind fineness could give an improved performance. Four sequential timed concentrates were taken in each case. The fine grinding curves appear to show similar flotation initially, then the curves for Cu recovery significantly increased, but the grade decreased slightly from 12.5 – 11.7 % with an increase in fine grinding.

Therefore, with significant increase in Cu recovery, the grade was only slightly compromised. It was expected that the additional Cu particles were directed into the rougher concentrate after fine grinding. That is why these fully and/or partially liberated Cu particles are increasing Cu recovery and decreasing Cu grade in the rougher concentrate. In the case of Mo flotation, Mo recovery and grade showed no significant differences in the MZ2HE ore. It was expected that liberation was not the reason for Mo loss. If a comparison of size-by-size recovery analysis of Cu and Mo was made on both feeds and rougher tailings, then we might be able to explain the reason for low Mo recovery using HRXMT analysis.

3.4.2.2 LSE ore

Two different grind sizes were tested on the LSE ore sample to evaluate the effect of the lithological characteristic on the flotation. Table 3.7 indicates that Cu and Mo recoveries and grades improved significantly at the finer grind size.

The recoveries of Cu and Mo increased 9.34 % and 8.47 %, respectively, when the p80 decreased from 220 µm to 148 µm. As expected, a finer grind resulted in greater recovery for both Mo and Cu. The optimum grind size (p80) for Cu and Mo flotation was at 148 µm. Furthermore, with both the fine and coarse grinds, the recovery kinetic curves for the Cu and Mo, were quite similar, which indicates that there are no additional factors that account for their recovery. For the LSE ore, kinetic results for Cu and Mo recovery are shown in Figure 3.10. Results indicate that generally, flotation rates of Cu and Mo continually increased in the coarse grinding stage. This increase was significantly decreased after fine grinding.

It might be explained that these minerals were liberated from gangue minerals and then easily floated after fine grinding but the kinetic curve for these minerals still did not reach a plateau on the graph. This slight increase in Cu and Mo loss could be explained by a different factor, which can affect flotation performance. The experimental grade/recovery curves of the LSE ore are illustrated in Figure 3.11.

The grade/recovery curves can also give some additional information relating to "slow" and "fast" floating effects of chalcopyrite and molybdenite. Fast floating effects are mainly related to particle size and liberation (the difference between the 1st concentrate at 0-1 minute) issues and slow floating is explained by surface oxidation and slime coating effects. In the LSE ore, the Cu recovery increased from 79.1 % to 88.5 %,

as more Cu was liberated, but the grade had no significant difference with an increase in grind fineness. Hence, we can expect that liberation does not affect grade and this phenomenon may attribute to slime coating. Slime coating and slime aggregation could be a dominant issue in the loss of Cu and Mo for the LSE ore.

In other words, as indicated in the graph for the grade/recovery curve of Cu, the slope of the flotation rate curve for Cu minerals was less steep for the coarser ground material, and then it increased during the fine grinding stage.

3.4.2.3 MZ2S ore

A similar series of tests was conducted on the MZ2S ore sample to confirm the response of different mineralization materials to the grind size. Cu recovery increased from 87.6 % to 91.2 % with decreasing particle grind size from p80 of 205 μm to 146 μm. Table 3.8 shows that Cu recovery and grade improved at the finer grind size but Mo exhibited a reverse result and recovery and grade significantly decreased.

The losses of Mo were considerable at the grind size p80 of 146 μm. At the finest grind (T3a), the final flotation tailings graded 0.11 % Cu and 0.019 % Mo with rougher concentrate recoveries of 91.2 % Cu and 75.6 % Mo. As shown in Figure 3.12, Mo recovery at the finer grind (T3a) was significantly lower than the flotation recoveries of the other ore types. Compared with coarse grinding, the recovery of Cu in fine grinding increased 3.6 % and recovery of Mo decreased 5.2 %. For the MZ2S ore, flotation kinetic results for Cu and Mo recovery are presented in Figure 3.12.

Results indicate that the flotation rate of Cu and Mo continually increased for both fine and coarse ground material. Their flotation rates did not stabilize and the froth

formation was very weak during the first 10 minute flotation period under standard testing conditions.

With an increase in dosage of flotation reagent and time, the flotation performance (as judged from froth formation) improved considerably, resulting in well mineralized, stable and thick froth.

The grade/recovery curves of the MZ2S ore for Cu and Mo when the grind size was reduced from p80 of 205 μm to 146 μm are shown in Figure 3.13. During first few minutes of flotation, the Cu grade increased from 26.5 – 30.5 % and the whole curve was pushed up to the right, presenting greater opportunities for recovery improvement to be made. The increased recovery at the finer grind size can be seen to rise from 87.6 % to 91.3 % in the cumulative concentrate grade with 22.5 % Cu. It was expected that the recovery of Cu is mainly dependent on the liberation state than on other factors of this ore type because the new, freshly exposed surfaces of the Cu particles could actively contact with the flotation reagent after fine grinding. However, Mo recovery was still unpredictable and it is difficult to explain reason for the lost Mo particles. In the case of Mo, all new surfaces are reacting with an unknown chemical compound or species.

To understand the general characteristics of the flotation response achieved with this ore type, the rougher tailings samples were studied using optical microscopy. Upon visual inspection, the molybdenum minerals were found to be round like a disk, smooth, and clean in the rougher concentrate. Also, all the isolated Mo mineral particles appeared to be well liberated. Significantly, similar molybdenite particles were observed in the MZ2S rougher tailings. The photomicrograph for the MZ2S rougher tailing sample is presented in Figure 3.14. The general mineralogical composition for the rougher tailings of the

MZ2S ore not only consisted of chalcopyrite, molybdenite, pyrite and quartz (gangue), but also a significant amount of Fe oxide minerals, such as hematite and magnetite, were regularly observed in this ore type. Also, the surface of the Mo particle seemed to be very brittle, strongly damaged and sometimes coated by some white powdery minerals on its surfaces and Mo loss was comparatively higher than for other ore types. This could be explained by the fact that the MZ2S ore had undergone significant surface oxidation, but visual inspection could not explain and confirm the reason for the loss of Mo.

The oxidation of near-surface sulfide minerals by atmospheric oxygen is critical for understanding and determining the flotation environment of weathering of sulfide-bearing bulk minerals. To better understand the reasons for such sulfide in the tailings, further detailed characterization studies were carried out using SEM-EDS and XPS analysis in order to understand why these naturally hydrophobic molybdenite particles were lost in the tailings. It was expected that either gangue mineral slimes were adsorbing onto the surface, or that surface oxidation and scale precipitation were occurring from the process water. As reported by many researchers, water chemistry plays an important role in molybdenite flotation due to the highly reactive edge surfaces of molybdenite crystals, particularly for fine molybdenite particles with large edge-to-face ratio. However, the appearance of sulfide minerals in the tailings is not normally expected.

3.5 Summary and discussion

In summary, 64 samples representing 7 ore types from Bingham Canyon were evaluated with batch rougher flotation tests and several ore types have been identified as difficult-to-float. The flotation recovery of Cu and Mo from these ore types is far inferior

from that of other more traditional ores with well behaved flotation characteristics. It is suspected that liberation, slime coating, surface oxidation and variation in process water chemistry may reduce the hydrophobicity of chalcopyrite and molybdenite and thus limit their flotation recovery. The objective of the flotation tests reported in this chapter was to examine the nature of lost particles using several experimental techniques such as size-by-size analysis, and flotation testing including rougher flotation kinetics, grade/recovery analysis, and scavenging flotation after desliming in order to determine the reason for the inferior flotation. Looking at the experimental data, one can easily observe that the LSE and MZ2S ore types are both difficult-to-float ore types. The sensitivity of Cu recovery to the grind fineness for the individual samples is generally significant, which means that liberation could be a main issue for Cu recovery for LSE and MZ2S ore types. Also, as is widely known, molybdenite is one of the most readily floatable minerals of all sulfides, but recovery by flotation is not always simple.

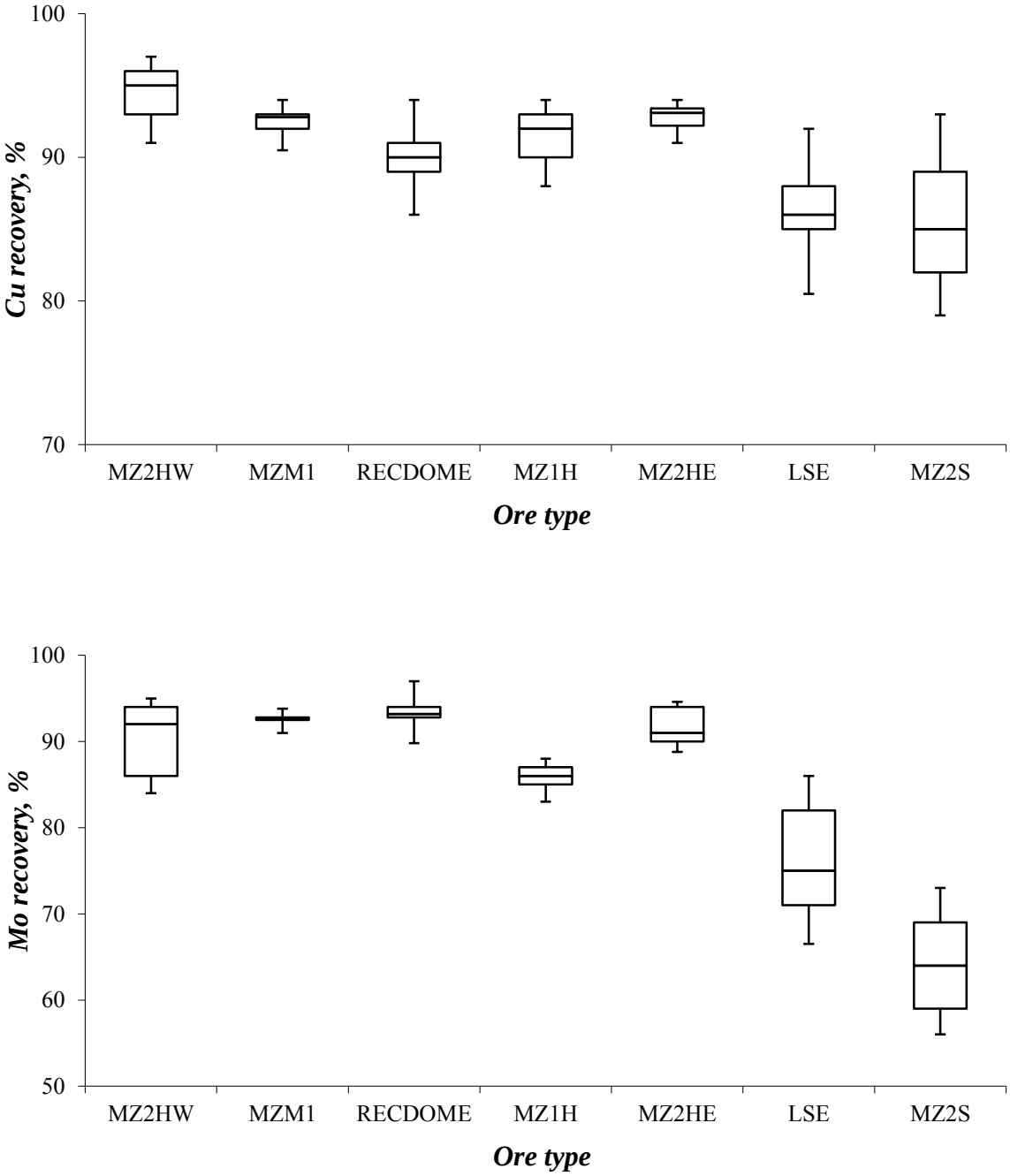

Figure 3.1 Results of copper (a) and molybdenum (b) recovery of batch flotation tests for each ore type, at a grind target of 25% plus 100 mesh (modified from FLSmidth, 2012).

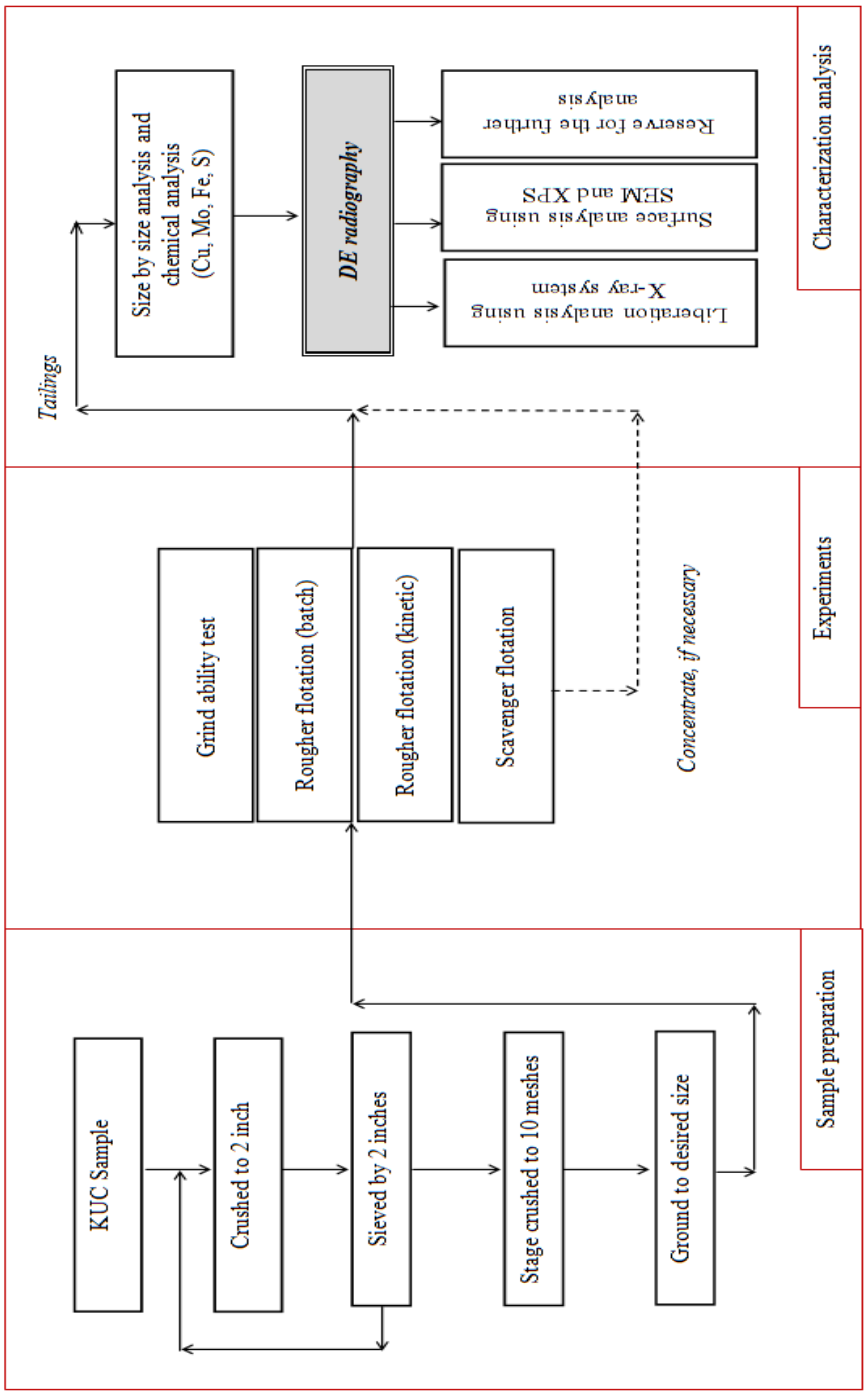

Figure 3.2 The schematic flowsheet for sample preparation and subsequent characterization analysis.

Figure 3.3 Laboratory rod mill used for grinding calibration tests prior to liberation and flotation testing.

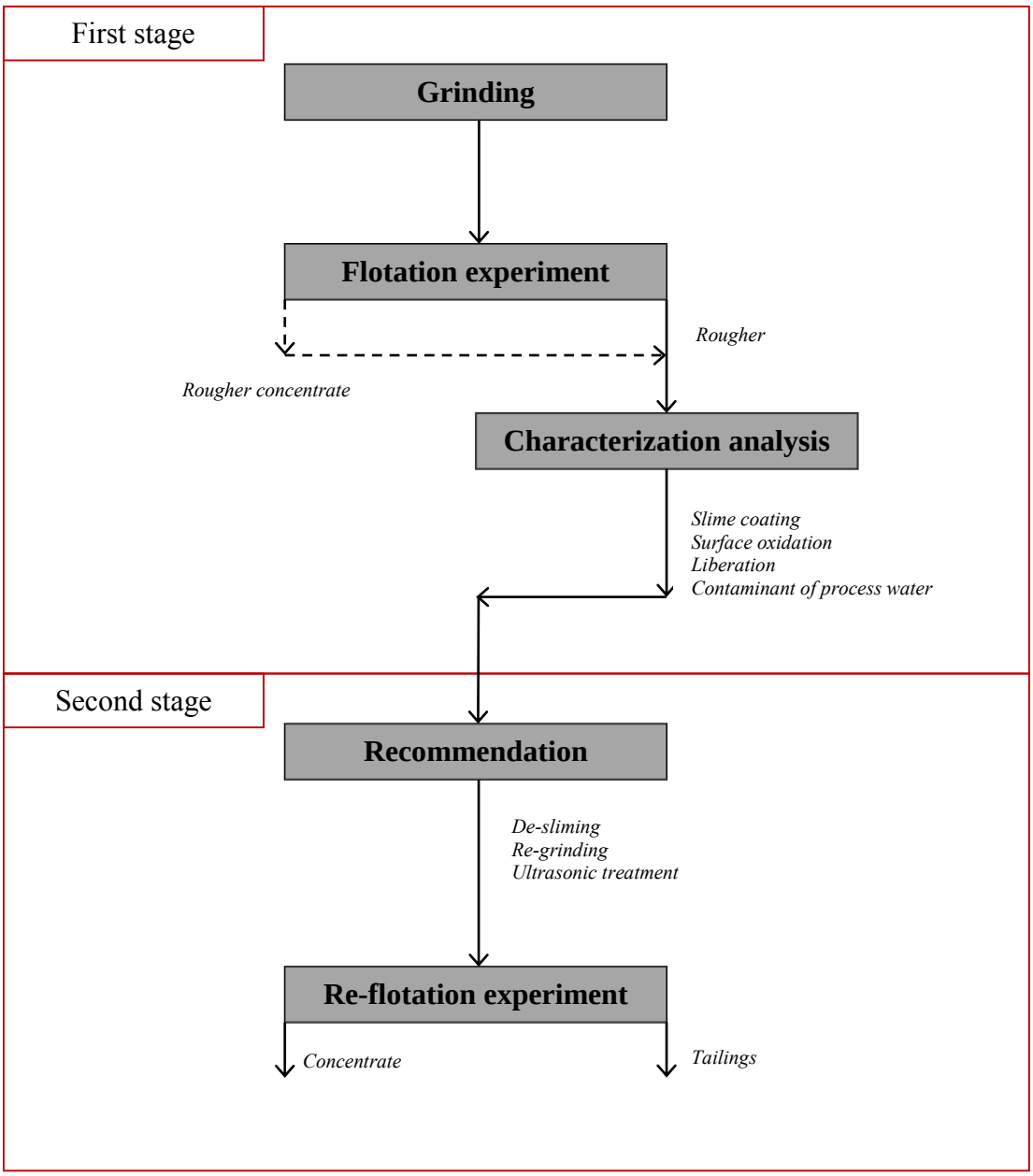

Figure 3.4 Schematic diagram of the standard flotation test work including a detailed characterization analysis.

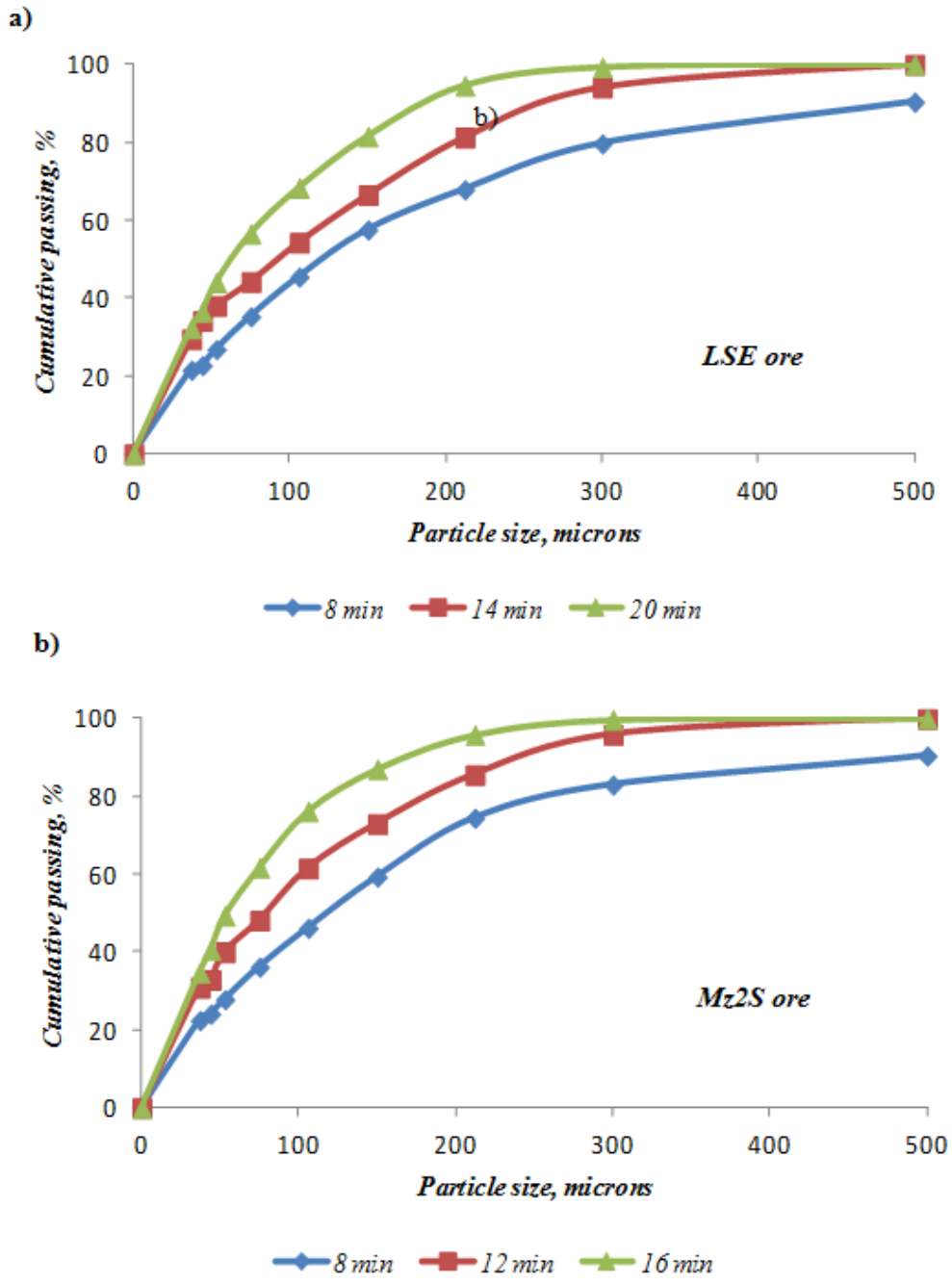

Figure 3.5 Particle size distributions of the LSE (a) and MZ2S (b) ore samples after grinding for different times.

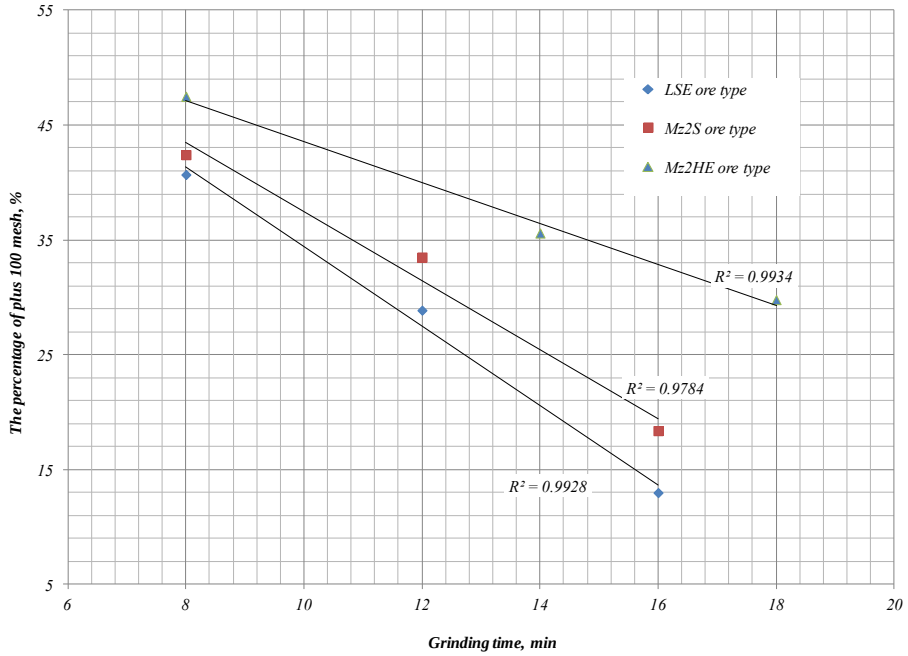

Figure 3.6 Grind calibration curve of the LSE, MZ2S and MZ2HE ore types.

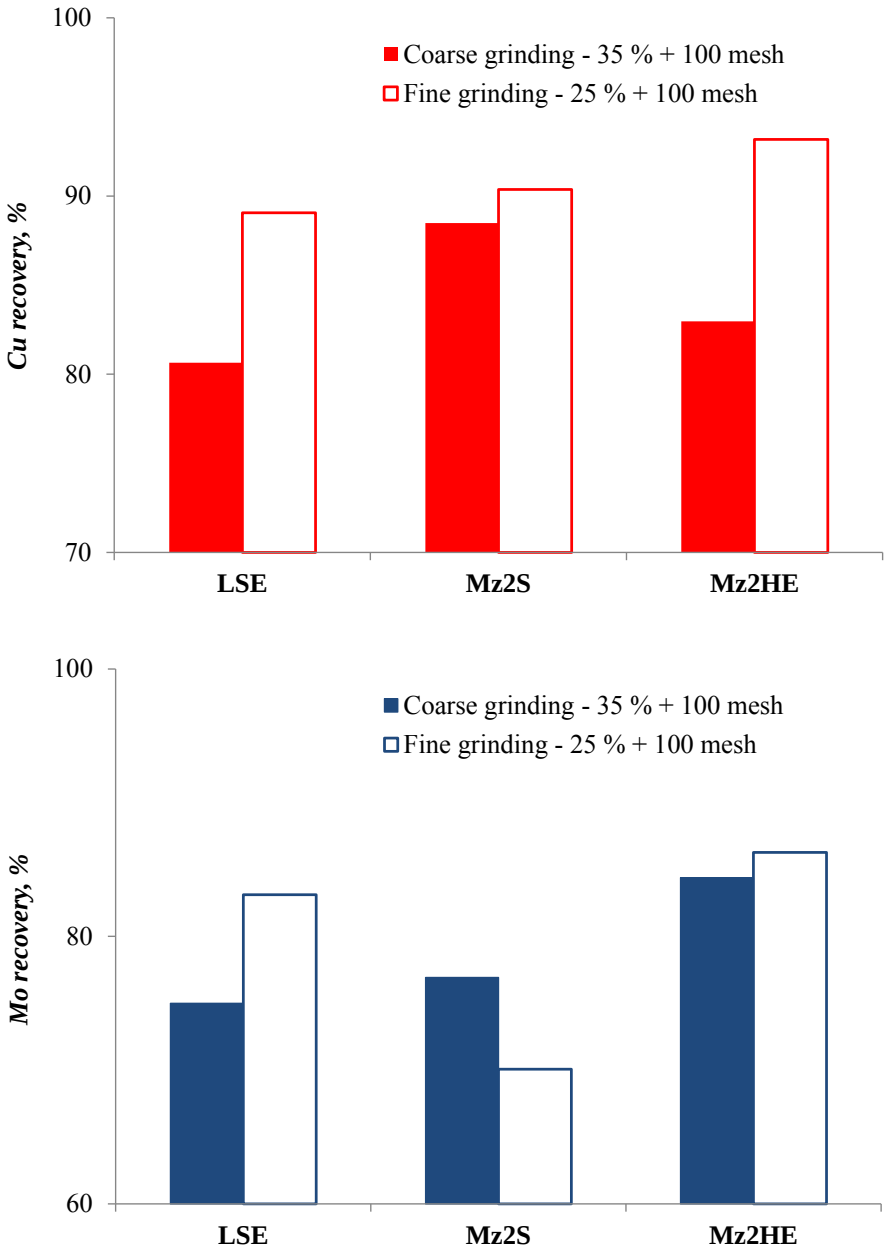

Figure 3.7 Cu and Mo recovery of the MZ2HE, LSE and MZ2S ore samples at different grind fineness.

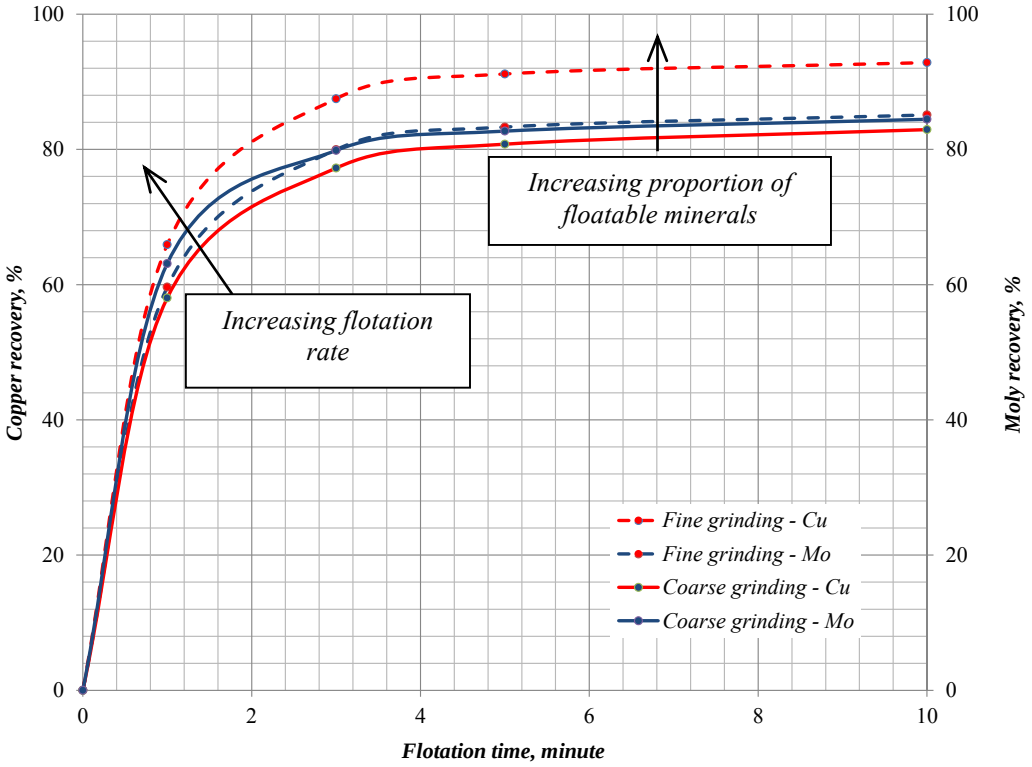

Figure 3.8 MZ2HE ore: copper (red) and molybdenum (blue) flotation kinetics during rougher flotation. Solid line represents coarse grinding at 35% +100 mesh and dashed line represents fine grinding at 25% -100 mesh.

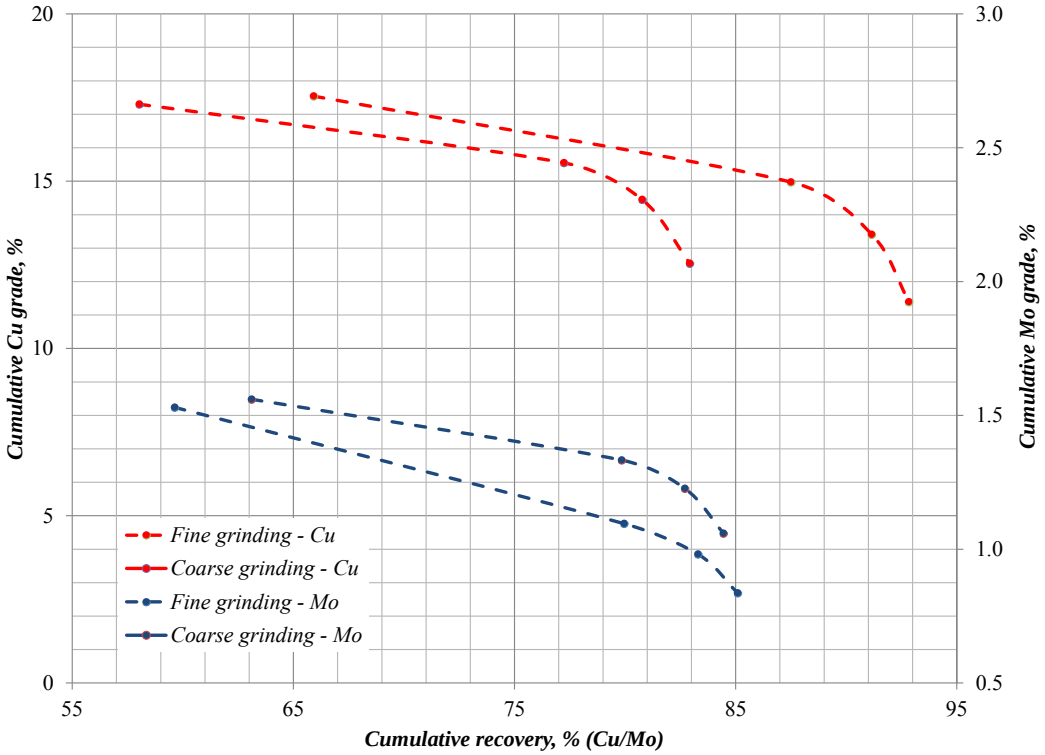

Figure 3.9 Illustration of typical form of grade/recovery curves for froth flotation based on chemical analysis and rougher flotation kinetic data MZ2HE ore. Each curve represents the cumulative grade vs. the cumulative recovery for each time interval.

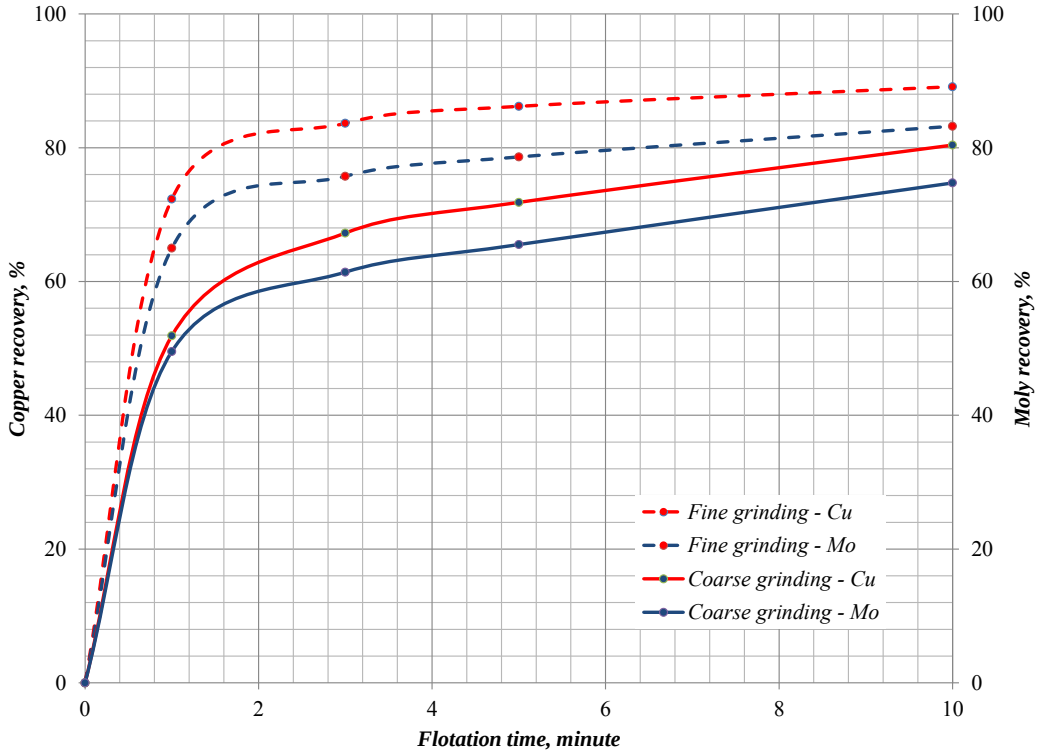

Figure 3.10 LSE ore: copper (red) and molybdenum (blue) flotation kinetics during rougher flotation. Solid line represents coarse grinding at 35% +100 mesh and dashed line represents fine grinding at 25% + 100 mesh.

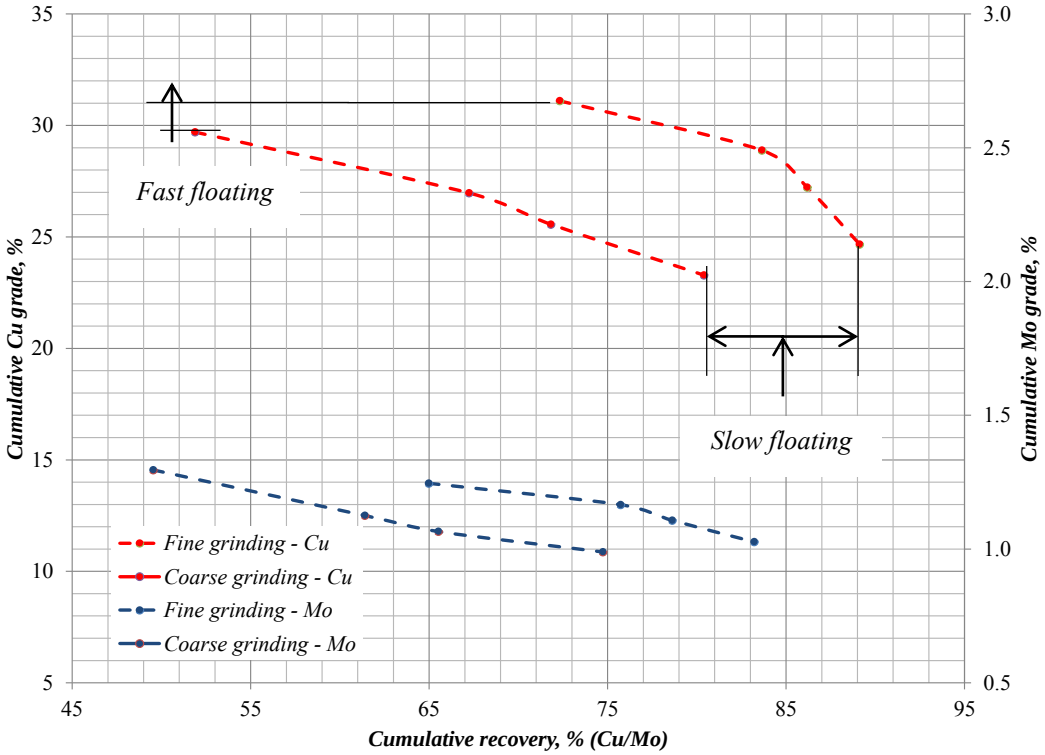

Figure 3.11 Illustration of typical grade/recovery curves for froth flotation based on chemical analysis and rougher flotation kinetic data of the LSE ore.

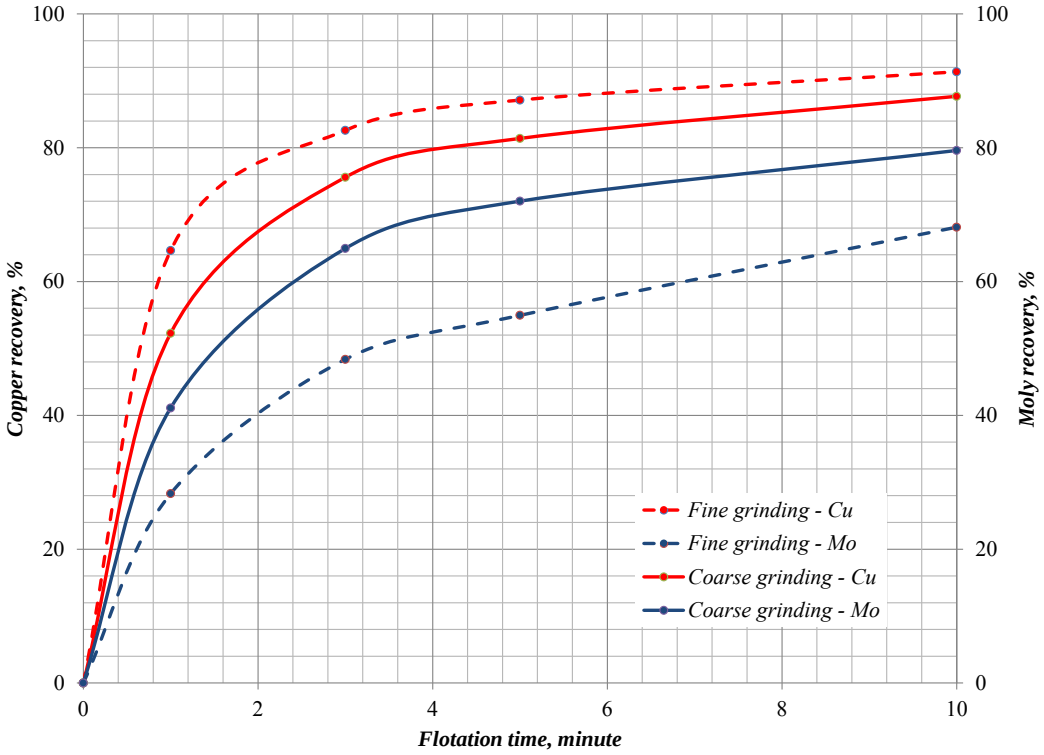

Figure 3.12 Flotation kinetics of the MZ2S ore showing the relation between the Cu and Mo recoveries with respect to the flotation time.

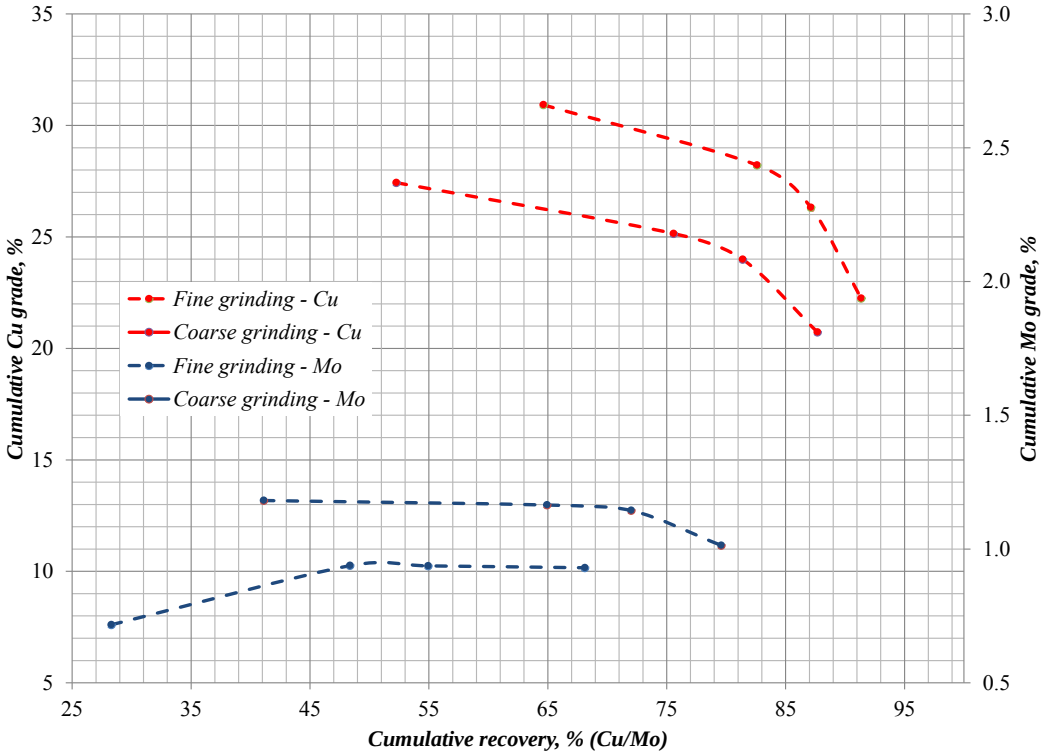

Figure 3.13 Illustration of typical form of grade/recovery curves for the rougher flotation of the MZ2S ore.

Figure 3.14 Lost sulfide particles in the rougher tailings of the MZ2S ore sample; photomicrograph by optical microscopy.

Table 3.1 Chemical assay report for KUCC head sample (adapted from FLSmidth lab).

Element	Unit	Ore type						
		MZ2HW	MZM1	REC DOME	MZ1H	LSE	MZ2HE	MZ2S
Cu	%	0.54	0.28	0.29	0.53	0.96	0.60	1.00
Mo	%	0.03	0.04	0.04	0.03	0.04	0.05	0.06
Fe	%	2.75	3.48	3.14	3.77	11.17	2.36	1.69
Au	ppm	0.10	0.08	0.09	0.15	0.43	0.32	0.52
Ag	ppm	1.63	2.20	2.33	3.13	5.00	4.00	6.23
S	%	0.75	1.33	0.83	1.12	1.48	0.92	1.17
SiO_2	%	61.40	58.64	58.43	57.74	47.37	58.24	

Table 3.2 Chemical assay report for KUCC head sample (adapted from KUCC lab).

Element	Unit	Ore type						
		MZ2HW	MZM1	REC DOME	MZ1H	LSE	MZ2HE	MZ2S
Cu	%	0.53	0.26	0.27	0.47	0.89	0.56	1.08
MoS_2	%	0.04	0.05	0.07	0.03	0.06	0.06	-
Mo	%	0.02	0.03	0.04	0.02	0.03	0.05	0.06
Au	ppm	0.00	0.00	0.00	0.01	0.01	0.01	0.48
Ag	ppm	0.03	0.04	0.03	0.07	0.13	0.08	6.41

Table 3.3 Designated reagent dosage in the flotation stage.

	Units	Cytec 8989	Burner oil	F - 549
Density	g/cc	1.166	0.81	0.99
Purity	%	65	100	100
Grind study test	lb/t	-	0.04	-
Rougher kinetic test	lb/t	0.035	0.07	0.046
Reflotation test	lb/t	0.010	0.05	0.023

Table 3.4 Summary of experimental results of the grind calibration study for the LSE and MZ2S ore types.

Ore type	LSE			MZ2S		
Grind time, minute	8	12	16	8	14	20
$Ca(OH)_2$, gm	1.2	1.9	2.4	1.2	1.9	2.4
pH	9.8	9.6	10.48	9.8	9.4	10.32
% + 100 mesh	40.7	27.1	13.0	42.4	33.5	18.4
p80	266	182	120	303	206	144

Table 3.5 Weight distribution into each size fraction of the LSE and MZ2S ore types.

Size class		Cumulative Passing, %					
		LSE ore			MZ2S ore		
mesh	μm	8 min	12 min	16 min	8 min	14 min	20 min
20	841	100.0	100.0	100.0	100.0	100.0	100.0
28	595	99.1	100.0	100.0	100.0	100.0	100.0
35	500	97.1	100.0	100.0	96.9	100.0	100.0
48	300	90.4	99.9	100.0	90.4	100.0	100.0
65	212	82.9	95.8	99.7	79.7	94.2	99.3
100	150	74.4	85.5	95.8	67.9	81.3	94.6
150	106	59.3	72.9	87.0	57.6	66.5	81.6
200	75	46.2	61.5	76.2	45.5	54.3	68.4
270	53	36.2	48.1	61.7	35.3	44.2	56.6
325	44	27.8	40.0	49.4	26.9	38.0	44.1
400	37	24.1	32.9	40.6	22.8	34.2	36.5
- 400	-37	22.5	30.9	34.8	21.6	29.5	32.4

Table 3.6 Effect of grind fineness on the recovery of Cu and Mo in MZ2HE rougher flotation at 25 % and 35 % + 100 mesh grind targets.

Test ID	p80, μm	Concentrate weight, %	Rougher concentrate			
			Assay, %		Recovery, %	
			Cu	Mo	Cu	Mo
T5a	132	4.29	12.5	1.032	92.5	85.8
T6a	195	4.65	11.7	1.079	82.9	84.6

Table 3.7 Effect of grind fineness on the recovery of Cu and Mo in the LSE rougher flotation at 25 % and 35 % + 100 mesh grind targets.

Test ID	p80, µm	Concentrate weight, %	Rougher concentrate			
			Assay, %		Recovery, %	
			Cu	Mo	Cu	Mo
T1a	148	4.17	20.2	0.678	88.5	82.5
T2a	220	4.11	18.2	0.554	79.1	74.0

Table 3.8 Effect of grind fineness on the recovery of Cu and Mo in the MZ2S rougher flotation at 25 % and 35 % + 100 mesh grind targets.

Test ID	p80, µm	Weight, %	Rougher concentrate			
			Assay, %		Recovery, %	
			Cu	Mo	Cu	Mo
T3a	146	4.42	22.5	0.922	91.2	75.6
T4a	205	4.15	21.1	1.064	87.6	80.8

CHAPTER 4

IDENTIFICATION OF TRACE MINERAL PARTICLES IN FLOTATION TAILINGS USING RAPID SCAN RADIOGRAPHY

4.1 Introduction

New processing technology for improved productivity and efficiency is the key to success in today's highly competitive market place. It has been well established that appropriate analytical control systems can provide such improvements. This is especially true of the particle separation processes used in the coal and mineral industries (Miller and Lin, 1988, 2004, 2009, 2013; King and Schneider, 1993). As the technology advances, the industry is always looking forward to a better technique for mineral characterization. Most present methods rely on heavy liquid fractionation, or on microscopy observation of a series of thin or polished sections (King and Schneider 1993) of the particulate sample. Optical microscopy is an invaluable tool for mineralogical characterization of ores and rocks. The minerals are identified from their optical properties. The optical properties differ from mineral to mineral because their crystal structure is different, as well as the chemical constituents of the mineral; also, their relative positions in the crystal lattice sites differ. However, it becomes difficult to

identify all minerals using only the optical microscope because there are cases where the optical properties of one mineral very closely resemble another (King and Schneider, 1993; Sutherland, 1998; Das et al., 2008). In addition, the traditional examination methods for multiphase mineral particles using 2D polished section images by optical microscopy is extremely time consuming, labor intensive, and has many limitations, including long sample preparation time, biased sampling, limited information, and consistent overestimation of the extent of liberation (Miller and Lin, 2004, 2009).

Therefore, a nondestructive technology (NDT) method called XMT has been developed for 3D mineral particle examination with the advantages of simple sample preparation, shorter analysis time, and statistically reliable accuracy and confidence of identification for multiphase minerals (Miller et al., 2009). As the resolution and the techniques for 3D analysis have advanced in the last decade, it is now possible to map in detail the microstructure and texture of multiphase particulate systems in 3D digital space (Miller and Lin 2009; 2013).

For trace mineral components such as molybdenite, the content is in the range of parts per million (ppm), which means that millions of particles must be examined to provide statistically reliable accuracy and confidence in the characterization analysis. HRXMT offers a quantitative imaging capability that can produce high resolution 3D images of the internal structure of multiphase particulate samples at a resolution of several μm (Miller and Lin, 2004, 2009) with a sample size of 1000x1000x1000 or about 1000 million voxels (volume elements). Another issue is sample analysis time for characterization, especially for trace mineral components. It should be noted that a full 3D tomography scan usually takes about several hours to half of a day depending on the desired voxel

resolution, 5 to 1 μm, respectively. In the case of HRXMT, thousands of projections of the sample may be needed, whereas in the case of radiography a projection of only a few seconds is used for analysis.

In this research, rapid scan dual energy (DE) radiography including a calibration procedure was used to evaluate and isolate trace mineral particles, such as chalcopyrite and molybdenite in flotation tailings at the ppm level. Dual energy (DE) radiography is the simplest and easiest option of multi-energy radiography. DE radiography involves taking two radiographic images at both high and low energy levels, and using the results of both scans to calculate the relative reflex and the effective atomic number, leading to elemental analysis. Rapid scan DE radiography is time efficient, especially compared to HRXMT. For example, more than 40,000 particles, 150x75 μm in size, can be interrogated in less than 15 minutes and the composition of particles containing high-density mineral phases estimated. After DE radiography scanning, these trace particles can then be isolated for detailed analyses such as liberation/exposure analysis by HRXMT and/or selected for surface characterization using XPS, ToF-SIMS, or other analytical instruments. Rapid scan DE radiography can also be used for the examination of drill core samples, tailings samples, or any other particulate sample containing trace mineral particles. In this chapter, first, the procedure for calibration will be demonstrated and then applications given to identify mineral particles using DE radiography.

This research provides an alternative way for mineral characterization using the DE method of the X-ray system in order to reduce the experimental cost and lead time, improve data accuracy, and data reliability. Mineral particles in monosize distribution can be identified with the relative reflexes and thickness. Each radiographic image can be

acquired in a very short time and is able to analyze several million particles.

4.2 Basic principles of DE radiography

4.2.1 Background and basic theory

Details about the theory and the principles of general radiography are available in many textbooks such as Martensen (2010) and Kahn and Gaskin (2012). Use of DE radiography was described early in the 1970s for medical applications (Alvarez and Macovski, 1976; Brody et al., 1981; Cardinal and Fenster, 1990). Later in 2002, consideration of applications in the mineral industry was reported (Schena et al., 2002, 2003). Reviews of the theory of DE radiography for material characterization are briefly summarized in the literature (Heaven et al., 2010; Schena et al., 2003). Several patents described a DE X-ray method imaging the fast moving material on a conveyer belt and using these images to calculate the grade of the stream (UK patent GB 2083618, 1982; US patent 6122343, 2000). X-ray radiography can be used to produce a 2D map of X-ray attenuation coefficients of irradiated ore samples. The intensity of the X-ray traveling through a mineral particle is attenuated (McCullough, 1975). As demonstrated in Figure 4.1 (a), a monochromatic X-ray of energy, E, and incident intensity (number of photons/unit time and area), I_0, on passing through local material, that absorbs X-ray photons and having a thickness, x, will have a transmitted intensity, I, given by:

$$I = I_0 \cdot exp\,(-\mu(\rho\,, Z, E) \cdot x) \tag{3}$$

where μ is the linear attenuation coefficient, depending on density, ρ, atomic number, Z

and the energy of the X-ray beam, E.

By taking the logarithm of the ratio of incident and transmitted intensity, Equation 3 can be rearranged as:

$$\ln(I/I_0) = -\mu(\rho, Z, E) \cdot x \tag{4}$$

As mentioned before, depending on the sample density, atomic number, thickness and the X-ray energy, the attenuation coefficient of the material can be determined as (Van Geet et al., 2001):

$$\mu = \rho(a + bZ^{3.8}/E^{3.2}) \tag{5}$$

where ρ is the bulk density, Z is the effective atomic number of the material, E is the X-ray energy, a and b are constants, which are energy dependent. As shown in Figure 4.1 (b), the log transmission through two minerals, A and B, is the sum of the log transmission of each mineral:

$$\ln(I/I_0) = -\mu_A(E) \cdot x_A - \mu_B(E) \cdot x_B \tag{6}$$

Equation 6 consists of two unknowns (x_A and x_B), which can be solved from radiography measurements at two energy levels (low and high).

$$\ln(I_L/I_{0L}) = -\mu_A(E_L) \cdot x_A - \mu_B(E_L) \cdot x_B \tag{7}$$

$$\ln(I_H/I_{0\mathrm{H}}) = -\mu_A(E_H)\cdot x_A - \mu_B(E_H)\cdot x_B \tag{8}$$

Then, the unknown thicknesses (x_A and x_B) can be solved as:

$$\begin{aligned} x_A &= (\mu_B(E_H)\cdot LA_L - \mu_B(E_L)\cdot LA_H)/\Delta \\ x_B &= (-\mu_A(E_H)\cdot LA_L + \mu_A(E_L)\cdot LA_H)/\Delta \end{aligned} \tag{9}$$

where Δ, LA_L and LA_H are :

$$\Delta = \mu_A(E_L)\mu_B(E_H) - \mu_A(E_H)\mu_B(E_L)$$

$$LA_L = \ln(I_{0L}(E_L)/I_L(E_L)) \text{ and } LA_H = \ln(I_{0H}(E_H)/I_H(E_H))$$

The log of the attenuations, LA_L and LA_H, are measured at each pixel for both the low-energy and high-energy radiographic images.

Basically, two methods were used to identify and isolate mineral particles from gangue minerals based on the radiography theory. Method 1 involved the calculation of the effective atomic number of minerals based on the relative reflexes between two energy radiographies and its corresponding main sample. Method 2 involved the estimation of relative thickness and was used, as a calibration standard to evaluate accuracy in the prediction of the thickness of high and low density minerals and its corresponding audit sample. Method 1 is more practical, but method 2 can provide a more accurate assessment of analytic variability.

4.2.2 Calculation of effective atomic number

Initially, the effective atomic number can be estimated based on the relative reflex from DE radiography. For two energy levels (low and high), Equation 3 can be written as:

$$I_{(E_i)} = I_{0_{(E_i)}} \cdot exp(-\mu(\rho, Z, E_i) \cdot x);\ i = Low, High \tag{10}$$

Differentiation of mineral phases within the sample is complicated because the linear attenuation coefficient, μ, at each voxel depends directly on the electron density, the effective atomic number, $Z_{eff,}$ of the material comprising the sample, and the energy of the X-ray beam, E. A simplified equation that illustrates the approximate relationship among these quantities is a general form of Equation 5:

$$\mu(E_i) = \rho[\alpha(E_i) + \beta(E_i) \cdot Z^p] \tag{11}$$

where the functions $\alpha(E_i)$ and $\beta(E_i)$ define the energy dependence of Compton and photoelectric effects, respectively. For the mineral system in this study, the p is set as 3.8. The effective atomic number is simplified, as $Z_{eff} \equiv Z$ and the radiography reflex is defined as:

$$R(E_i) = R_i = \ln(I_{0,i}/I_0) \tag{12}$$

at a specific energy level, E. Then, Equations 11 and 12 can be combined as:

$$R(E_i)/(\rho \cdot x) = \mu_m = [\alpha_i + \beta_i \cdot Z^p] \cdot Z) \quad (13)$$

where $\mu_m = {}^{\mu}/_{\rho}$ is the mass attenuation coefficient. Based on the operating energy range (40 kV to 150 kV for the DE radiography), the DE radiography technique involves both the Compton and photoelectric effects with $p \approx 3.8$ for this study. Three known materials and measurements in a specific energy range using the DE radiographic technique (Naydenov et al., 2003) can calculate the effective atomic number of an unknown material. In this case, the relative reflex of two radiographs, $X = R_1/R_2$ plays the principal role in the estimation of the effective atomic number, Z_{eff}, of an unknown material. From Equation (12),

$$X \equiv R(E_1)/R(E_2) = \mu_m(E_1)/\mu_m(E_2) = \mu(E_1)/\mu(E_2) \quad (14)$$

Therefore, *X* depends only on the effective atomic number and does not depend on the geometry (thickness, *x*) or the density (ρ) of the material nor does it depend on its other physicochemical properties.

In this way, the Z_{eff} of an unknown material can be estimated based on DE radiography.

$$Z_{eff} = ((k_1 \cdot X + k_2)/(k_3 \cdot X + k_4))^{1/p} \quad (15)$$

where $X = R_1/R_2$ is the relative reflex from two radiographs at different energy levels (high and low), and the calibration coefficients k_1, k_2, k_3 and k_4 are determined from the

relative reflexes of three known materials as described by the following equations.

$$k_1 = Z_1^p \cdot Z_2^p \cdot (X_1 - X_2) - Z_1^p \cdot Z_3^p \cdot (X_1 - X_3) + Z_2^p \cdot Z_3^p \cdot (X_2 - X_3)$$

$$k_2 = X_1 \cdot X_2 \cdot Z_3^p \cdot \left(Z_1^p - Z_2^p\right) - X_1 \cdot X_3 \cdot Z_2^p \cdot \left(Z_1^p - Z_3^p\right) + X_2 \cdot X_3 \cdot Z_1^p \cdot \left(Z_2^p - Z_3^p\right)$$

$$k_3 = X_1 \cdot \left(Z_1^p - Z_2^p\right) - X_2 \cdot \left(Z_1^p - Z_3^p\right) + X_3 \cdot \left(Z_1^p - Z_2^p\right) \quad (16)$$

$$k_4 = X_1 \cdot X_2 \cdot \left(Z_1^p - Z_2^p\right) - X_1 \cdot X_3 \cdot \left(Z_1^p - Z_3^p\right) + X_2 \cdot X_3 \cdot \left(Z_2^p - Z_3^p\right)$$

where X_1, X_2 and X_3 are the relative reflexes of three known materials using the DE method; Z_1, Z_2 and Z_3 are their effective atomic numbers, and p is set as 3.8. The calibration constants depend upon the chosen energy values used in the radiation source, characteristics of the detector, etc., but not upon properties of the material. These constants are determined from a series of test measurements using objects of known composition and geometry.

Generally, this method provides the capability to calculate the effective atomic number of unknown minerals using the DE method. The DE method works well as long as the energy range for each measured element does not involve the K-edge effect. With the effective atomic number and mineralogy of the sample, the unknown material can be characterized.

4.2.3 Estimation of effective thickness (relative composition)

Heaven's work (Heaven et al., 2010) reported a thickness calculation based on the dual energy method and two known materials using the following transformation. To characterize the gangue minerals (silicate) and trace mineral component (high density,

high Z) using the DE radiographic technique, aluminum (Al) and copper (Cu) were chosen as materials A and B, due to their similarity to the attenuation coefficients for gangue (quartz) and high density trace minerals (chalcopyrite, molybdenite), as shown in Figure 4.2. Polychromatic X-ray sources provide X-ray photons with a distribution of energy levels and the photon absorption needs to be solved with a nonlinear function for the log attenuation values.

As shown by Cardinal and Fenster (1990), the approximate solution for a polychromatic X-ray source, a simplified equation that illustrates the approximate relationship for unknown thickness (x_A and x_B), can be solved as:

$$x_A = \frac{a_0 + a_1 L + a_2 H + a_3 L^2 + a_4 LH + a_5 H^2}{1 + b_0 L + b_1 H}$$
$$x_B = \frac{c_0 + c_1 L + c_2 H + c_3 L^2 + c_4 LH + c_5 H^2}{1 + d_0 L + d_1 H} \quad (17)$$

where x_A and x_B are the thicknesses of A and B for each pixel in the reconstructed images for the two known materials, respectively. The 16 unknown coefficients $a_{0\ldots5}$, $b_{0,1}$, $c_{1\ldots5}$, and $d_{0,1}$ can be estimated from calibration of low- and high-energy radiographic images with a combination of 5 known thickness levels for both materials, A and B.

4.3 Materials and methods

4.3.1 DE radiography

The high-resolution X-ray micro computed tomography (HRXMT) system at the University of Utah has been the main instrument used to acquire DE X-ray radiographs. Major external and internal components of the Xradia MicroXCT-400 machine are shown in Figure 4.3 and Figure 4.4, respectively. Based on a polychromatic focal X-ray source, the scan conditions have been considered and optimized in order to obtain high quality images. As the most important consideration of the DE method, the source energy is set at 80 kV for the low-energy level, which is satisfactory for Cu mineral scans, and at 140 kV for the high-energy level, which is mostly for high density minerals such as galena and gold. The lens magnification was set at 4X, providing an image resolution of around 5 μm per pixel, and a field of view approximately 5 mm by 5 mm.

This magnification meets the need for particle size classes from 1 mm to 50 μm; a physical 150 μm thick glass filter is used to remove the noise caused by low energy X-ray photons, and to improve the contrast of silicate minerals. In order to have an appropriate field of view, the distances between the sample to source and sample to detector, are set at 20 millimeters and 44 millimeters, respectively. The effect of scattered radiation is excluded.

The exposure time is set at 5 seconds per radiograph to obtain sufficient X-ray photon counts for the sample. Binning is set at 2 for a moderate exposure time and image quality, which goes to 1024 pixels on the X and Y axes. Finally, the image for measurement is an average of 10 radiographs.

Both sample sets were compressed to 1 millimeter thickness by plastic plates

(76.2x25.4x1.0 mm) from both sides, and stabilized by double-sided tape on one side of the plastic slide. The slides and tape helped keep the sample fixed on the sample stage while absorbing only a small amount of X-ray photons, which were resolved by references.

4.3.2 Sample preparation and standard calibration

Two sets of samples were prepared for calibration of DE measurements. The first sample set was assembled of six different minerals. This sample set was measured by three known materials to calculate an unknown material effective atomic number following Naydenov's work (Naydenov et al., 2003). Aluminum and Cu foils comprised the second sample set following Heaven's work (Heaven et al., 2010).

4.3.3 Experimental procedure

Rapid scan DE radiography was used to locate the high and medium density minerals with a series of radiographic images taken at both a high- and low-energy levels in a very short time.

A step-by-step experimental procedure of rapid scan DE radiography is included in Appendix C. In order to obtain a quick and accurate evaluation by radiographic analysis, monosize particle distribution must be organized for sample preparation. These conditions not only help identify specific mineral phases by quick radiographic evaluation, but reduce misinterpretation caused by the transmission distance, similar minerals, or particle size.

If the attenuation coefficient of the objective mineral is much higher than that of the

host minerals, it will be much easier to identify and locate a specific mineral. To enhance the image contrast, the distance of the source/detector, exposure time and physical filters should be considered to establish a high quality radiograph.

4.4 Results and discussion

4.4.1 Determination of unknown coefficients

The DE radiographic procedure allows for calibration specific to minerals of interest with improved discrimination and accuracy. In addition, the DE technique requires that data be collected at two energies sufficiently different to define primary contributions from photoelectric interactions and Compton scattering.

To determine the unknown coefficients $a_{0\ldots5}$, $b_{0,1}$, $c_{0\ldots5}$ and $d_{0,1}$ of Equation 16, DE pairs from radiographs for an Al step-wedge and a Cu step-wedge standard, or reference, were used for calibration. In this regard, the Al foil and Cu foil are stacked as interlaced layers, as shown in Figure 4.5 (a). Each Cu foil has a thickness of 35 μm, and each Al foil has a thickness of 110 μm. In this way, 5 Cu foil samples and 5 Al foil samples were combined and glued on the plastic plates. A total of 36 sections were measured with each section being approximately a 0.3mm x 0.3mm square area. Radiographs of the Al and Cu wedges stacked for DE calibration at 80 kV and 140 kV are shown as Figures 4.5 (b) and 4.5 (c), respectively.

Averaged radiographic images for reference materials were taken following the same scan conditions specified in Section 4.3.1 using the absorption mode. The Al foil samples of increasing thickness were stacked from left to right (alphabetic sequence from A to F) and Cu foil samples of increasing thickness were stacked from top to bottom (numeric

sequence from 1 to 6).

The log transmission results as well as the actual thickness of the Al and Cu for each rectangle were input into a Microsoft Excel spreadsheet. The unknown coefficients can be determined using a minimization solver (Brown, 2001). Once values of corresponding coefficients have been determined, the calculated thicknesses of Cu and Al foils can be determined using Equation 16. In this study, the generalized reduced gradient method built into Excel's solver tool (Brown, 2001) was used to fit the data from Table 4.1. The measured thickness of these Al and Cu wedge steps are listed in the top row and the left column of Table 4.1. The measurements of the log attenuation values corresponding to the sections of Al and Cu wedges acquired from radiographic analysis at DE levels of 80 kV (white column) and 140 kV (gray shaded column) are listed in Table 4.1. ImageJ software (National Institutes of Health: http://rsbweb.nih.gov/ij/) was used to measure relative intensities of the radiographic images. To minimize registration errors with the wedges, the horizontal and vertical edges of the wedges were used as fiduciary landmarks; the top and bottom of the wedge steps are parallel. The step outlines were made with ImageJ well away from the edges of the steps. Low (L)- and high (H)– energy images of the stacked wedges were used for calculation of the coefficients for Equation 16.

The measured mean pixel values in a region of interest in both high and low energy images from each of the 25 rectangles were used to convert to the negative log of the energy transmission, $-ln(I_{rectangle}/I_{air})$ values, to obtain the data in Figure 4.5. The actual thicknesses of the wedges were measured 3 times with a Duratool electronic micrometer. As presented in Table 4.2, after 10 iterations, values of corresponding

coefficients $a_{0\ldots5}$, $b_{0,1}$, $c_{0\ldots5}$ and $d_{0,1}$ for Equation 16 were determined. The spreadsheet calculations adjusted the unknown coefficients iteratively to determine the coefficients that produced the best fit between the actual thicknesses and the calculated thicknesses.

The calibration data and the corresponding coefficients are only valid for the imaging parameters reported in this work. Changes of the kV, X-ray generator, sensor, source-to-detector distance, or the calibration wedges would necessitate obtaining new calibration images, collection of data, and calculation of new coefficients. To determine the accuracy of the coefficients, 25 calculated thicknesses were compared to the measured thicknesses with the corresponding standard deviation, as shown in Figure 4.6, from section A1 to E5.

Similarly, 25 reconstructed measurements are plotted for each Cu step-wedge. It is noted that a highly significant correlation is found between the measured step-wedge thickness and the calculated thickness from DE radiography for the Cu wedge. Furthermore, a prediction of Al and Cu wedge thicknesses for sections A6 and F6 are also calculated and presented in Table 4.3. However, a larger spread in Al thickness for each step is observed from the result of Table 4.3. It is expected that the noise is higher for the calculated Al foil thickness (low density material) than for the Cu foil thickness (high density material) (Gauntt and Barnes, 1994). The standard deviations of each section are less than 3 %. The coefficients are acceptable for the level of accuracy desired.

Second, samples consisting of six different materials (quartz, aluminum, copper, molybdenite, gold and lead) were prepared for the determination of effective atomic numbers using DE radiography measurements. The positions of the calibration materials

(quartz, aluminum, copper, molybdenite, gold, and lead) and related DE radiographs acquired at 80 and 140 kV are shown in Figure 4.7.

In this case, aluminum, copper and lead were selected as known materials. These three elements can represent the three different mineral phases usually present in samples from metal mining operations having low attenuation coefficients (gangue, quartz/silicates), medium attenuation coefficients (copper, most base metal minerals) and high attenuation coefficients (molybdenite, galena, lead or other precious metals). Quartz, molybdenite and gold were selected as the unknown materials for validation. Although the plastic plates and double-sided tape absorb some X-ray photons, this does not matter since the ratio is taken and the absorption contribution is the same for each mineral sample. Material information used for the determination of effective atomic numbers based on DE radiography is listed in Table 4.4. Samples were arranged in a 5mm x 5mm area and 4X magnification used for each single projection (radiograph), without moving the sample or the source/detector. Coefficients $k_1, k_2, k_3,$ and k_4 were then calculated according to Equation 15 using $p = 3.8$. Yielding, $k_1 = 1.37 \cdot 10^{12}$, $k_2 = -1.20 \cdot 10^{12}$, $k_3 = -1.15 \cdot 10^{6}$ and $k_4 = 6.57 \cdot 10^{5}$.

The calculated effective atomic number was then compared to the real effective atomic number to determine the accuracy in data correlation. Figure 4.8 shows the estimated and actual effective atomic numbers based on the relative reflex of the two radiographs, X. Since the polychromatic maximum energy for this instrument is about 150 kV and 10 watts flux, these settings could be insufficient for the reflex to determine the high effective atomic number for materials such as gold. In this regard, instrument capability could limit identification to material with an effective atomic number less than

40. Also, the impurity of gold could affect the experimental result. A universal dependence has been predicted for the effective atomic number as a function of relative radiographic reflex. The established theoretical law is nearly confirmed by the experimental data presented.

4.4.2 Applications of rapid scan DE radiography

A very important part of using rapid scan DE radiography is the creation of an accurate and complete mineral reference library (MRL) that is used to classify the minerals in a sample or sample suite. The MRL is made up of mineral names or mineral attenuation coefficient groupings associated with the relative reflex of two energy level (low and high) radiographies. To evaluate the feasibility and accuracy of identification for a rapid search and isolation of the lost mineral particles in flotation tailings, 9 different mineral particles with 150x75 μm size, which were separated from the KUC ore sample, were spread on the double sticky tape on the plastic plates. Results are shown in Figure 4.9 (a) and the DE radiograph acquired from the indicated region as shown by Figure 4.9 (b).

Minerals listed in Table 4.5 are the most abundant minerals of the copper porphyry ore samples from the Bingham Canyon mine, KUC, and confirmed and isolated by the Geological Department at the University of Utah from pure minerals. The actual effective atomic numbers of the reference minerals were calculated by a standard equation (Taylor et al., 2009) and their densities can found at http://www.mindat.org/ (Ralph and Chau, 1993). Preliminary results indicate the mineral particles with high effective atomic numbers, Z_{eff}, are identified very well as shown in Figure 4.9. Using the same scan

conditions and the same coefficients obtained in Section 4.4.1, these nine pure minerals were scanned to verify the accuracy of the coefficients K_1, K_2, K_3 and K_4. As shown in Figure 4.9 (b), the dark grey area represents minerals with high density/high atomic numbers, the midgrey areas represent the medium density/medium atomic number minerals, and the light grey areas indicate the surrounding background and low atomic number minerals. In most cases, the region of interest (ROI) of the mineral could contain different materials with different transmission values. Porosity (air or water) and impurities of the selected mineral (molybdenite containing a talc inclusion), for example, may affect calculation of the mean relative reflex value.

Specially, one needs to consider the partial volume effect (PVE) of the ROI on the radiography image and all these effects should be removed before statistical analysis. If particles are surrounded by background, PVE definitely occurs, as shown in Figure 4.10.

If this is the case, a ROI of a mineral can be manually drawn, and the mean value of counts in that region can be calculated for determination of the mean pixel value. The method to correct or consider the impurity and porosity of a mineral is to determine the confidence interval of the intensity value. A confidence interval gives an estimated range of intensity values that is likely to include an unknown population parameter, the estimated range being calculated from a given set of sample data. The formula for the confidence interval (CI) of the mean of the relative reflex as presented in the Equation 18.

$$CI = sample\ statistic \pm margin\ of\ error = \bar{X} \pm Z(S/\sqrt{n}) \tag{18}$$

In this formula, $\bar{X}$ is the mean of the intensity data; Z is the interval coefficient, which

can be found from the normal distribution table (for example, the interval coefficient for a 95% confidence level is $Z = 1.96$), S is the standard deviation of the data and n is the pixel numbers. The margin of error ($\pm Z\frac{S}{\sqrt{n}}$) of a confidence interval is defined to be the value added or subtracted from the sample mean which determines the length of the interval.

In this particular case, 9 different minerals with their specific relative reflexes have been determined. The confidence intervals for each mineral can be calculated separately, as shown in Figure 4.11. Bubble charts are popular tools for identifying and illustrating measurement clusters. Essentially, these bubble charts allow four different variables to be plotted within the same graph, making it easy to assess the relative statistical performance. For example, each mineral circle, identified by color and size, is plotted on the chart based on the relative reflex (x-axis) and the effective atomic number (y-axis). The size of the circle represents the confidence interval of intensity values of the relative reflex for each mineral.

As shown on Figure 4.11, some bubbles such as chalcopyrite and sphalerite are overlapping. Using this method, it is easy to differentiate elements with a large difference between their effective atomic numbers; for example, it is easy to tell the difference between quartz ($Z_{eff} = 11.8$) and molybdenite ($Z_{eff} = 36.4$). However, for minerals with closer atomic numbers, such as chalcopyrite ($Z_{eff} = 25.0$), azurite (Z_{eff}~24.5) and sphalerite ($Z_{eff} = 25.4$), it is impossible to differentiate them using DE radiography. Of course, there is another way to improve accuracy of radiographic inspection. Further, multi-energy approaches (3 or 4 energy levels) may be capable of discriminating these minerals.

The estimated effective atomic numbers used the coefficients K_1, K_2, K_3 and K_4, which were determined from standard calibration with $p = 3.8$. These are then compared to the actual effective atomic numbers to determine the accuracy in data correlation, as shown in Figure 4.12. Figure 4.12 shows how close the estimated effective atomic numbers based on the relative reflex of the two radiographs, X, were to their actual effective atomic numbers. The standard deviations of the values of effective atomic numbers are less than 10 %. The coefficients were acceptable for the level of accuracy needed to locate and identify desired particles. However, a wider spread of effective atomic numbers of high density and high attenuation coefficient minerals was observed in Figure 4.12.

It is noted that the maximum energy of the X-ray system was not enough for the relative reflex to determine high effective atomic number materials such as galena and barite. It is expected that DE radiography uses X-rays to determine the attenuation coefficients; but it is very dependent on the ability of the X-rays to penetrate the sample. This means that for higher density minerals, the machine in use may not be able to produce X-rays with a high enough energy to go completely through the sample. Therefore, this further limits which minerals can be identified using DE radiography. Such reference minerals rarely occur in the KUC flotation tailings.

General mineralogical characterization of the Cu rougher tailings revealed that apart from the gangue minerals, the main sulfide minerals are chalcopyrite, pyrite and molybdenite. Some amount of covellite and iron oxide minerals such as hematite were also present. A histograms of the relative reflex of these common minerals in the KUC rougher tailings is presented in Figure 4.13. Data were analyzed and displayed in a

histogram (a column chart that displays frequency data) by using the histogram tool of Minitab 16 software (Minitab, 2011).

To create a histogram, the radiography data were organized in two columns that contain input data and frequency or bin numbers on the worksheet. Input data are the data of relative reflexes of each mineral to be analyzed. Molybdenite particles selected for calibration analysis based on optical microscopy appeared to be completely liberated, smooth and pure. However, as seen from Figure 4.13, there was an unusual overlapping between the relative reflex values of molybdenite and bornite, causing suspicion that this could be due to inaccuracy in identifying the molybdenite particle. The particle was further carefully examined by SEM analysis, which revealed the presence of some silicates and pores. Hence, it is understood that porosity and impurity impacts the X-ray intensity values of the selected minerals. This phenomenon is also observed in oxidized minerals like malachite and hematite. The results of this investigation are summarized as follows:

1. Based on the relative reflex of MRL data, all minerals in the flotation products can be grouped into three main categories (high, medium, and low) by effective atomic numbers and attenuation coefficients.
2. High and medium attenuation coefficient minerals (molybdenite and chalcopyrite) can be easily differentiated from gangue minerals based on the relative reflex of two radiographs.
3. The basic weakness of the DE radiography method is that it is difficult to differentiate minerals with similar effective atomic numbers such as chalcopyrite and sphalerite or pyrite and iron oxide, leading to errors in the elemental analysis

and particle identification, as exemplified in Figure 4.13.

4. The accuracy of mineral identification was found to be at $Z_{eff} \geq 26 \pm 6$ for high and medium density minerals depending upon many variables such as characteristics of the X-ray source (non-monochromatic), statistical and other fluctuations, including poor energy resolution, noise, scattered radiation and porosity or impurity of material.

To verify and to further evaluate the feasibility of the rapid search and isolation of trace mineral particles, a sample with 150x75 μm particle size from flotation tailings was prepared and several molybdenite particles of the same size placed at known positions within this sample. DE radiographs were acquired from 40 (4x10) adjacent regions and show stitched images of different locations. The stitched images were composed of a total of 40 – 50 images per one slide. The projection region for each radiograph image is 25 mm^2 containing about 450 - 500 particles and the total projection time for a single DE radiographic image and the reference image took 15 seconds. In addition, a reference image was taken at both low and high energies for every slide so that a correct reference could be applied for every slide. As stated in Section 4.2.2, the reference image normalizes the attenuation coefficients to a percentage of the transmission. This essentially makes the difference between the attenuation coefficients larger, increasing the contrast in the image. Figure 4.14 illustrates the identified molybdenite particles found in the center image of the bottom images in Figure 4.14 (b). Then, identified molybdenite particles were confirmed by optical microscopy, as shown in Figure 4.14 (c). Several particles containing Cu sulfide mineral with a lower effective atomic number than molybdenite were placed in the sample slide. Each radiographic image can

be acquired in a very short time and is able to analyze several millions of particles per day. In addition, for identification of Cu sulfides in drill core samples without the detailed analyses of association and liberation, DE radiography was applied. Results indicate that larger cores up to 25 mm can be imaged, but smaller samples were the focus in this situation. Cubic Cu ore particles (3x3x3 mm) were prepared and DE radiographs were acquired, as shown in Figure 4.15. As shown in Figure 4.15, results indicate that Cu sulfides are identified with a reconstructed thickness of less than 0.2 mm inside the 3 mm thickness cubes. The gray scale indicates thickness from 0 mm (black) to 0.256 mm (white). It is also noted, as expected, the reconstructed thickness of the rock block is slightly higher than the actual thickness (3 mm). From such measurements, the volume percent of the sulfide minerals for the three cubic Cu ore particles (3x3x3 mm) can be determined, as shown at the bottom of Figure 4.16.

HRXMT is a nondestructive technique that has the capability to generate 3D images of particulate beds. In this regard, to further evaluate the accuracy using DE radiography, these three cubic Cu ore particles were scanned by HRXMT. In practice, when raw data collected from HRXMT analysis were processed to generate 3D reconstruction of the sample, the attenuation coefficient values in each voxel were translated to scaled CT number values. Scaled CT number values are used in the classification process for identification of the different minerals. More detailed information about the scaled CT number and identification of minerals is presented in Chapter 5.

Generally, the HRXMT equipment is calibrated using standard pure Cu mineral samples (Miller and Lin, 2013). A scaled CT number range is assigned to each pure mineral. In this way, the identification of the different mineral phases is accomplished in

the scanned samples according to the scaled CT number values. Comparison of the radiographs and 3D tomography images from a similar viewing angle is shown in Figure 4.17. For volume rendering of 3D images, sulfide mineral grains were set as a brown color, pink was set for mineral phases with attenuation coefficients higher than chalcopyrite and the gangue phase was set as a semitransparent green color. The estimation of the composition in volume percent from a 3D tomography image is included in the bottom row for comparison. As expected, the estimate from DE radiography is underestimated due to the use of the Cu calibration wedge, which has a higher X-ray attenuation coefficient than most of the Cu minerals. Based on 3D tomography analysis of the samples, the proposed DE radiography technique was indeed faster and more time efficient than only X-ray tomography or QEMSCAN analysis and the potential additional data that could be gathered made this technique worth exploring for future projects, especially if it involves identification of trace particles concentrated on a small, parts per million scale. DE radiography provides some limited but important key information by shooting just two radiographic images in a few seconds, while a detailed examination such as HRXMT and QEMSCAN, usually takes a few hours to a day.

In other words, based on sampling statistics during DE radiography inspection, huge amounts of detailed data significantly increase the possibility of finding the desired particles (molybdenite) in low concentration products such as flotation feed and tailings.

Secondly, the scan is a 2D image of all sample particles, providing the spatial location of a specific region or selected particle. The noninvasive, nondestructive sample preparation and scan procedure allow the desired minerals to remain in the sample for further analysis. Thirdly, sample preparation and prescan time is easy and short. In this regard, rapid scan DE radiography can recognize the region of the sample containing the targeted mineral phase

first, then a complete characterization analysis such as HRXMT, SEM-EDS, and XPS analysis can be implemented to characterize the specific mineral phases, as shown in Figure 4.18. Finally, the technique was demonstrated for fast geometallurgical analysis such as identification of heavy metal minerals, specifically Cu and Mo sulfides, and an estimate of their amount in run-of-mine ore and trace heavy metal particles in flotation tailings. In the future, the DE method will be able to integrate the rapid-radiography scan for a complete examination procedure before the HRXMT scan as a more accurate choice.

4.4.3 Identification of lost minerals in KUC rougher tailings

4.4.3.1 Data acquisition and file conversion

As previously mentioned in Section 3.3.4, approximately 3 - 5 g of representative sample portions were obtained using a rotary sample divider from rougher tailings, and spread over plastic plates for preparation of a sample suitable for rapid scan DE radiography examination. A total of 120 slides of rougher tailings samples of three different Cu ore types (MZ2S, LSE, and MZ2HE) from KUC ore for the whole project have been prepared and considered for identification and isolation of lost sulfide minerals, such as molybdenite and chalcopyrite, using this method. In other words, each ore type was compared in two categories of grind fineness (coarse and fine) and examined for two coarse size classes (50x100 mesh, 100x200 mesh) from each grind fineness. Ten slides were prepared from each size class. Several examples of the resulting scans are shown in Figure 4.19.

The DE radiography scans are completed by splitting the slide into 40 sections, making a 4x10 grid, and scanning each section at a low-energy level (80 kV) and a high-

energy level (140 kV). These were scanned using the averaging mode on the Xradia MicroXCT-400 machine, taking 3 images at 5 seconds each to average together and produce a single image. Generally, all rougher tailings samples were scanned under the same conditions using rapid scan DE radiography. The scan conditions were set at the following: 4X magnification with 5 seconds exposure time; source voltages at 80 kV and 140 kV; the distance between source and detector -44 mm and 20mm; the detector binning at 2 with a 150 μm glass filter.

The Xradia MicroXCT-400 at the University of Utah provides applications called XMController and XMReconstructor (Xradia, 2010) for image acquisition and reconstruction. Radiographic images in 2D for both high- and low-energy levels were acquired using an averaging mode and visualized by XMController on the screen, and then saved as a radiography file pattern with extension .xrm. The XRM file contains information of X-ray intensity, coordinates, exposure time, source voltages, distances, etc. In addition to the internal image format (.xrm) from Xradia, several image formats can be exported, namely, tiff, jpeg, and raw.

According to the specifications of the MicroXCT-400, the maximum color depth of the CCD detector is 16-bit grayscale and radiography scans are saved in a grayscale, unsigned 16-bit (xrm) file. In the present study, it would be a time consuming process to export 80 radiographic images (both at high- and low-energy levels) using the XMController without losing original image data. It usually takes more than 20 minutes for each slide. In this regard, instrument capability limited conversion of radiographic images in a short time. After the DE radiography scans were completed, file conversion time from .xrm file to .bin file could be reduced approximately 200 times using the

corresponding Mathlab code, as shown in Appendix B. The binary file .bin format is the same format as the .raw file with simply a different extension. When all files were converted into .bin and/or .raw file, the calculation of the relative reflex was easily performed using Matlab software (Mathworks, 2012), according to Equations 11 and 13.

Once digital radiography images with .xrm file extensions were converted into 8-bit, grayscale, .raw files, which contain basic experimental values based on the pixel intensities of the relative reflexes, then the effective atomic numbers of each mineral could easily be calculated. In addition, the labeling of each file could contain some additional information. Having the assistance of the file name, the ore type, grind fineness, size class, number of slide, types of flotation products (concentrate, tailings and feed) and the corresponding location of lost particles on the slide could be defined. For example, a name of any radiographic image contains the following information:

LSE_oretype_finegrinding_plus100mesh_slide_1_roughertail_Section1x1.xrm

In Figure 4.19, note the darker particles in each radiography scan, these could be potential molybdenite minerals. Based on chemical analysis, the estimated numbers of lost chalcopyrite and molybdenite particles in KUC flotation tailings are presented in Table 4.6.

As previously stated, each slide consists of 40 radiographic image sections. Based on results of image analysis, one section contains approximately 450 – 500 particles. Each slide contains roughly 18,000 – 22,000 particles in the 300x150 μm size class, so a total of 220,000- 250,000 particles from each size class for each ore type could be imaged and analyzed using the radiographic method.

The average analysis time for each slide was approximately 15 minutes. Depending

on the Mo content in the rougher tailings, the number of slides scanned from each size classes was determined. If the Mo content was less than 0.003 %, approximately 10 slides were acquired. This enabled the characterization and classification of these mineral particles to be investigated. Therefore, an image-processing program was necessary to analyze the lost minerals in the flotation tailings, as presented in Section 4.4.3.2.

4.4.3.2 Image processing and data analysis

Image processing and data analysis are the next important steps after image acquisition and file conversion, because they allow for significant enhancement of the visibility of the details in the digital radiographs. The entire process is semiautomatic and high throughput. The automated determination of high atomic number minerals also eliminates some elements of operator error. There are several image processing software packages available such as ImageJ (Rasband, 1997), MIPAV (2007), and MATLAB (2012), some commercial and some open-source.

Once the relative reflex, described in Section 4.2.2, was found from the low- and high-energy scans using the appropriate Matlab code, it was saved as high resolution radiographic images with extension .raw. After importing them into ImageJ, a Threshold function was applied to these radiographic images. In general, good threshold can be selected if the histogram peak of the desired mineral is tall, narrow, symmetric, and separated by deep valleys. Commonly, flotation tailings are multiphase, heterogeneous materials consisting of several different minerals. In the multiphase case, such as in this research, a hysteresis (two levels) threshold, based on the pixel intensity histogram, is applied for phase segmentation. As mentioned previously, thresholding removes

unwanted background information, leaving behind only the desired particles themselves. Figure 4.20 shows the ImageJ tresholding function that segments the background from molybdenite. The dialog box, Figure 4.20 (a), was opened after the tresholding function was selected from the ImageJ menu bar. This histogram represents the distribution of pixel intensities of relative reflex in 2D; pixels above the high threshold are classified as molybdenite and below the low threshold as background. The lower and upper thresholding (sliders) were selected from the calibration results presented in Figure 4.12. In this case, all pixels between 0.74 and 0.82 represent medium/low density and medium/low atomic number minerals and the pixel intensities below 0.74 represent high density and high atomic number minerals in the sample. Using these tresholding values, the radiographic image, Figure 4.20 (b), was segmented into features of interest (molybdenite) and background (air and other minerals such as quartz, chalcopyrite and pyrite). While adjusting, the threshold molybdenite particles are displayed in red and the background is displayed in grayscale, Figure 4.20 (c). Once the thresholding function was applied to the radiographic image, the background became white, leaving only the black images of the desired particles, Figure 4.20 (d). Tresholding is not the final step for DE radiography. Based on the relative reflex of thresholded particles, the effective atomic number can be estimated for mineral identification.

Once all minerals with a high/medium density and a high/medium atomic number in the rougher tailings have been found in the radiography images, lost molybdenite and chalcopyrite particles can be located easily on the etched grid pattern. Isolation of desired particles from the slide was manually done using microtweezers or high precision cutting tweezers (TDI 14AGW-C) under simple optical microscopy. The microtweezers were the

best tool for picking up objects too small to be easily handled with the human hand. All lost particles isolated from the rougher tailings were collected into the cylindrical aligned container, subsequently undergoing further detailed analysis. Liberation analysis using HRXMT was performed initially.

In conclusion, a schematic diagram of the DE radiography method is illustrated in Figure 4.21 and the standard operating procedure broadly described in Appendix C. Generally, the samples to be analyzed are initially split into narrow size fractions, each size fraction distributed on projection plates, and the plates placed in the sample holder of the MicroXCT-400 for irradiation at two energy levels (DE analysis). A single projection image in 2D is captured by the detector, visualized on the screen according to the same scan conditions as a standard sample and then saved as a radiography file pattern with extension .xrm.

After completing the acquisition process at high- and low-energy levels, the averaged reference is established. The reference should be prepared for both high- and low-energy levels because each sample should have their own reference to remove X-ray attenuation of the background, air and any other effects associated with the lens in order to enhance image quality. All radiographic images are saved in the .xrm file after applying the reference. Based on a combination of these two images, the relative reflex of X-ray intensity can be calculated according to Equation 13, saved into a single radiographic file and then converted from .xrm to .bin using the Matlab software for image data analysis. As mentioned previously, one radiographic image is a relatively small image with 5x5 mm size but it contains 400 - 500 particles and analysis of this image requires considerable processing time. This method can find the desired particles in a very short

time by subtracting the background and/or unnecessary gangue particles using thresholding from the radiographic image.

In this research, this subtraction allows for isolatation of high density and high atomic number minerals such as molybdenite from other minerals. The thresholded image is used to calculate the effective atomic numbers of the particles for mineral identification.

4.4.3.3 Advantages and limitations of DE radiography

As mentioned before, radiography is one of the most important and widely used methods in nondestructive technology. Each radiographic testing method offers a number of advantages but each also has some limitations. A summary of advantages and disadvantages of rapid scan DE radiography is outlined in Table 4.7.

One of the important benefits of DE radiography scanning is consumption of considerably less disc space (4 megabytes/one image) than tomography. Use of less disc space helps save storage space and also allows low-end computers to process the image file under the system limitations.

4.5 Summary and discussions

The purpose of this work was to find an accurate, rapid, simple and easy method to locate lost valuable mineral particles from rougher tailings samples of three KUC ore types through their relative reflex of X-ray intensities using rapid scan DE radiography. All of the findings in this work are based on the analysis of several mineral particles covering a limited range of characteristics (particle size, effective atomic number, X-ray intensity and X-ray attenuation coefficient). Accordingly, the conclusions from these

findings might apply only to these types of samples.

The findings serve as a model and as an initial study. As with any research, the initial efforts define a starting point. Further work on other samples can then be considered in reference to these data and the findings can then be either generalized or more definitively qualified. A total of 160 slides were scanned by this method using the X-ray system. The theory and procedures are described for the evaluation and isolation of trace mineral particles from samples at the ppm level. In this regard, Al and Cu wedges were used as calibration standards to evaluate accuracy in the prediction of the thickness of high- and low-density minerals. In addition, the effective atomic number was determined based on the relative reflex from DE radiography. The results demonstrate the feasibility of DE radiography to identify mineral particles having a medium to high effective atomic number ($Z_{eff} > 26$), which is recommended for the identification and the isolation of trace mineral particles. Then, these trace particles can be isolated for detailed characterization analysis by HRXMT and/or selected for surface characterization using XPS, TOF/SIMS, or other analytical instruments. The DE measurements correlated well with micron measurement data taken for the Al and Cu wedges. In addition, it was concluded that the dual energy approach allows one to improve the inspection efficiency by an order of magnitude, in contrast to single energy methods.

The technique was demonstrated for rapid geometallurgical analysis and it was expected that several millions of particles per day can be interrogated using this proposed radiography method with an accuracy of up to 90%. Also, these developments can find application not only in rapid geometallurgical analysis (identification of heavy metal minerals, specifically Cu and Mo sulfides, and an estimate of their amount in run-of mine

ore and trace heavy metal particles in tailings), but also in areas such as identification of mineral zones from drill core samples, mineral resource evaluation, mine planning and the evaluation of separation efficiency of feed, tailings streams or any other particulate sample containing trace mineral particles. Preliminary results verify that DE radiography works well to fulfill this function.

The DE method is not optimal for quantification, but useful for sample characterization into groups. Only the HRXMT scan or some other characterization instruments can accurately describe the detailed mineral information. Nevertheless, the dual energy method is truly helpful for examining the lost minerals in a short time, with mass samplings, rather than doing full HRXMT scans. This reduces the experimental cost and lead time, improves data accuracy, data reliability and improves their performance. In the future, the rapid scan DE method should be able to integrate the rapid radiography scan for a complete examination procedure before the HRXMT scan as a faster and more accurate choice, and it could help to solve problems for difficult-to-float ores.

a) Single

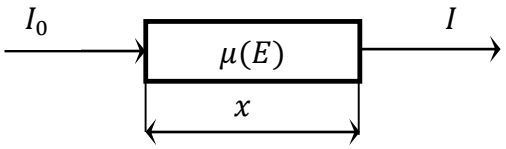

b) Multiple

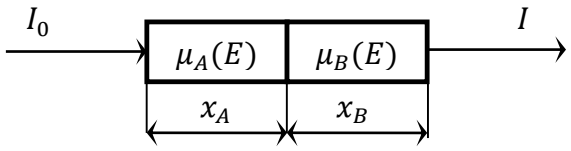

Figure 4.1 A simplified X-ray beam, I_0 attenuated through single (a) or multiple (b) materials, having thicknesses, x_A , x_B results in attenuated beam, I.

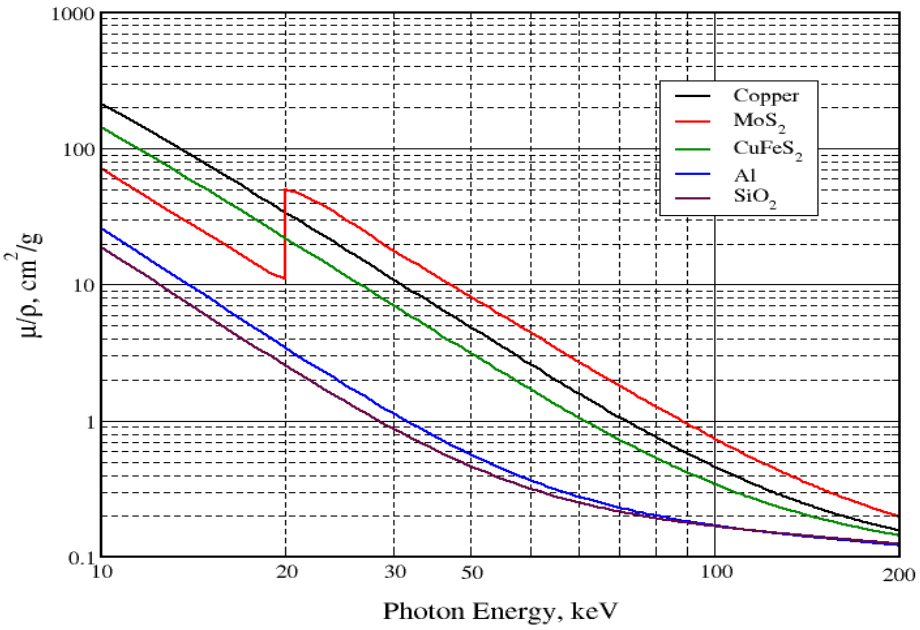

Figure 4.2 Mass attenuation coefficients of Al and Cu representing the gangue mineral (quartz) and high density trace minerals (chalcopyrite and molybdenite) using a software application called XMuDat (Nowotny, 1998).

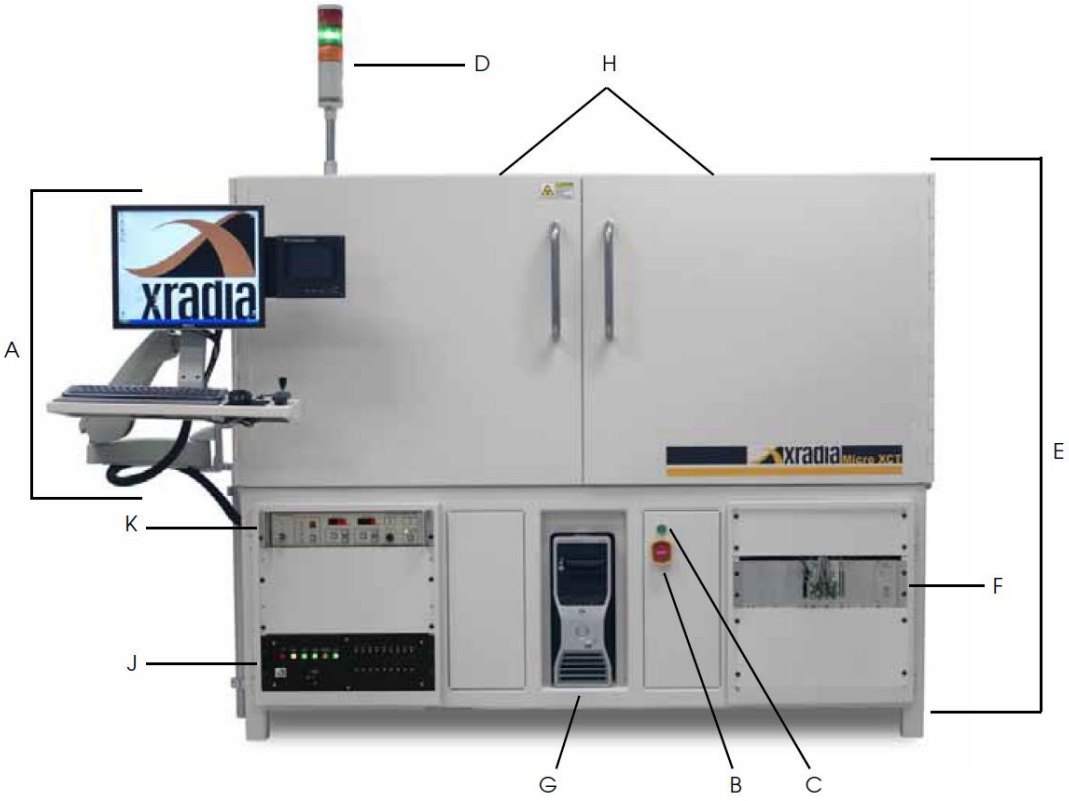

Figure 4.3 The Xradia MicroXCT-400 system at the University of Utah. Major external components: A – Ergonomic station; B – EMO button; C – RESET button; D – light tower; E – enclosure; F - motion controller hardware; G – workstation; H - access door; J – power distribution; K – storage server.

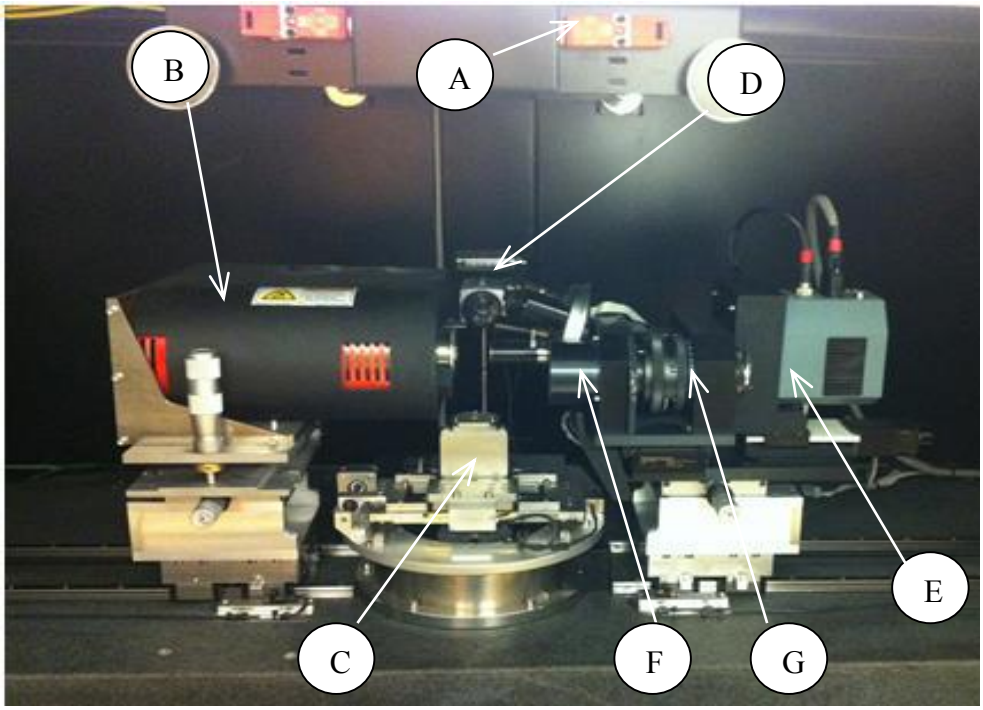

Figure 4.4 Visual internal view of the MicroXCT-400, with the access doors open. (A – Safety lock; B – X-ray source; C – Sample stage; D – visual light camera; E – detector assembly; F – turret; G – macrolenses).

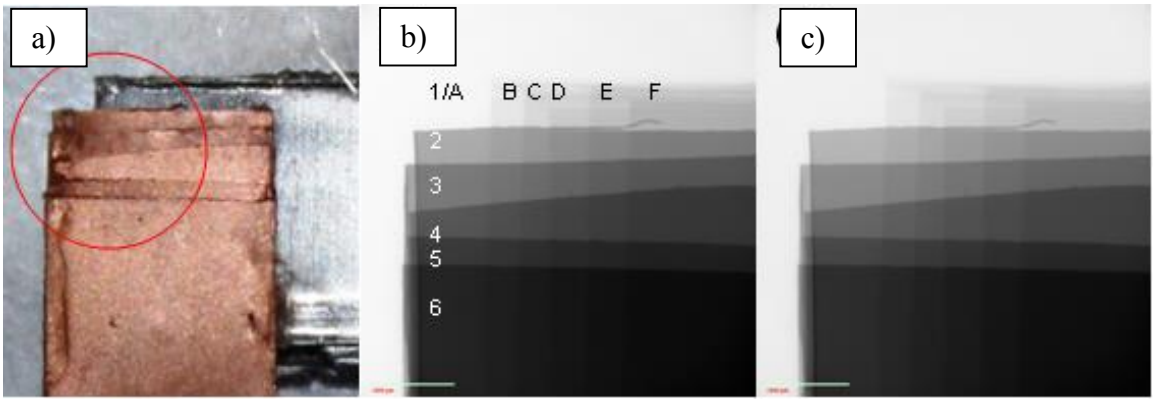

Figure 4.5 Photo of stacked Al and Cu foils (a) and radiographs of the stacked Al and Cu wedges for DE calibration at 80 kV (b) and 140 kV (c).

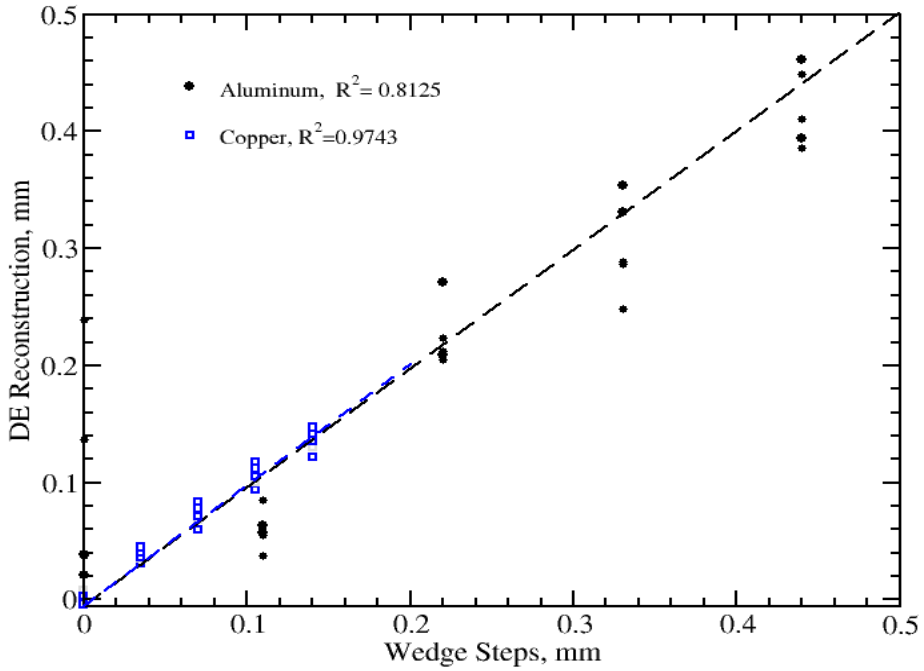

Figure 4.6 Comparison between the measured step-wedge thickness and the reconstructed thickness from DE radiography for the Al foil and Cu foil wedges.

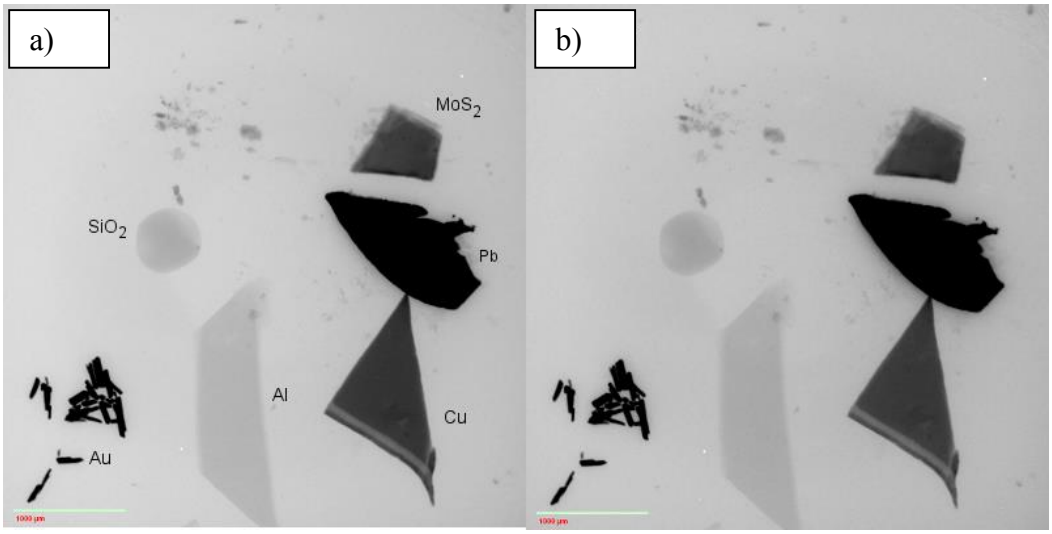

Figure 4.7 DE radiographs (80 kV and 140 kV) of the quartz, aluminum, copper, molybdenite, gold and lead samples for determination of the unknown coefficient and effective atomic numbers. a) Low-energy level; b) high-energy level.

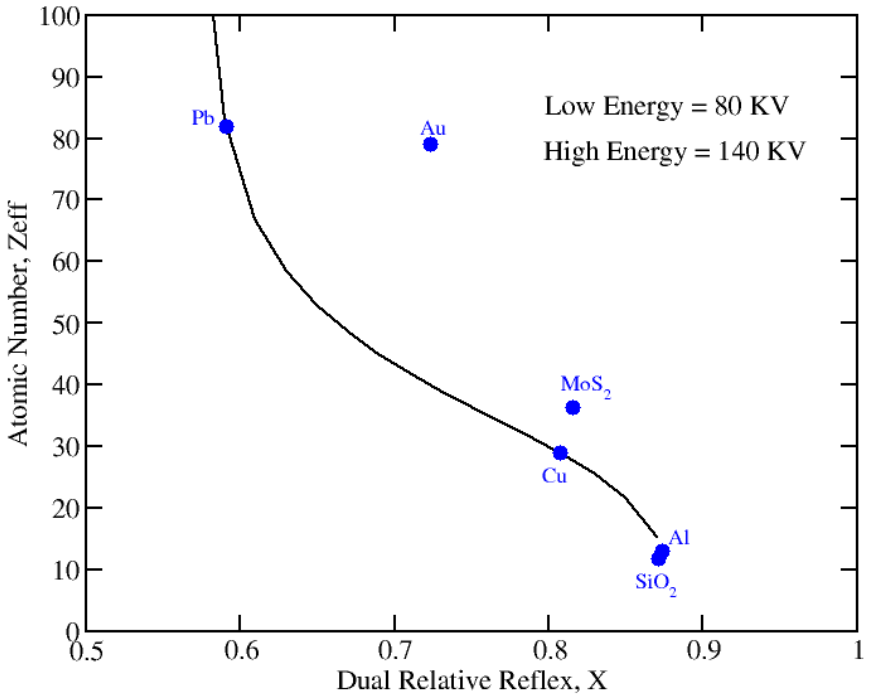

Figure 4.8 Estimated (line) and measured (points) data of effective atomic numbers based on the DE relative reflex of two radiographs, X.

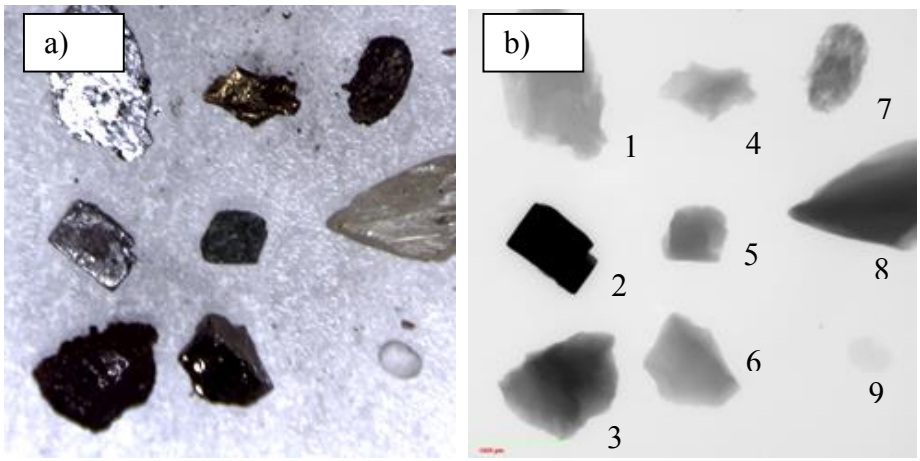

Figure 4.9 Microphotograph (a) and radiographic (b) image of main minerals (the detailed information is in Table 4.5) in Cu-Mo flotation tailings for DE calibration at 80 kV and 140 kV. 1 – molybdenite; 2 – galena; 3 – bornite; 4 – chalcopyrite; 5 – azurite; 6 – pyrite; 7 – hematite; 8 – sphalerite; 9 – quartz.

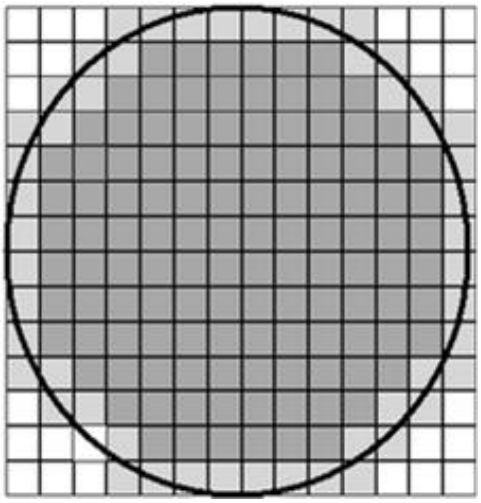

Figure 4.10 Partial volume effect dilutes the X-ray intensity values of a mineral during radiography analysis. In the case of MoS_2, the resulting attenuated value is close to that of copper minerals, making it difficult to distinguish MoS_2 from the other medium density and/or atomic number minerals.

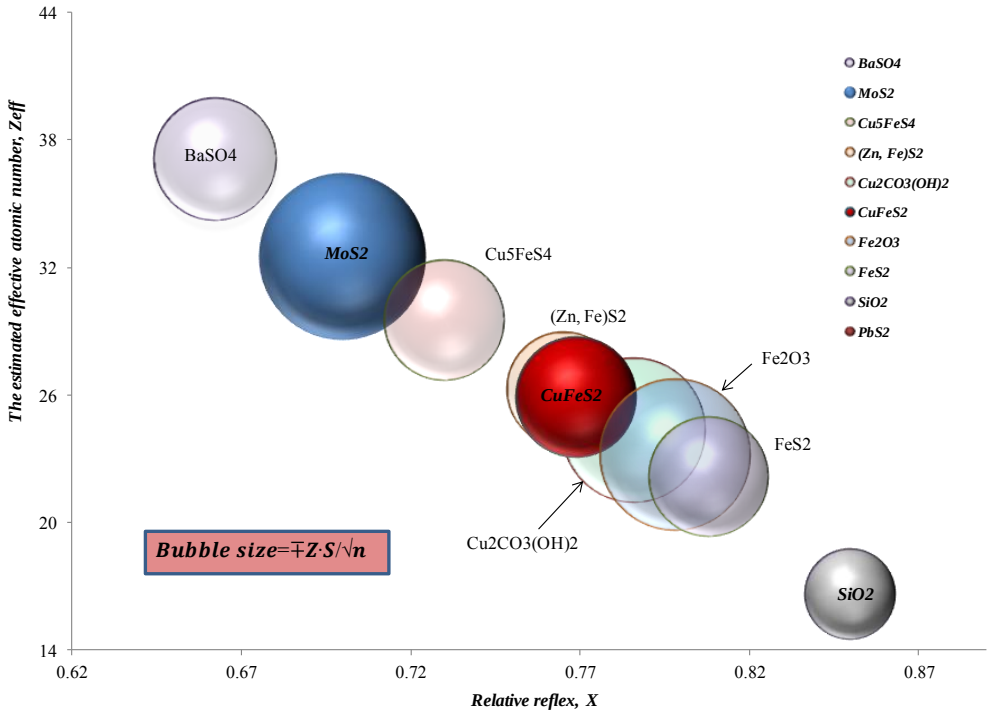

Figure 4.11 Dependence of the effective atomic number upon radiography reflexes in the regions of the photo effect and Compton scattering. The experimental dependence for materials of known composition are indicated.

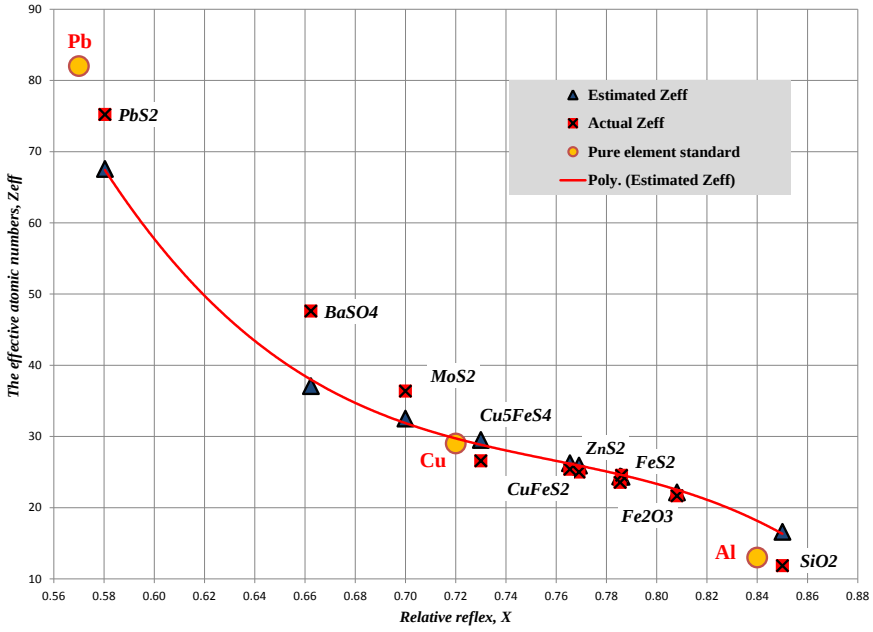

Figure 4.12 Calibration curve for given K_i and p-3.8 values and comparison between estimated (blue) and actual (red) effective atomic numbers from DE radiographs for each mineral.

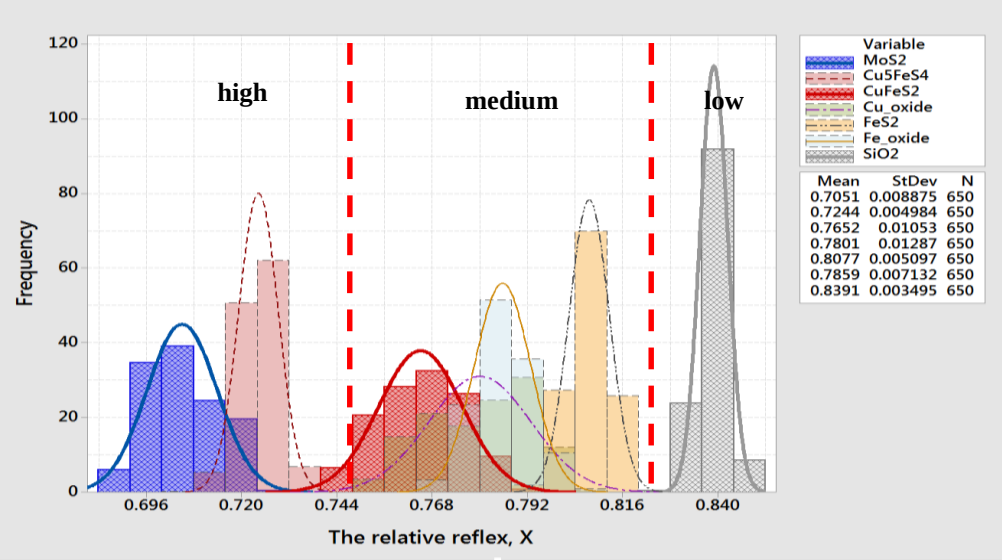

Figure 4.13 Histogram of the relative reflex of the most common sulfide minerals in the KUC flotation tailings.

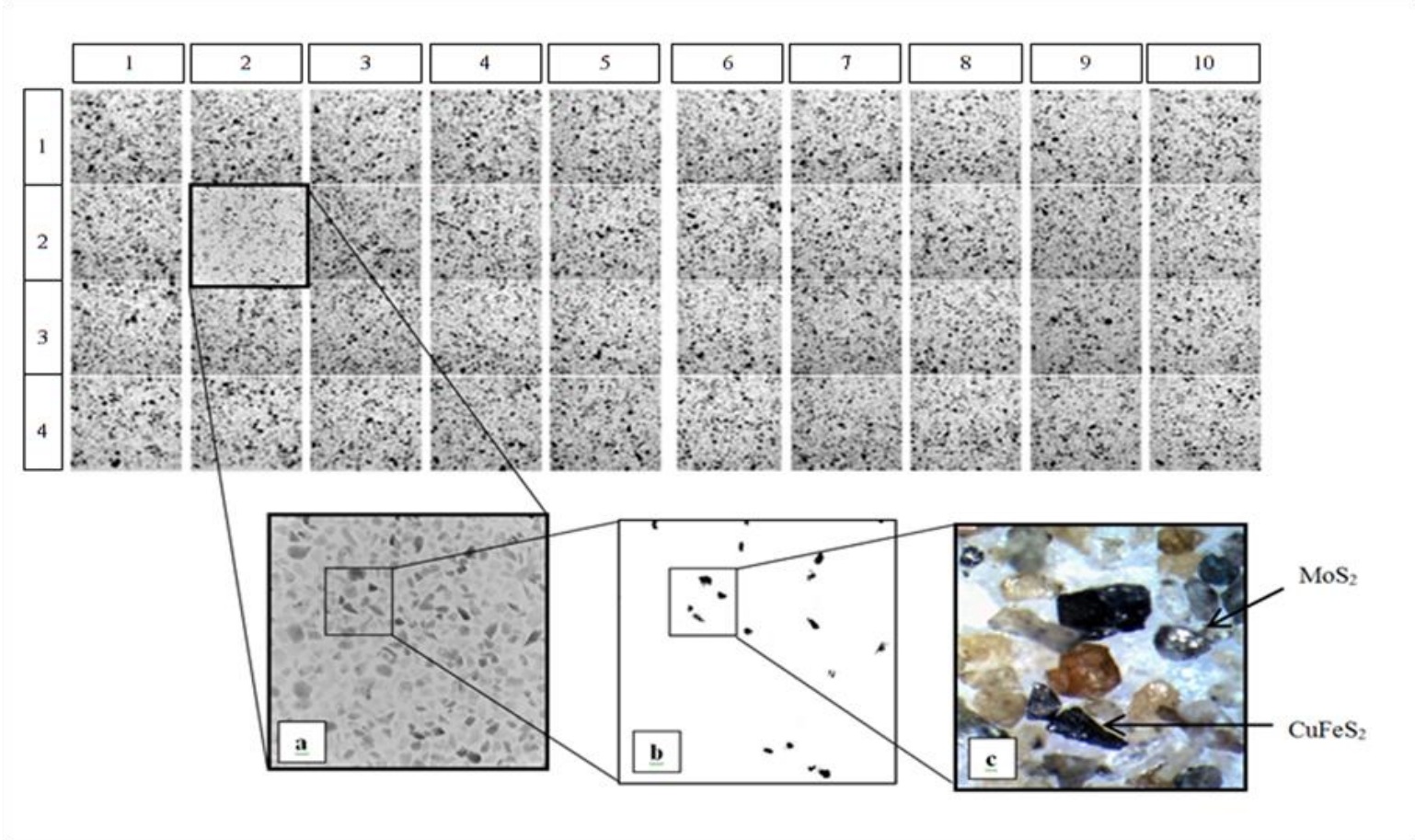

Figure 4.14 Molybdenite and chalcopyrite particles identified for each section of slide based on DE radiography and optical inspection for the search and isolation of trace mineral particles.

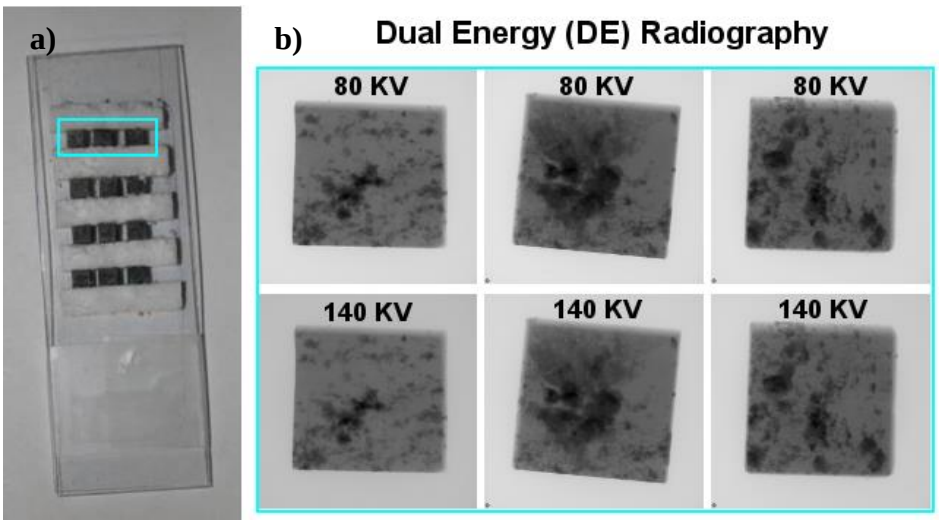

Figure 4.15 Photo of cubic Cu ore particles (a) and the corresponding DE radiographs (b).

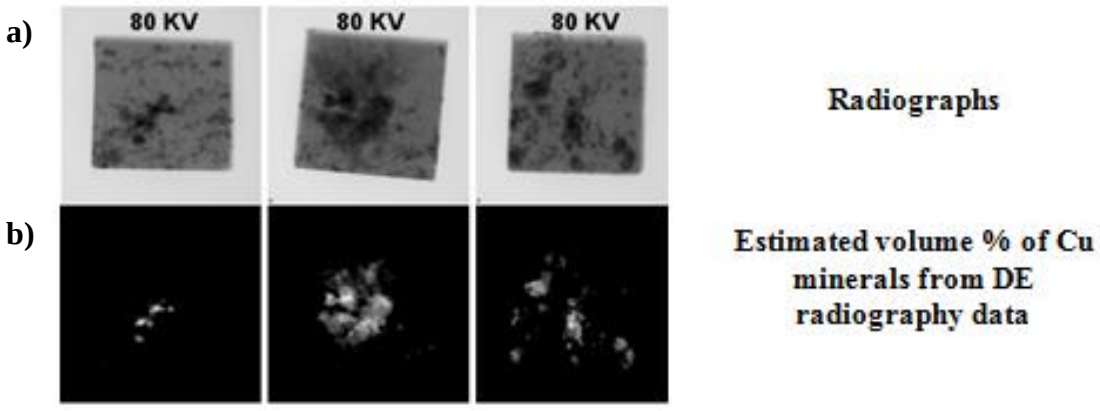

Figure 4.16 Sulfide mineral grains are identified from the estimated Cu minerals using DE radiography. Most of these mineral grains are less than 0.2 mm. a) radiography image; b) tomography image.

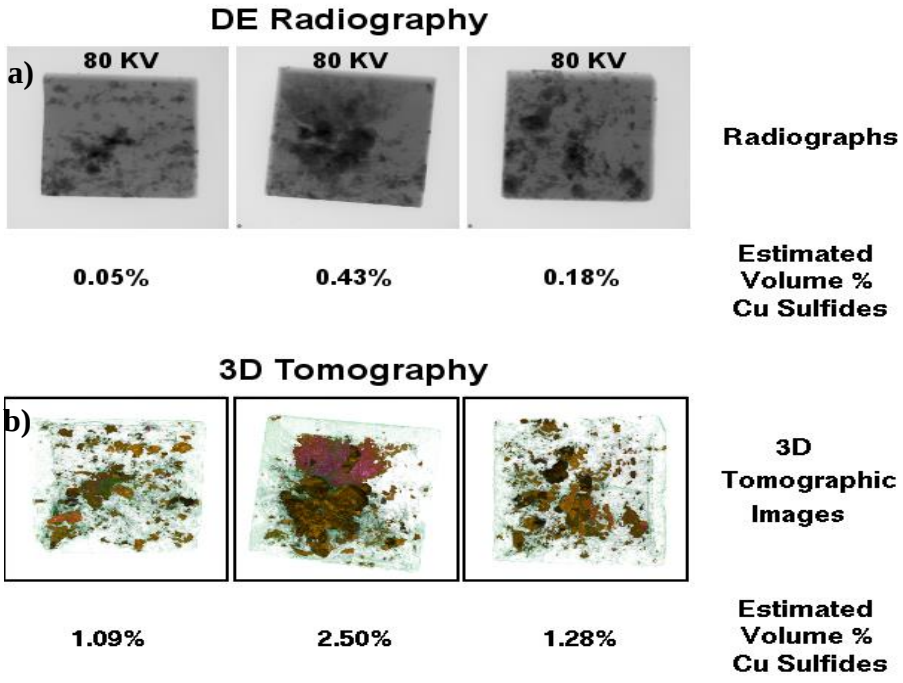

Figure 4.17 Comparison of the cubic Cu ore particles (3x3x3 mm) using DE radiography (a) based on Figure 4.15 and 3D tomography (b) images, respectively.

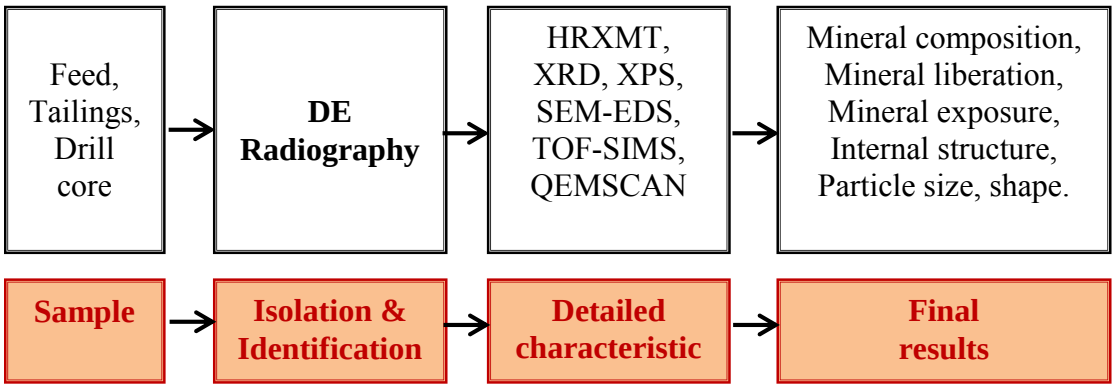

.

Figure 4.18 Combination of DE radiography and detailed characterization analysis for mineral properties.

a) Size class - 150 x 300 µm

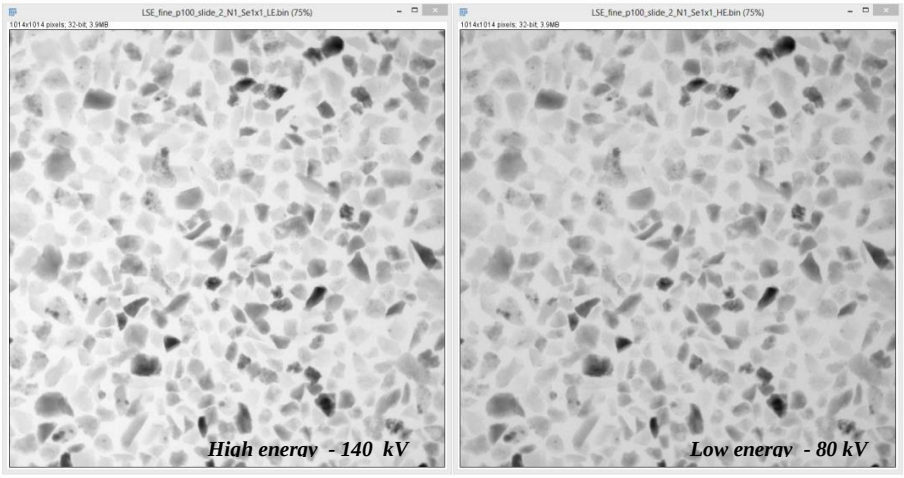

b) Size class - 75 x 150 µm

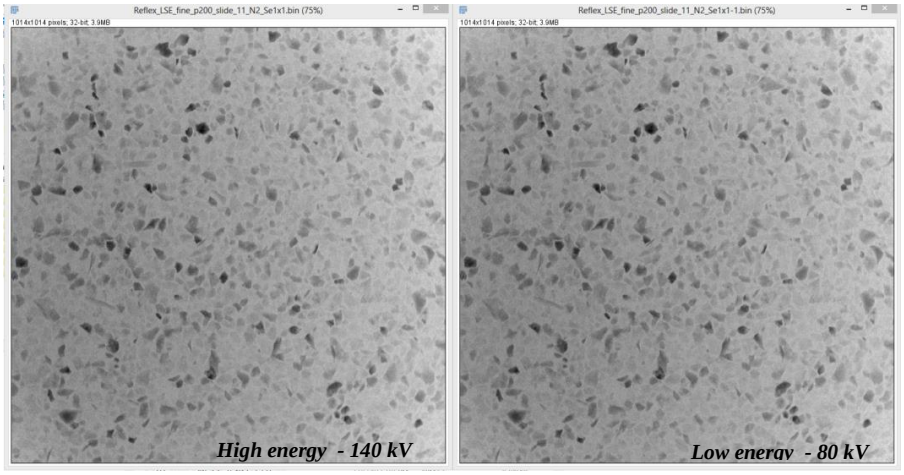

Figure 4.19 DE radiography scans from the LSE rougher tailings (fine grinding – 25 % + 100 mesh size class). a) Coarse size class; b) medium size class. The images on the right are low-energy (80kV), and the images on the left are high-energy (140kV).

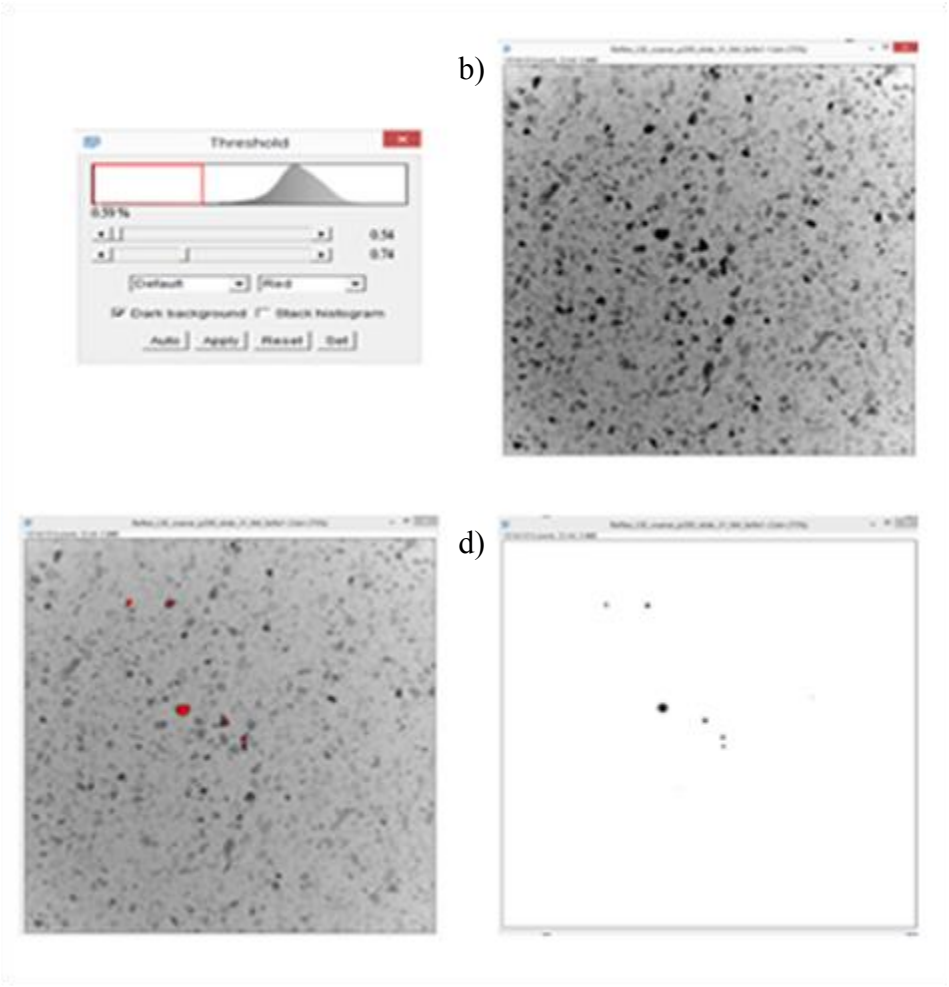

Figure 4.20 ImageJ thresholding function that segments the background and medium/low atomic number minerals from high atomic number minerals. a) Threshold dialog box; b) image of molybdenite particles prior to tresholding; c) threshold adjustment to match particles; d) final binary threshold image showing black particles on white background.

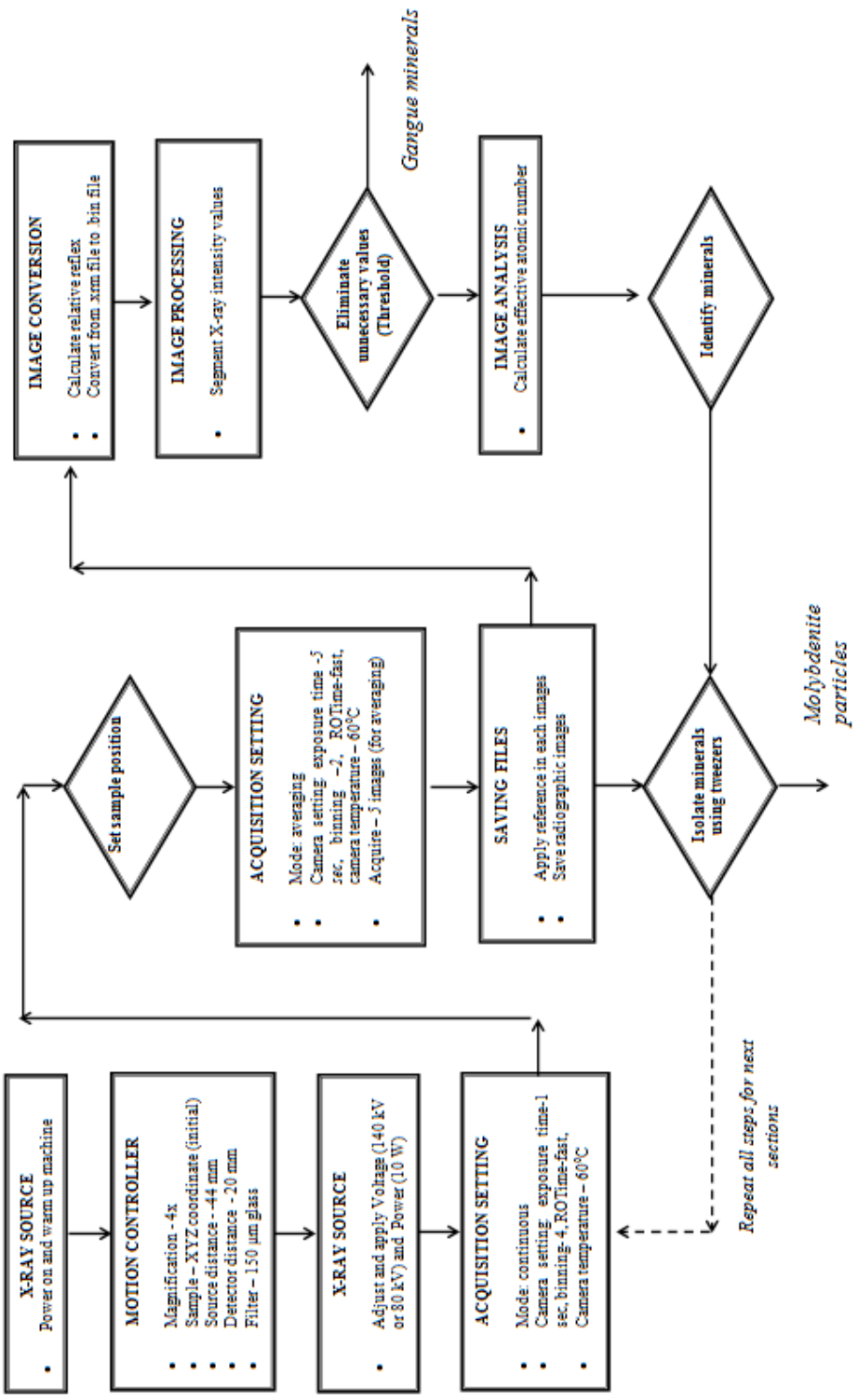

Figure 4.21 Summary of rapid scan dual energy (DE) radiography and its application in the analysis of tailings slides.

Table 4.1 Measurement of log attenuation values from different sections of Al and Cu wedge steps (different thickness and composition) at 80 kV (white column) and 140 kV (gray shaded column).

			A		B		C		D		E		F	
Foil thickness, mm			Aluminum foil											
			0.00		0.11		0.22		0.33		0.44		0.55	
1		0.000	0.0	0.0	2.8	1.6	5.2	3.2	7.5	4.7	9.7	6.1	12.1	7.8
2		0.035	13.2	8.2	15.0	9.5	16.4	10.6	18.0	11.9	19.5	13.1	21.1	14.4
3	Copper	0.070	21.8	14.5	23.2	15.6	24.3	16.6	25.6	17.7	26.8	18.8	28.0	19.8
4	foil	0.105	28.2	19.7	29.4	20.7	30.4	21.7	31.5	22.7	32.5	23.6	33.3	24.4
5		0.140	33.0	24.0	34.2	25.0	35.1	25.9	36.0	26.8	36.8	27.6	37.5	28.4
6		0.175	36.9	27.7	37.9	28.6	38.8	29.4	39.5	30.3	40.3	31.0	40.9	31.8

Table 4.2 Corresponding unknown coefficients used in Equation 16 for thickness estimation of Al and Cu foil wedges.

Reconstruction coefficients for thickness of Al		Reconstruction coefficients for thickness of Cu	
a_0	0.02	c_0	0.00
a_1	-0.84	c_1	28.15
a_2	1.49	c_2	-16.35
a_3	-0.01	c_3	0.18
a_4	0.01	c_4	-1.01
a_5	-0.01	c_5	0.41
b_0	-0.07	d_0	-4.00
b_1	0.04	d_1	-35.45

Table 4.3 Measured and calculated thicknesses of Al and Cu samples for sections A6 and F6.

Sections	Transmission		Thickness, mm		Thickness, mm	
	L, 80 kV	H, 140 kV	Al	Al calc.	Cu	Cu calc.
A6	36.93	27.68	0.00	0.30	0.18	0.15
F6	12.07	7.81	0.55	0.53	0.00	0.01

Table 4.4 Measured log attenuation values and relative reflex, X, acquired from DE radiography used for the determination of effective atomic numbers for various materials.

Material	Chemical formula	Effective atomic number, Zeff	Log attenuation value		Relative reflex, X
			80 kV	140 kV	
Aluminum	Al	13.00	74.62	85.42	0.87
Quartz	SiO_2	11.85	74.11	85.05	0.87
Copper	Cu	29.00	63.00	78.05	0.81
Molybdenite	MoS_2	36.37	63.59	77.94	0.81
Gold	Au	79.00	43.12	59.64	0.72
Lead	Pb	82.00	16.74	28.31	0.59

Table 4.5 Basic properties of most abundant minerals of copper porphyry ore for dual energy radiography calibration.

	Mineral		Effective atomic number, Zeff	Density, g/cm3
	Name	Formula		
1	Molybdenite	MoS_2	36.37	4.62-4.73
2	Galena	PbS_2	75.21	7.31-7.58
3	Bornite	Cu_5FeS_4	26.58	5.06-5.09
4	Chalcopyrite	$CuFeS_2$	25.00	4.10-4.30
5	Azurite	$Cu_3 (CO_3)_2(OH)_2$	24.54	3.77-3.83
6	Pyrite	FeS_2	21.64	4.80-5.10
7	Hematite	Fe_2O_3	22.69	5.10-5.25
8	Sphalerite	$(Zn, Fe)S_2$	25.40	3.90-4.20
9	Quartz	SiO_2	11.85	2.65-2.70

Table 4.6 Numbers of estimated lost chalcopyrite and molybdenite particles in KUC rougher tailings, size classes (300x150; 150x75 μm).

Ore type	Grind condition, % +100 mesh	Size class, micron	Rougher tailings				Estimated numbers* of lost mineral particles in ten sample slides	
			Grade, %		Distribution, %			
			Cu	Mo	Cu	Mo	Cu	Mo
Mz2HE	25	300x150	0.05	0.0035	28.9	16.2	118	8
		150x750	0.01	0.0020	5.2	6.3	32	9
	35	300x150	0.10	0.0046	17.5	9.4	221	10
		150x750	0.05	0.0022	6.8	3.5	112	9
LSE	25	300x150	0.14	0.0026	23.9	19.5	320	6
		150x750	0.07	0.0025	24.6	40.2	154	11
	35	300x150	0.35	0.0043	62.1	31.8	790	10
		150x750	0.12	0.0032	14.8	16.9	260	14
MZ2S	25	300x150	0.16	0.0225	43.4	50.5	361	51
		150x750	0.09	0.0071	21.7	14.8	196	30
	35	300x150	0.25	0.0150	54.9	46.4	556	34
		150x750	0.08	0.0050	19.5	17.8	171	21

* *assuming all lost particles are fully liberated*

Table 4.7 Summary of advantages and disadvantages of DE radiography method.

	Advantages	Disadvantages
Major	Replaces tedious manual analysis by systematic, computer automated analysis	Has difficulty distinguishing minerals with very similar composition
	Reduces the potential for operator bias and human error	Accuracy and precision of results is not high enough
	Increases throughput and the number of mineral grains examined, providing a more statistically representative analysis of a sample	High degree of skill and experience is required for exposure and interpretation
	Has the ability to distinguish fine-grained or complexly intergrown minerals at the scale of micrometer	The equipment is relatively expensive (especially for X-ray sources)
Minor	Can detect both surface and internal structure	Requires monosize distribution
	Significant variation of material can be detected by this method	
	Sample preparation is easy	
	Scanning time is short	

CHAPTER 5

CHARACTERIZATION OF LOST PARTICLES IN FLOTATION TAILINGS USING ADVANCED INSTRUMENTATION

5.1 Introduction

Tailings evaluation can define the actual losses in a mineral processing plant, while simultaneously defining why the losses occur and what might be done to flotation efficiency. Of course, working with tailings is never easy. Minor or trace concentrations of valuable minerals means that sample collection and integrity become a major concern. Trace mineral analysis for minerals such as molybdenite is challenging and often the process of selecting and preparing an appropriate, representative sample is more work than undertaking the characterization analysis. Fast and accurate identification of lost minerals in flotation products, such as feed and tailings, is a very important topic in metallurgical engineering. Most particle identification methods often overlook and miscount the trace mineral concentration in flotation tailings. To correct this, it is proposed that the DE radiography method be used to quantitatively identify and collect trace particles. Combining DE rapid scan radiography with other detailed characterization methods may facilitate an accurate accounting of trace minerals at the parts per million

concentration, as described in Chapter 4. HRXMT, SEM and QEMSCAN can be used for more accurate mineral identification and liberation analysis, once the lost mineral particles are isolated from the tailings.

The objective of this phase of the dissertation research is to characterize the identified and isolated valuable sulfide mineral particles from the rougher tailings and determine their liberation state, association with other minerals and surface chemistry features. To identify, characterize and quantify these lost particles, there are a variety of methods available. The more traditional methods include elemental analysis done by XRF, mineralogical analysis by XRD, mineral phase liberation analysis using automated SEM techniques such as QEMSCAN or MLA, and HRXMT. Surface chemistry features can be determined using XPS and ToF-SIMS.

5.2 Materials and methods

Generally, particulate materials are sampled from input (feed) and output products (rougher concentrate and rougher tailings) of flotation and analyzed to evaluate the efficiency of the separation. Specifically, rougher tailings from fine grinding experiments were considered for detailed characterization analysis. The instruments used in this section are optical microscopy, SEM, X-ray CT and XPS, whose operational details and experimental methodology for characterization analysis are described in following sections. The detailed analysis can be divided into four main categories:

- Initial characterization analysis
- Particle size distribution and size-by-size chemical analysis
- Mineralogical analysis and liberation state analysis using SEM and HRXMT

- Surface characterization analysis such as slime coating and surface oxidation using SEM-EDS and XPS.

A schematic diagram of the procedure adopted to isolate and collect lost sulfide mineral particles and the detailed characterization analysis is presented in Figure 5.1. In the following Sections, 5.2.1, 5.2.2, and 5.2.3, instruments and methodology are described.

5.2.1 Particle size distribution and size-by-size analysis

The purpose of size-by-size distribution analysis is to determine the Cu and Mo distribution in the flotation products. After rougher flotation, representative portions (approximately 150 grams) of samples of the flotation feed and tailings were split and then screened into 5 size fractions by wet or dry screening using analytical screens with quadratic openings. Five size classes were used to represent very coarse (>300 μm), coarse (300x150 μm), medium (150x75 μm), fine (75x37 μm) and slime (<37 μm) size fractions.

Initially, all samples were deslimed by wet screening at 400 mesh (37 μm). The coarse fraction above 37 μm was dried, weighed and screened using standard sieves; 48, 100, 150, and 200 mesh and the certain amounts of samples were prepared for chemical analysis. Each size fraction was assayed to determine copper, molybdenum and iron content. Then, all molybdenite particles in each size class were collected and isolated using the DE radiography method. The principle and experimental procedures of DE radiography are well described in Chapter 4.

5.2.2 Liberation analysis using HRXMT

The micro tomography technique offers a unique capability for the quantitative analysis of multiphase systems through the acquisition of high-resolution 3D images. One important area of application for HRXMT is mineral liberation and mineral exposure analysis (Miller and Lin, 1987; Gu and Napier-Munn, 1997; Lin and Miller, 2001; Videla et al, 2007; Al-Wakeel et al, 2009). The X-ray micro tomography technique is able to distinguish different mineral phases contained in ore particles based on the corresponding computed tomography (CT) numbers for each phase. Lin and Miller (1996) described the CT numbers for several of the most abundant copper minerals in copper porphyry ores and the results are presented in Figure 5.2.

As a result of DE radiography inspection, lost sulfide particles were isolated from rougher tailings samples and then all collected particles were poured into a plastic cylinder of up to 4 mm in diameter. The sized samples do not require any other special preparation. However, the sample needs to be well confined and held by frictional forces because any small movement will cause reconstruction failure and error.

The sample was placed on the rotating stage between the X-ray source and the detector, where photons pass through the sample and the projected image is captured by the detector. Usually, a full tomographic 3D scan on the MicroXCT-400 requires 1000 projections and then the data are used to reconstruct the experimental data for liberation analysis.

During tomography data acquisition, the scan conditions are an important issue in order to obtain the best image quality. Image quality depends on many factors such as source voltage, magnifications, distance between source and detector, physical filters,

field of view, exposure time, projection count and reference states (Xradia, 2010; Hsieh, 2012). As described by Lin and Miller (1996), an appropriate scan condition for image acquisition of copper samples is presented in Table 5.1.

As mentioned before, the Xradia MicroXCT-400 provides an application called XMController and XMReconstructor (Xradia, 2010) for image acquisition and reconstruction. According to the specifications of the MicroXCT-400, the maximum color depth of the CCD detector is a 16-bit grayscale, which means the CT reading is between 0 and 65535 for each voxel. Initially, the results of an HRXMT scan were saved in a grayscale, unsigned 16-bit tomography file using XMReconstructor. Then, the tomography file was converted from a 16-bit unsigned short to an 8-bit unsigned byte using MIPAV (McAuliffe, 2012). CT readings higher than molybdenite values can easily be excluded by MIPAV software while file conversion is being completed. After the reconstruction, the reconstructed images were rescaled by the CT standard (Lin and Miller, 1996; Hsieh, 2012). The scale is usually a range from 0 to 255 in a specific ratio focused on the range of objective mineral attenuation coefficients. The conversion ratio between the 16-bit unsigned short and 8-bit unsigned byte was 40 and the unsigned byte file size (1 gigabyte) reduces to one-half of the unsigned short file size (2 gigabytes) for data storage when the file conversion is completed. The conversion is favored to save storage space and also to use low-end computers to process the image file under the system limitations. Table 5.2 shows a comparison of CT numbers with corresponding minerals for mineral characterization and quantification at the same voxel in unsigned short and unsigned byte.

Based on rescaled CT numbers, the selected minerals such as molybdenite and

chalcopyrite are easily distinguished from gangue minerals and the reconstructed image can be visualized using volume rendering and image analysis software such as ImageJ (Rasband, 1997), and Drishti (Limaye, 2006) for visualizing tomography data in 3D.

In this work, the 3D object counter plug-in from the ImageJ software was used to describe the liberation state of the lost molybdenite particles based on the HRXMT data and then each corresponding data set was converted to 3D volume rendered images by visual inspection.

5.2.3 Surface characterization analysis using SEM-EDS and XPS

A Hitachi 6000 scanning electron microscope with an attached EDS system was used in order to characterize the samples of feed, concentrate and tails from rougher flotation, and with respect to slime coating, chemical composition, and oxidation state of elements at the molybdenite and chalcopyrite surfaces. SEM is a type of electron microscope that produces images of a sample by scanning it with a focused beam of electrons. The main advantages of SEM over optical microscopy include much higher magnification (>100,000X) and greater depth of field, up to 100 times that of optical microscopy. With SEM microanalysis, it is possible to identify chemical elements or compounds present either within or on the surface of an object. Identification of the elements present may be qualitative or quantitative. Qualitative microanalysis means that the elements present in the sample are identified from their characteristic X-ray peaks, but their abundances are not determined. The analytical spot size ranges from about 100 μm to 100 nm in this analysis. For qualitative microanalysis of an unknown object, consideration must be given to the operating parameters of the microscope and the properties of the sample to

be analyzed. SEM can also provide information about crystal defects and chemical bonding of mineral surface.

In addition to SEM, more detailed characterization has been accomplished and confirmed using X-ray photoelectron spectroscopy (XPS). XPS is particularly useful in the determination of surface elemental composition, site occupancy, oxidation and reduction chemistry, adsorption of cations and anions, and differentiation of exchangeable and nonexchangeable clay components. The principles of XPS are well documented in the literature (Wagner et al, 1979; Briggs and Seah, 1990; Yates, 1998).

From these parallel analyses, it has been possible to identify the contributing mineralogical and surface chemical factors resulting in the observed flotation behavior of the refractory copper porphyry ores.

5.3 Results and discussions

5.3.1 Initial characterization analysis

Using the optical microscope and SEM at the University of Utah, a preliminary mineralogical analysis was carried out on the raw sample without DE inspection to obtain more conventional images of the minerals present and also to understand the flotation response achieved with KUC ore types. SEM-EDS can qualitatively identify and map the distribution of the mineral phases within the samples.

Samples were prepared by mounting on pin type SEM stubs using carbon adhesive tabs. Samples were examined in a Hitachi 6000 SEM using a beam voltage of 20 kV and in the secondary emission and back scattered modes. For conventional imaging in the SEM, specimens must be electrically conductive, at least at the surface, and electrically

grounded to prevent the accumulation of electrostatic charge at the surface. Samples are usually coated with an ultrathin coating of electrically conducting material such as gold and carbon. Polished sections of the rougher concentrate and rougher tailings for each ore type were prepared without DE radiography pretreatment. Each polished section was studied with a mean of 50 – 100 fields analyzing 10000 -15000 particle sections.

The average analyzing time for each polished section was approximately 2 hours. SEM photomicrographs of sized particles from the MZ2HE ore, rougher concentrate, are presented in Figure 5.3. The main sulfide minerals in the rougher concentrate were chalcopyrite, pyrite and molybdenite. All particles appeared to be well liberated. It was also observed that the MZ2HE rougher concentrate had sulfide minerals similar to those found in the LSE and MZ2S rougher concentrates. Apart from the main mineral phases, associations of these individual mineral phases with other minerals were observed. Chalcopyrite and pyrite were observed mostly in association with gangue minerals. Some minor bornite and covellite particles were also found in the samples. In the polished specimen prepared from rougher tailings, the main minerals were chalcopyrite, pyrite and the gangues. Some minor bornite and molybdenite particles were also found in the sample. The photomicrographs for these 150x75 μm size, locked chalcopyrite particles in the rougher tailings are presented in Figure 5.4. As emphasized in Figure 5.4, most chalcopyrite was interlocked with gangue minerals or locked inside pyrite in the rougher tailings. In general, a considerable amount of locked chalcopyrite was observed in the MZ2HE rougher tailings. It was difficult to determine the extent of liberation and the liberation characteristics of chalcopyrite based on 2D analysis. According to visual inspection, the presence and nature of the liberation state for chalcopyrite in the rougher

tailings was quite similar to that observed for other samples of KUC ores. It appeared that chalcopyrite losses are most likely to be in the locked and middling particles than is the case for molybdenite. The loss of these locked chalcopyrite particles in the tailings significantly lowers Cu recovery. In the rougher tailings, the Mo particles are mostly considered to be fully liberated in all ore types, as shown in Figure 5.5. In this optical microscopy study, only two molybdenite particles were detected in all samples due to its low concentration. Except for particle morphology and size, it is difficult to conclude anything about these molybdenite particles.

As widely known, molybdenite may be the most readily floatable of all sulfide minerals, however, enrichment by flotation is not always simple. Particularly, if Mo particles are big, and flat, they generally became more difficult to float. A number of chemical mechanisms including oxidation of minerals and media, oxygen reduction and galvanic coupling could occur and govern the surface properties of molybdenite minerals at the Copperton concentrator. The initial characterization analysis confirmed that the recovery of Cu sulfide is more dependent on the liberation state of chalcopyrite, while for molybdenite some other factors appear to play a significant role. As mentioned before, lack of hydrophobicity may be related to mineral slimes adsorbing onto the surface, surface oxidation, and/or scale precipitation from process water. In this regard, SEM 2D analysis is not convenient to characterize trace minerals at concentrations of ppm. The rarity of molybdenite in the samples results in limited accuracy, thus further analysis of particles is required for increased accuracy.

As a final point, it was concluded that any kind of 2D characterization analysis really could not provide enough information about the lost molybdenite particles.

5.3.2 Results of size-by-size recovery analysis

5.3.2.1 MZ2HE ore

Based on metallurgical analysis of a rougher flotation test (T5a), approximately 92.5 % of the Cu and 85.8 % of the Mo were recovered in the rougher concentrate after fine grinding. Results of the particle size distribution and size-by-size chemical analysis of these rougher tailings are shown in Table 5.3 and Table 5.4. As indicated in Table 5.3, experimental results show that about 4.8 % of Cu in the feed material was in the slime fraction (<37 μm) and about 12 % of the total Cu was coarser than 150 μm. The fraction between 300 and 37 μm included the remaining Cu. A maximum Cu content (0.98 %) was observed in the feed for the 75x37 μm size class, which is the most favorable size class for flotation separation. The grind size (p80) was approximately 132 μm after fine grinding.

First, the fine fraction below 37 μm was considered in the MZ2HE rougher tailings sample. The amount of slimes in the rougher tailings was 19.6 % after fine grinding, containing 19.6 % of the Cu and 8.3 % of the Mo for the MZ2HE ore. This indicated that the slime size fraction in the rougher tailings did not contain too many valuable minerals. However, Cu recovery dropped off in the coarse (150x75 μm) size fraction. Approximately 61.0 % of Cu was distributed in the coarse size class above 150 μm.

With Mo, fine grinding indicated Mo loss in the rougher tailings in the coarse size fractions above 75 μm. In particular, in the 300x150 μm and 150x75 μm size classes, there was a significant loss in Mo distribution. The recovery of Mo in these size classes dropped off to a much greater extent than the recovery of Cu. It is expected that Mo particles could definitely be liberated but their flotation efficiency was unsatisfactory and

unpredictable. According to Cu and Mo distribution in the rougher tailings and feed, the relative recoveries of each size fraction could be evaluated based on chemical analysis. An analysis of the relative recovery by size class was carried out to investigate Cu and Mo loss for different particle size classes as they often exhibit different recovery rates. The losses of Cu and Mo in the MZ2HE rougher flotation feed and tailings depend on size classes and is illustrated in Figure 5.6. The feed and flotation products were characterized with respect to mass distribution, as well as chemical and mineralogical characteristics in order to evaluate the flotation behavior of each size class.

Hence, a better understanding of the flotation of coarse (300x150 µm) and medium (150x75 µm) size fractions, instead of the slime fraction, is required for the MZ2HE ore. A detailed investigation is clearly warranted in the liberation analysis.

5.3.2.2 LSE ore

A rougher flotation test (T1a) of the LSE ore showed that 10.9 % of Cu and 16.8 % of Mo were lost in the rougher tailings, as shown in Figure 5.7. Flotation feed data indicated that about 11.7 % of Cu was in the form of fines below 37 µm and approximately 1.1 % of the total Cu is coarser than 300 µm, as shown in Table 5.5. The fraction between 300 and 37 µm included the remaining 87.2 % of Cu, which is really favorable for flotation separation. A maximum Cu content (1.1%) was observed in the feed for the 75x37 µm size class. The size-by-size chemical assays for the LSE rougher feed and tailings samples are presented in Table 5.5 and Table 5.6, respectively.

As seen from Table 5.6, the amount of slimes was 26.9%, containing 33.9 % of the Cu and 35.8 % of the Mo. It means that the LSE sample contained significant clay

minerals. The presence of clay in porphyry ore could cause a loss in recovery possibly due to the presence of slime coatings on mineral surfaces or on air bubbles.

As mentioned previously, Bradshaw et al. (2011) described that clay minerals such as talc, kaolinite, bentonite and smectite, which are often associated with copper, gold and other valuable minerals, increase reagent consumption and create serious frothing or non-frothing problems. In particular, the Mo recovery significantly dropped in the tailings in the coarse size classes above 150 µm (approximately 43.3 %) and in the fines below the 37 µm size classes in the LSE ore. Hence, a better understanding of the flotation of coarse molybdenite particles is more important than for the small molybdenite particles in the LSE sample.

5.3.2.3 MZ2S ore

A rougher flotation test (T3a) of the MZ2S ore showed that 9.7 % Cu and 29.9 % Mo were lost in the rougher tailings. The particle size distribution and size-by-size chemical analysis for the MZ2S rougher feed and tailings sample are presented in Table 5.7 and Table 5.8, respectively. The grind size of p80 was 145 µm. However, the amount of slime was quite high as with the LSE ore and 25.5 % of the slime fraction contained 34.5 % of the Cu and 22.3 % of the Mo in the rougher tailings. Cu size-by-size analysis in the rougher tailings showed a trend similar to the LSE ore but the main difference was found in the fine (75x37 µm) size class. Predominately, this size class (75x37 µm) is the most favorable size class for flotation separation but the Cu loss (55.2 %) was significantly higher compared to the LSE ore in the medium (150x75 µm) and fine (75x37 µm) size classes. The Mo recovery significantly drops in the coarse size class above 150 µm and in

the fines below the 37 μm size fractions, as shown in Figure 5.8.

This could be explained by some chemical reactions, such as surface oxidation, which can strongly affect both Cu and Mo flotation performance. It is well accepted that not all particles of a particular size float at the same rate. Flotation separation is based on the fact that different mineralogical species exhibit different degrees of hydrophobicity in the chemical environments employed in flotation circuits. It is expected that particles of different mineralogical or surface composition within a single particle size class would exhibit different rates during flotation. This effect is also observed within the MZ2S rougher flotation data set.

From Figure 5.8, it was evident that Cu and Mo recoveries were adequate in the 75x37 μm size range and as shown in Figures 5.6 and 5.7. However, both Cu and Mo in the coarse fractions +75 μm and +150 μm still recover at a far lower rate in all these ore types due to the particle size. Based on a literature survey, it was well documented that flotation recovery exhibits a classical relationship with particle size (Imaizumi and Inoue, 1963; Trahar and Warren, 1976): poor recovery of the fine and coarse particles and high recovery of the intermediate size fractions. According to size-by-size recovery analysis of the MZ2HE, LSE and MZ2S ore types, it was confirmed that the major amount of Cu and Mo loss are mainly distributed in the fines (-37 μm) and above the coarse (150x75 μm) size fractions. In this research, particles finer than 37 μm in the slime fraction were not analyzed for the detailed characterization analysis for two reasons. First, any particles below 37 μm were expected to be completely liberated and their inclusion could be misleading. Second, most characterization instruments are not designed for low concentration samples with ppm levels and these particles would also be impossible to

isolate individually because the particle size is extremely small for DE radiography pretreatment. In general, when particle size is reduced, the surface area are will be increased and this affects many flotation behaviors. Increased particle charge due to small sizes leads to cohesion, agglomeration, and segregation. Otherwise, in his research, Zhou (2010) broadly described the main reasons for loss of fine molybdenite particles. That is why this research was more focused on coarse and very coarse size fractions, because variation in Mo recovery is driven to a greater extent by coarse particle recovery than fines, with molybdenite being affected more so than copper (Triffet and Bradshaw, 2008).

5.3.3 Mineral liberation analysis using HRXMT

After completing data acquisition and the file conversion, the 3D object counter plug-in on the ImageJ was used to determine liberation characteristics of the molybdenite particles. This plug-in can count the number of 3D objects in a stack and displays the volume, the center and the coordinates for each object. In this case, thresholding has been used in the tomography image in order to separate molybdenite particles from other minerals. The thresholding values for molybdenite were selected from histograms of the CT data for individual minerals, as presented in Figure 5.2. All pixels with intensity above the threshold value were considered as molybdenite pixels while other pixels were considered as being part of the background. The results are presented both as a data table and as a new image file that shows the outlines and numbers of the particles included in measurements after completing the 3D object counter analysis. The data table generated by ImageJ contains a mean volume of the objects, standard deviation, center of objects,

and numbers of object's voxels, as shown in Figure 5.9. The table can then be saved as an .xls or .dat extension, which then could be imported into spreadsheet software such as Excel. The volume of the threshold particle (molybdenite) were associated with gangue minerals or touching other particles can be compared to the average volume of all particles in the sample. Without thresholding, this plug-in could also estimate the average volume of particles in a sample population. Consequently, where the ratio of the volume of molybdenite particle to the average volume of the sample is high or close to 1, this represents a completely liberated mineral grain.

As mentioned before in Section 5.3.1, the liberation analysis by HRXMT scans was only focused on the rougher tailings for each ore type, which was generated from fine grinding at 25 % + 100 mesh size class. In general, the liberation analysis indicates that 90 % of the constituent (gangue) particles are liberated, and 90 - 95 % of the molybdenite particles appear to be present as free, fully liberated particles in most of the ore types. Molybdenite was primarily distributed in the gangue minerals. Table 5.9 presents the qualitative summary results of the liberation characteristics of molybdenite in the rougher tailings of the MZ2HE, LSE and MZ2S ore types. Visual inspection using optical microscopy and SEM revealed good liberation of molybdenite particles in the LSE and MZ2S rougher tailing in the coarse (300x150 μm) to medium (150x75 μm) size fraction, through some interlocked particles in the coarse size class were occasionally observed. These results were confirmed by 3D object counter analysis and the amounts of locked molybdenite particles were more accurately estimated. The minor amounts of unliberated molybdenite particles were presented as locked inside of gangue minerals (particles of grade 0 – 30 %) and/or also by remnants (exposed grain) on the surface of quartz

particles (particles of grade 30 – 60 %). As illustrated in Figure 5.10, the majority of the molybdenite particles (approximately 95 %) were very well liberated in the 150x75 μm size fraction but did show mineral locking with other minerals. Basically, most molybdenite particles contain very fine quartz grains as inclusions and only 1 - 3 % of them are considered locked and in low grade middling particles. The liberation results show that the molybdenite in the 150x75 μm size fraction had significantly better liberation than the 300x150 μm fraction. The real interlocking or high grade middling (particles of grade 50 – 75 %) was primarily observed in the coarse (300x150 μm) size fraction, as illustrated in Figure 5.10 (b). It could be concluded that approximately 30 % of the total Mo loss is related to a liberation issue in both the MZ2HE and MZ2S ore types. Especially, in case of the MZ2HE ore, about 12.7 % of the molybdenite particles interlocked with gangue particles. The 3D volume rendered image might be the best way to identify detailed liberation characteristics (for example, the locked or exposed) of each size fraction based on the same tomography data. As described by Miller and Lin (1996), the classification of mineral phases is based on X-ray linear attenuation coefficients. Most direct volume renderings use 1D dimensional transfer function, which assign color and opacity to the volume based solely on the single quantity that contains the dataset. 2D transfer functions briefly described in the literature (Kniss, Kindlmann and Hansen, 2001) are a most effective way to extract minerals and their boundaries for the classification and analysis of multiphase particles. The 2D transfer function of digital data allows for a clear separation between high, medium and low density and/or atomic numbers minerals of the rougher tailings due to the distinct difference in attenuation coefficients. Particularly, the molybdenite particles were clearly observed in the

reconstructed 3D images obtained through the HRXMT. The difference between molybdenite and chalcopyrite in a specific range of CT numbers gave a good contrast to low attenuation coefficient materials such as silicates, the most abundant minerals in this sample. Figure 5.11 (a) and Figure 5.11 (b) show the original and color segmented 3D views of the rougher tailings sample, respectively.

As shown in Figure 5.11, silicates are visualized as light green particles, and chalcopyrite (orange) is the dominant copper mineral in this sample. Note that only six molybdenite particles (blue) were identified in this color segmented tomography image. In addition, other mineral phases such as bornite and pyrite can also be identified.

As shown in Figure 5.12, the morphology and liberation characteristics of each molybdenite particle in the section taken out from the 3D reconstructed image were clearly presented. Comparing results of the liberation state between 3D object counter analysis and the visual inspection of the reconstructed 3D image, it was concluded that the liberation state was not a main issue for molybdenite loss in the samples of the MZ2S and LSE rougher tailings.

In the size range 150x75 μm, the majority of the molybdenite particles were nearly fully liberated, though with a few particles that are partially locked, making about 90 % liberation. For the size classes 300x150 μm, all the molybdenite particles looked almost the same size with similar shapes, smooth surfaces and fully liberated in the 3D rendered image.

5.3.4 Slime coating analysis using SEM-EDS

After HRXMT analysis, 5 – 8 molybdenite particles were randomly selected from the particles isolated by DE radiography for SEM-EDS and XPS surface analysis. The correct sample preparation is vital to getting good quality information from the sample. First, the effect of coating on the mineral surface was considered, as shown in Figure 5.13. For this research, it was important to leave the sample uncoated (in its natural state), because the surface properties analysis, for determination of the oxidation state and elemental composition around the selected area of the lost minerals, was required after SEM analysis. Generally, the practice of coating samples with metals such as carbon and gold obscures the surface property of the minerals. As observed from Figure 5.13, there was no significant difference between the EDS spectra of the coated and the uncoated particles. Hence, the surface coating was only used for SEM imaging for molybdenite particles in order to improve the SEM image quality and prevent unusual effects such as abnormal contrast and image deformation and shift. Sometimes an unexpected discharge of electrons from a charged area may cause a bright flash on the screen, as shown in the top image of Figure 5.13 (a).

Figure 5.14 (a) and Figure 5.14 (b) show a comparison between molybdenite particles isolated from the LSE rougher concentrate and from the rougher tailings. In general, the molybdenite particles appear to be well liberated, but slime attachments are observed at their surfaces. The slime particles vary in size from 5 - 25 μm. The EDS analysis was primarily focused on two spots on these molybdenite surfaces and the results are presented in Figure 5.14 (Spot # 1) and (Spot # 2). According to the EDS analysis in Figure 5.14 (Spot # 1), Mo and S signals occupied the molybdenite face surface along

with traces of other elements such as O, Si, Fe and Al, as indicated by the EDS pattern.

However, a significant amount of gangue minerals with finer particle size, containing Si, Ca, Al, Mg, K, and O was observed at Spot # 2 in Figure 5.14. A magnified SEM image of a selected area (Spot # 2) on the Mo particle isolated from LSE rougher tailings showing this distribution of elements on the sample surface is presented in Figure 5.15. The Mo loss problem could be solved by knowing the distribution of a particular element without requiring quantitative point analysis. The X-ray mapping clearly shows the extent of molybdenite surface associations with the surface of some gangue particles.

First, as seen in Figure 5.15, it can be concluded that molybdenite particles could easily transfer into the rougher tailings if the slime particles cover more than 15 % of their surfaces. Second, the face plane of molybdenite particles in the LSE rougher tailings is not perfect. There are some microdefects, small step-like edges, formed due to comminution processes such as crushing, grinding and/ or oxidation. These edges on the face planes could act in the same way as fringe edges, attracting significant amounts of fine gangue minerals. In addition, the EDS spectrum for Spot #2 in Figure 5.15 emphasized that Si, O, Mg and Fe are the major contaminants composing the aggregated particles, suggesting that they could be one of the silicate group minerals such as talc and quartz, the major gangue minerals in the skarn type ore. These surface attached gangue minerals or precipitates that obscure the molybdenite surfaces could be the main reason of molybdenite loss from the LSE ore. These observations are in conceptual agreement with the flotation results mentioned previously in Chapter 3. Then, SEM-EDS analysis was conducted for molybdenite particles isolated from the MZ2S rougher concentrate and rougher tailings, and the corresponding results are presented in Figure 5.16 (a) and Figure

5.16 (b), respectively. It is evident that molybdenite particles are liberated, well rounded, with a relatively clean surface when compared to particles from the LSE sample. The major differences of the MZ2S molybdenite surfaces in the rougher tailings are the level of surface damage and oxidation. These could be explained in terms of a longer residence time in the grinding circuit or the effects of geological conditions. In this respect the contribution of morphology and surface features relative to other effects such as surface oxidation or surface precipitates should be confirmed.

Fine particles were still aggregated on the surface of molybdenite but the amount of slime cover was not as significant as it was for the LSE ore. Molybdenite particles in the rougher concentrate were observed to be fully liberated but with a slightly oxidized surface. Only Mo and S signals were found at the surface (Spot # 1) according to EDS analysis. The tails were a mixture of locked molybdenite particles (~10%) and fully liberated molybdenite particles (~90% %) and greater Ca and Si silicate contaminations were found at the molybdenite surfaces in the MZ2S rougher tailings, as shown on the EDS spectrum in Figure 5.16 (c). Also, some indication of gangue (dark) phases can be seen on the magnified SEM image presented in Figure 5.17 (a). The gangue minerals embedded on the soft surface of molybdenite were mostly quartz (dark phases) followed by very small amounts of illite, dolomite, and calcite. According to EDS analysis of the selected area in Figure 5.17 (b), apart from Mo and S signals, minor Fe signals are found at the molybdenite face. It is known that iron species are released into the pulp during comminution due to the presence of iron minerals in the ore. When both Fe and Ca species are present the zeta potential becomes higher, which decreases the interaction between molybdenite particles and bubbles and reduces the flotation recovery of

molybdenite. Zhou (2010) reported a similar finding that the depressant effect of Fe^{3+} on molybdenite flotation is strongest at pH 11 and the presence of Ca^{2+} enhances this effect. As has been reported by many researchers, water chemistry plays a tremendous role in molybdenite flotation in this kind of ore due to the highly reactive edge surfaces of the molybdenite particles, especially for fine molybdenite particles with large edge-to-face ratios. Figure 5.17 also presents the magnified SEM image of the molybdenite and gangue association and the corresponding EDS spectrum is consistent with the high abundance of quartz at the molybdenite surface. Quartz particles were considered to be embedded or interlocked into the surface of the molybdenite, as well as being trapped within the striated layers and particles causing high surface damage. This may be responsible for the low Mo flotation recovery.

According to Fuerstenau and Chander (1972), "polar surfaces are produced when the molybdenite crystal is broken along the edges. These polar surfaces are chemically active with water with the formation of thio-molybdates and the species $HMoO^{4-}$ and MoO_4^{2-} determine the electric charge at the edges and contribute to a more hydrophilic characteristic." It was evident that the hydrophobicity and floatability of molydenite particles in the MZ2S sample decreased due to the ratio of face and edge and/or the surface oxidation. Mostly, it is expected that the calcium ions absorbed at the edges and micro-edges of the particle, cause a significant effect on the floatability of molybdenite as a function of the pH.

As previously reported for the Cu size-by-size recovery curve (see Figure 5.7), the Cu loss was significant in the 150x75 μm size fraction of the MZ2S rougher tailings. Detailed analysis using SEM-EDS was undertaken on the chalcopyrite particle isolated

from this size fraction and the results are presented in Figure 5.18. Figure 5.18 demonstrates that chalcopyrite particles from the rougher tailings were fully liberated with a clean, smooth surface and had relatively no slime attachments, however, these particles have an O signal apart from the Cu, Fe, and S signals. This could explain the low probability of adhesion of the particles to air bubbles due to surface oxidation, which leads to a low Cu flotation rate.

On average, 8-10 molybdenite particles were randomly selected for SEM-EDS and SEM imaging analysis from the coarse 300x150 μm size fraction for each ore. Results showed that most molybdenite particles in the coarse size fraction were flat, smooth and fully liberated but had significant surface damage or deformation either due to geological conditions and/or the grinding operation. As described by other researchers, hydrophobicity of molybdenite particles is determined by the relative surface exposure of faces (hydrophobic) and edges (hydrophilic). In flotation, molybdenite particles with higher exposure of edges will have lower probability of attachment to air bubbles on collision. The loss of these coarse molybdenite particles could be caused by many factors such as the bridging effect of Ca^{2+} ions, slime coating, contact angle, ratio of face to edge and hydrodynamic effects. In general, the presence of hydrophilic edges on the damaged and striated surface may prevent the spreading of oily Mo collectors at hydrophobic face surfaces, thus reducing Mo recovery. This phenomenon is observed in each rougher tailing containing coarse molybdenite particles. Also, at least two to three of these selected coarse molybdenite particles were interlocked or associated with other minerals, as displayed in Figure 5.19. In this case, gangue minerals could be embedded directly into the soft surface of molybdenite during the grinding operation. As mentioned

previously, approximately 30 % of the Mo loss for each ore type was in this coarse 300x150 µm size fraction. These particles definitely need to be separated and ground to a certain size to increase liberation during flotation. In this way, grade and recovery could be improved.

5.3.5 Surface oxidation using XPS analysis

In previous Sections, liberation and SEM-EDS and SEM imaging analysis were used to analyze the surface of molybdenite. All discussion was based on experimental results and other results reported the literature. In the present section, X-ray photoelectron spectroscopy will be applied to study the surface of the molybdenite particles and to link the results to previous conclusions.

XPS spectra of molybdenite were collected using a Kratos Axis Ultra X-ray photoelectron spectrometer equipped with a 2.5 kV ion gun (with the beam current typically 1 µA cm^{-2}) for over layer sputter erosion and depth profiling. The spectrometer was calibrated using the metallic Au 4f. A monochromatic Al K_α X-ray source ($hv = 1486\ eV$) was used. The working pressure in the ultra high vacuum chamber for the data acquisition was kept below 10^{-8} torr. The element library and the quantification factors used here for quantitative analysis were provided via the system Casa XPS software. Two different scans were made on a selected area of the molybdenite surface: a survey scan and high-resolution scan. Energy peaks in the survey scan identify the elemental composition of the analyzed surface. Detection limits are approximately 0.1 atom percent for most elements. The scanned area and depth for XPS on the molybdenite surface were 300 µm x 300 µm and 10 nm, respectively. Typical analysis requires 3 - 4 minutes for

survey analysis, and 5 - 20 minutes per analysis point for high resolution scans, depending on the abundance of the element in question. Typical samples for XPS are 150x75 μm in size. The survey (full range) XPS spectrum of the molybdenite sample is provided in Figure 5.20.

A National Institute of Standards and Technology (NIST) database (http://srdata.nist.gov/xps/) is available to identify binding energies for specific compounds, which are shown in Table 5.10. In the molybdenite surface analysis, the corresponding binding energies were selected as E = 162.66 eV for the S ($2p_{3/2}$) line, E = 229.81 *e*V for the Mo ($3d_{5/2}$) component, an E = 532.8 eV for the O (1s) signal. The O (1s) peak may be related to air contamination of the samples or surface oxidation of the molybdenite and it could be scattered because the oxygen species involved were difficult to specify with confidence. Figure 5.20 presents the spectrum showing the carbon, oxygen, molybdenite and sulfur peaks for molybdenite particles isolated from the rougher concentrate and rougher tailings of the LSE and MZ2S ore types. The high-resolution XPS spectra in the S (2p) and Mo (3d) regions for all the samples investigated are displayed in Figure 5.21.

The binding energies (*E)* and the full width at half maximum (FWHM) of the peaks were determined by optimized peak-synthesis using a Gaussian line shape. The spectrum of the molybdenite sample in the concentrate generally showed a soft, partially resolved S (2p) doublet, a sharp Mo (3d) doublet and a weak broad O (1s) band (not shown). The two doublets identified are characteristic of the S^{2-} and Mo^{4+} features present at the surface of a normal MoS_2 sample. However, the spectrum of the molybdenite sample in the MZ2S tailings presented in Figure 5.21 shows that a new broad doublet appeared in

the S (2p) region (not shown) located at a higher binding energy than that of the original S (2p) doublet, with the Mo (3d) signal now giving a three-peak structure derived from two overlapping doublets. According to Spevak (1993), it was identified that this new doublet was the Mo (3d) peaks of oxidized molybdenite Mo^{6+} (MoO_3 or $CaMoO_4$) produced from the Mo^{4+} (MoS_2) in the rougher tailings sample by oxidation. The corresponding binding energy value of the new peak was 236.4 eV for Mo^{6+}, as given in Table 5.10.

XPS results revealed that MoO_3 and SO_4^{2-} species were the major oxidation products at the molybdenite surface. It can be seen from Figure 5.21 that both the sulfur and molybdenite species, present in the sample of MZ2S rougher tailings, were oxidized. Apart from that, the elemental composition (atom %) for all the samples studied and the corresponding atomic fractions of the different sulfur and molybdenum species, as determined from the XPS data, are presented in Table 5.11.

According to these XPS values, the oxidation state of the molybdenite particles in the rougher tailings were validated. The O fraction in Table 5.11 demonstrates a trend of increasing oxygen from concentrate to tailings with the slower floating molybdenite particles in the rougher tailings. During Cu-Mo flotation, it was evident that the fastest floating particles in the rougher concentrate have the highest surface sulfur and the lowest amount of oxygen on their surface. It means that surface sulfur is responsible for the natural hydrophobicity of the molybdenite. In general, tailings particles should have a lower concentration of sulfur than concentrate particles.

Depending on the surface roughness and topography, these trends may not be seen from the atomic fraction values of the Mo, S and O signals, derived from XPS spectra.

Nevertheless, atomic ratios and the percentages of different Mo and S species of selected particles could clearly reveal the surface oxidation states based on these values. With regard to the atomic percentage of the concentrate and tailings of the MZ2S molybdenite at pH=10, the surface S/Mo ratio in the tailings (1.53) was significantly lower than that in the concentrate (1.82), which suggests that the tailings sample was more oxidized than the concentrate and explains why the tailing molybdenite was not floated.

This S/Mo ratio indicates loss of sulfur from the surface or near surface region of the samples affected by an oxidation reaction. It could be hypothized that the loss of molybdenite particles in the MZ2S rougher tailings strongly depends on the oxidation state of their surface. It is important to note that this behavior was not observed for LSE molybdenite particles in the rougher tailings.

XPS analyses were undertaken in order to examine the surface species on the molybdenite isolated from both concentrates and tails and to enable identification of surface species that contribute to specific flotation behaviors, e.g., hydrophilic edges created during surface oxidation and grinding that result in value minerals reporting to the tails. It was found that surface sulfur (S^{2-}) of molybdenite in MZ2S rougher tailings was significantly decreased for the slower floating particles, whereas surface oxidation and calcium coating predominated.

5.4 Summary and recommendations

In general, the combination of information from size distribution analysis, HRXMT, SEM-EDS, XPS and SEM imaging has clarified the following aspects of the liberation state and the surface properties of Cu and especially Mo particles in flotation tailings and

the extent to which these factors influence the flotation separation efficiency: (1) Cu and Mo distribution in both feed and tailings of rougher flotation were determined for each ore type and the relative size-by-size recoveries of different size fractions determined. (2) The liberation characteristics of molybdenite particles in the LSE and MZ2S rougher tailings were quantitatively estimated by the 3D object counter plug-in using ImageJ software and the results were compared with 3D reconstructed images. (3) The surface properties of molybdenite particles were examined by SEM and XPS analysises. Interesting findings that were made from the results of SEM and XPS analysis include:

a) Gangue mineral fines were found attached or embedded to most coarse and medium molybdenite particles in the rougher tailings;
b) Chalcopyrite in the tailings from the rougher flotation appeared to be locked particles for all ore types;
c) Molybdenite in the tailings appeared to be fully liberated but several factors have been identified that could affect molybdenite flotation efficiency, all of them primarily related to the surface properties of molybdenite. For example, the adsorption of oily collector at the molybdenite surfaces appeared to be inhibited by the presence of fine gangue mineral particles and/or calcium precipitates due to surface damage, surface oxidation, and the concentration of the contaminants in the process water.

The molybdenite particles in the LSE tailings appeared to be considerably covered by slime minerals. In the case of the MZ2S tailings, molybdenite appeared to be oxidized to an oxide species with evident precipitates, corresponding to powellite ($CaMoO_4$) in both composition and morphology, adhering to their surfaces.

From these parallel analyses, it has been possible to identify the contributing morphological and surface chemical factors resulting in the observed flotation behavior of molybdenite particles. For example, the major factors affecting the MZ2S ore and the general conclusions from detailed characterization analysis regarding the flotation characteristics and their impact on flotation plant efficiency are outlined in Figure 5.22.

It was concluded that, approximately 89.0 % of the Cu and 83.2 % of the Mo were recovered in the LSE rougher concentrate during flotation testing. Detailed characterization analysis results of the Mo recovery are highlighted. LSE rougher tailings accounts for 16.8 % of Mo losses. Of the 16.8 % molybdenum loss:

- 6.0 % was in the coarse and medium size fractions. Fully liberated particles that reported to the tailings had higher levels of calcium ions and slime coating on their particle surfaces than recovered molybdenite, indicating that slime was actively depressing molybdenite particles and that desliming or high shear mixing could remove the slime cover and improve flotation efficiency.
- 0.2 % were locked or partially liberated particles distributed in the same size fractions and the average size of these particles was approximately 20 µm.
- 6.1 % were fully liberated slime particles distributed in the fine and ultra fine size fractions. This could be due to slime aggregation. Dispersants or ultrasonic treatment are widely used to modify the colloidal interactions between gangue particles and can disperse the clay particles and increase the flotation recovery of the minerals, reducing the required collector dosage
- The remaining 4.5 % had no slime attached and were completely liberated particles, but reported to flotation tailings. The reason for Mo loss was un-

predictable. It could have been related to hydrodynamic effects such as attachment or collision probability during froth flotation.

In the case of the MZ2S ore, 9.7 % Cu and 29.8 % Mo was lost into the rougher tailings. Of the 29.8 % molybdenum loss:

- 7.6 % of the total Mo loss was fully liberated particles distributed in the fines (37 μm) and ultra-fine (25 μm) size fractions.
- 22.2 % of the Mo loss was distributed in the coarse and medium size fractions. Only 0.4 % of them were observed in low grade middling particles presented as locked inside of gangue minerals and/or by remnants on the surface of quartz particles that might require regrinding to achieve liberation. Approximately 18.4 % of the lost particles were fully liberated but did not break during the grinding process. Nevertheless, their surfaces were highly damaged, oxidized (65 %) and contaminated by gangue minerals (18 %). Hence, Mo particles lost in the tailings were strongly oxidized and had high levels of surface oxidation such as powellite ($CaMoO_4$) on particle surfaces, indicating that surface oxidation was a main issue for Mo loss.
- The remaining Mo loss (6.5 %) was distributed in the intermediate size fractions. Most particles were fully liberated, relatively clean and un-oxidized surfaces. Even after several detailed characterization analyses, the reason for Mo loss was really unpredictable and was not expected. It could be related to the effect of process water or the hydrodynamic effects such as attachment or collision probability during froth flotation.

Based on the most significant limitation to flotation efficiency, reflotation

experiments were carried out on the LSE and MZ2S rougher tailings to evaluate possible alternatives for improved flotation recovery of Cu and Mo. In the case of the LSE and MZ2S samples, the estimated Mo losses related to slime coating were 3.8 % and 3.3 %, respectively. A combination of desliming, with a screening to remove fines below 37 μm in size, and high shear mixing to activate the oxidized surface could be the simplest and easiest choice to improve Cu and Mo recovery or verify results of the characterization analysis.

Based on the results of reflotation testing, the average Cu and Mo recoveries of the LSE sample were increased by 2.4 % and 4.2 %, respectively. In the case of the MZ2S sample, the average Cu and Mo recoveries were increased by approximately 1.7 % and 3.7 %, respectively. A summary of the results for the reflotation experiments are shown in Appendix A. A moderate addition of Cytec 8989 and burner oil at 0.01 lb/t and 0.05 lb/t, slurry pH of 9.5 and flotation time of 10 min were sufficient to achieve these results.

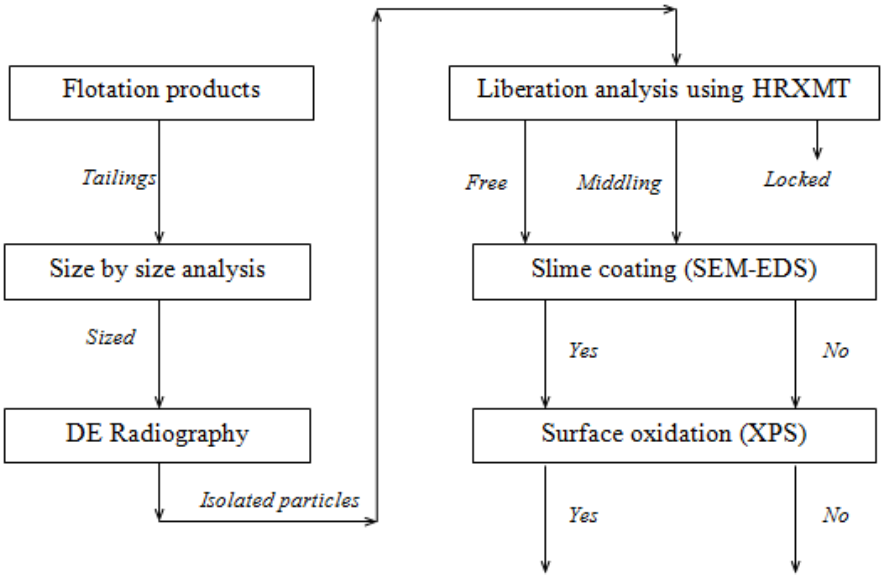

Figure 5.1 A schematic diagram of the detailed characterization analysis of lost mineral particles.

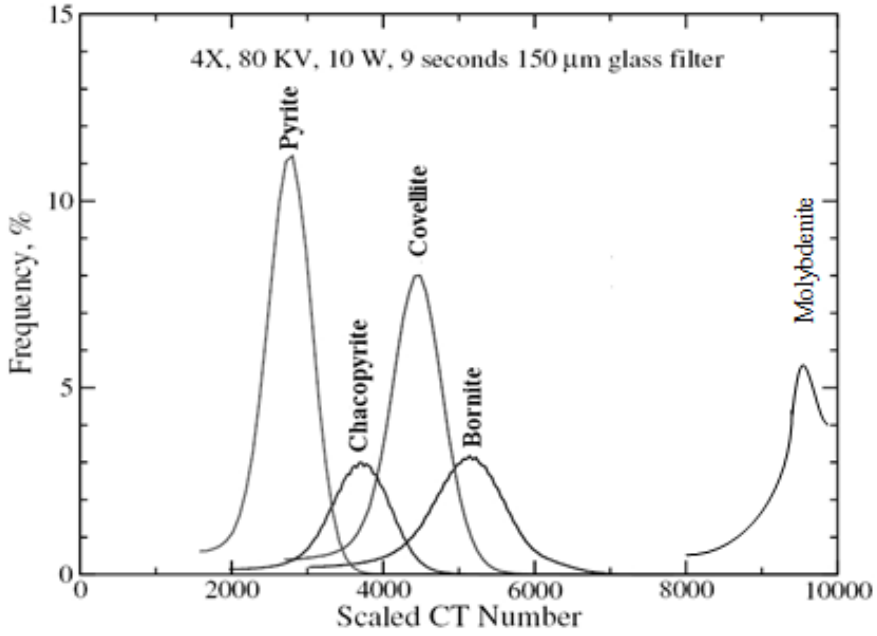

Figure 5.2 The values of each CT number for sulfide mineral phases at a voxel resolution of 5 µm (adapted from Medina, 2012).

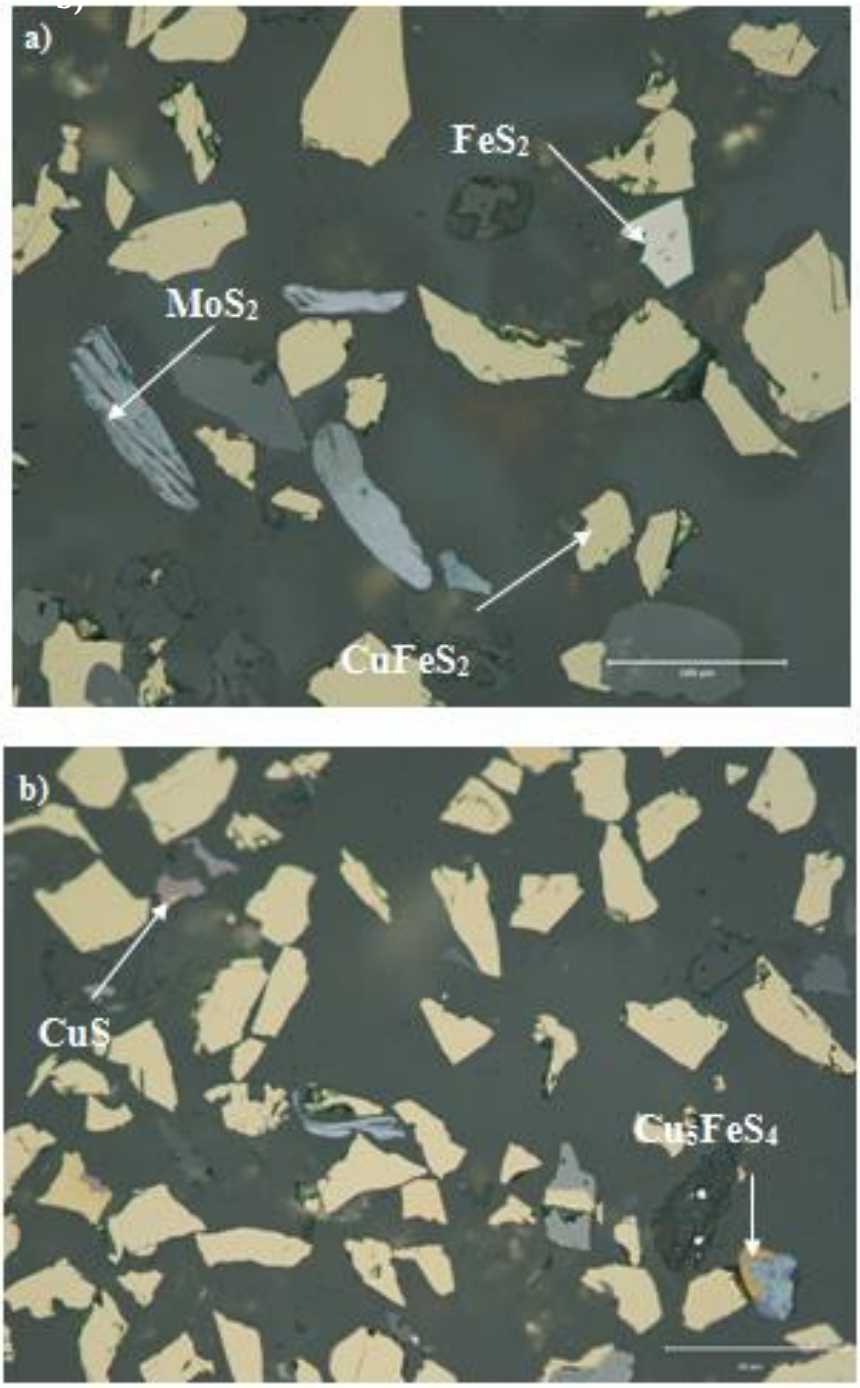

Figure 5.3 SEM backscattered images of chalcopyrite and molybdenite particles from rougher concentrate for the MZ2HE ore. a) 300x150 µm; b) 150x75 µm.

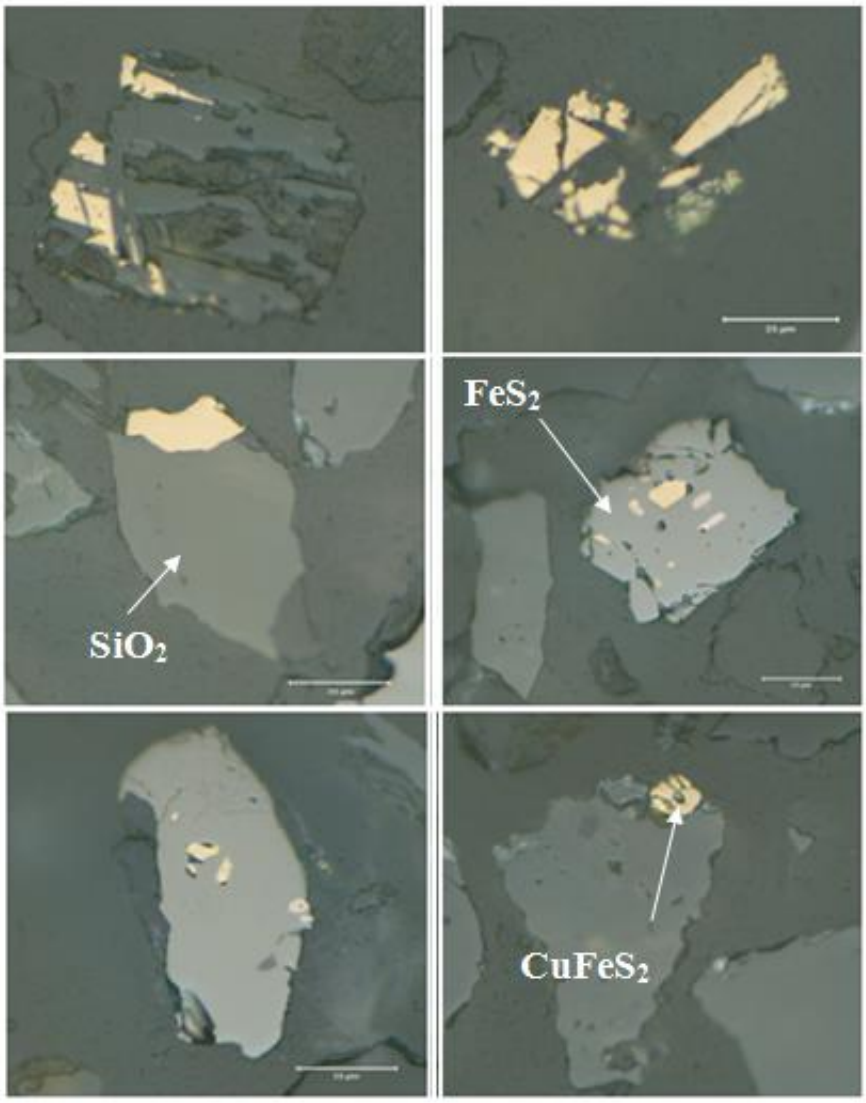

Figure 5.4 SEM backscattered images of locked chalcopyrite particles (150x75 μm) from rougher tailings for the MZ2HE ore.

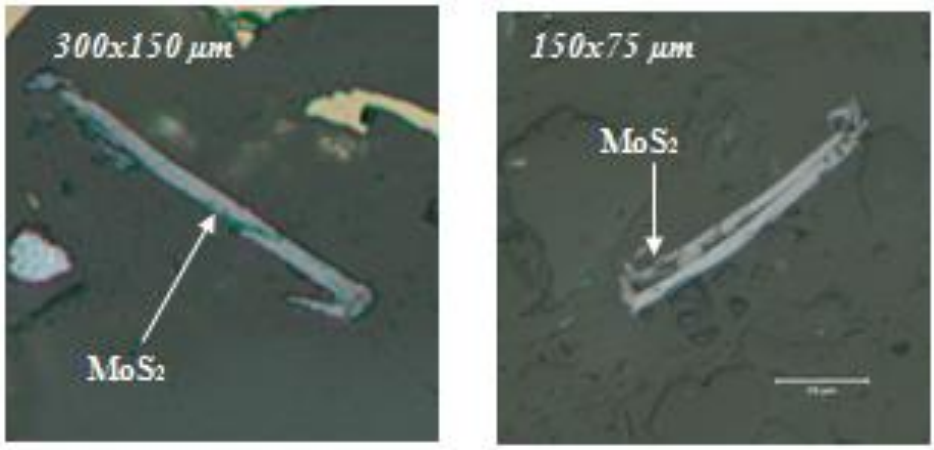

Figure 5.5 SEM backscattered images of 300x150 µm and 150x75 µm molybdenite particles from rougher tailings of the MZ2S ore.

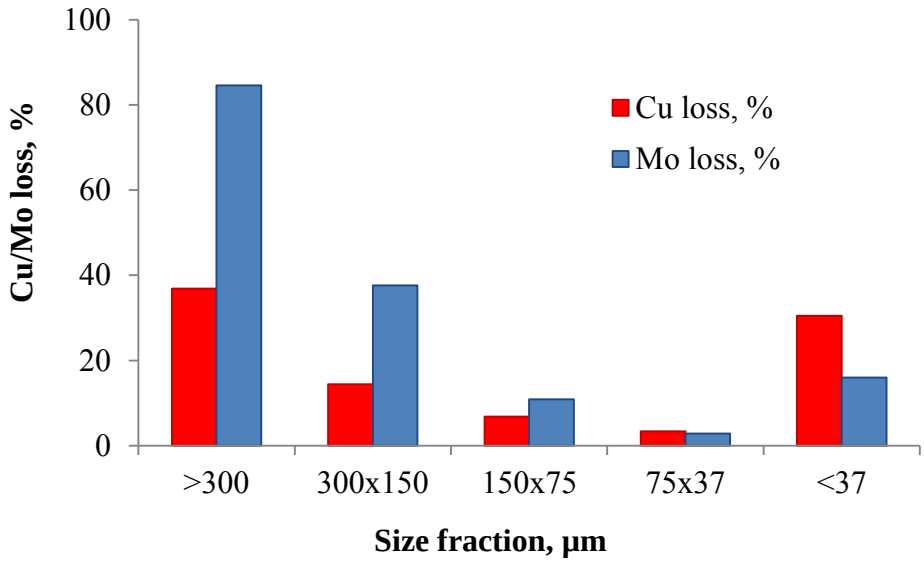

Figure 5.6 Copper and molybdenum loss in the rougher tailings of the MZ2HE ore.

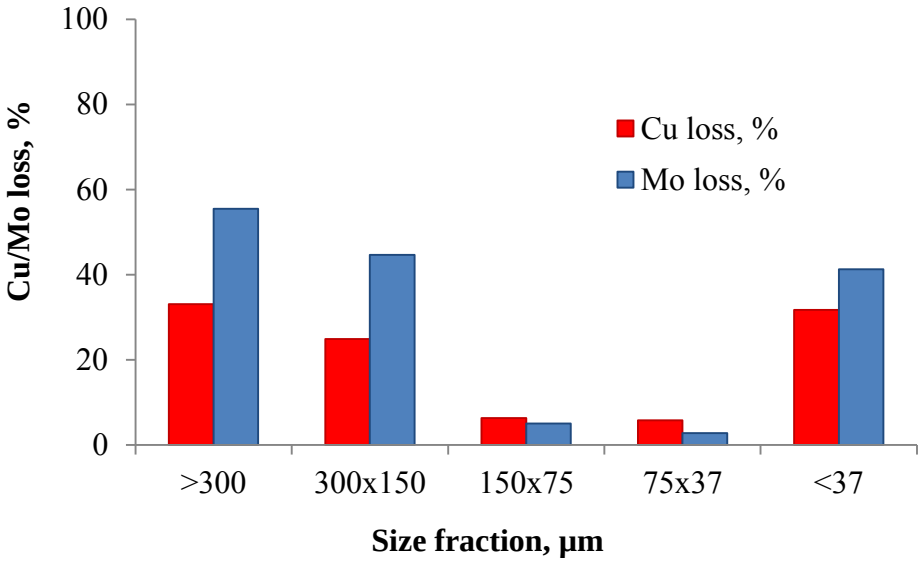

Figure 5.7 Copper and molybdenum loss in the rougher tailings of the LSE ore.

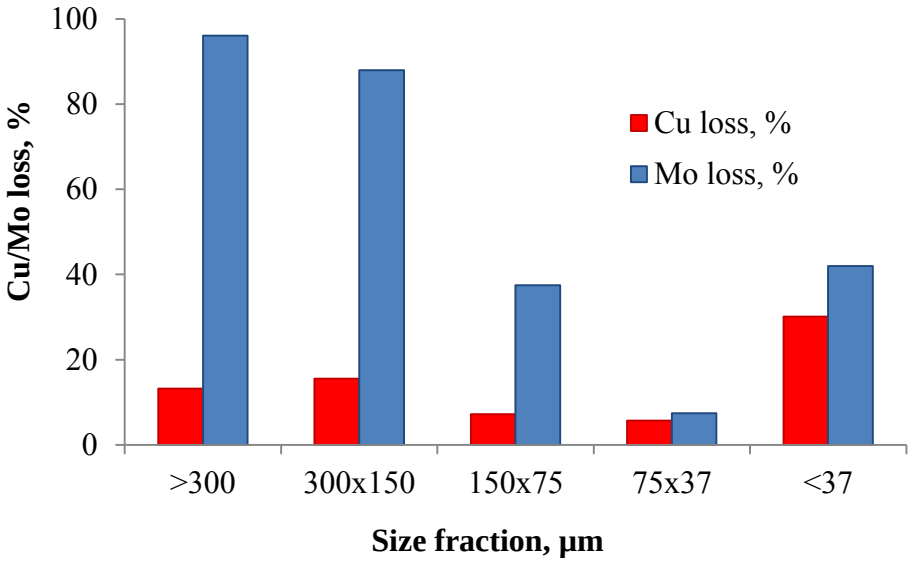

Figure 5.8 Copper and molybdenum loss in the rougher tailings of MZ2S ore.

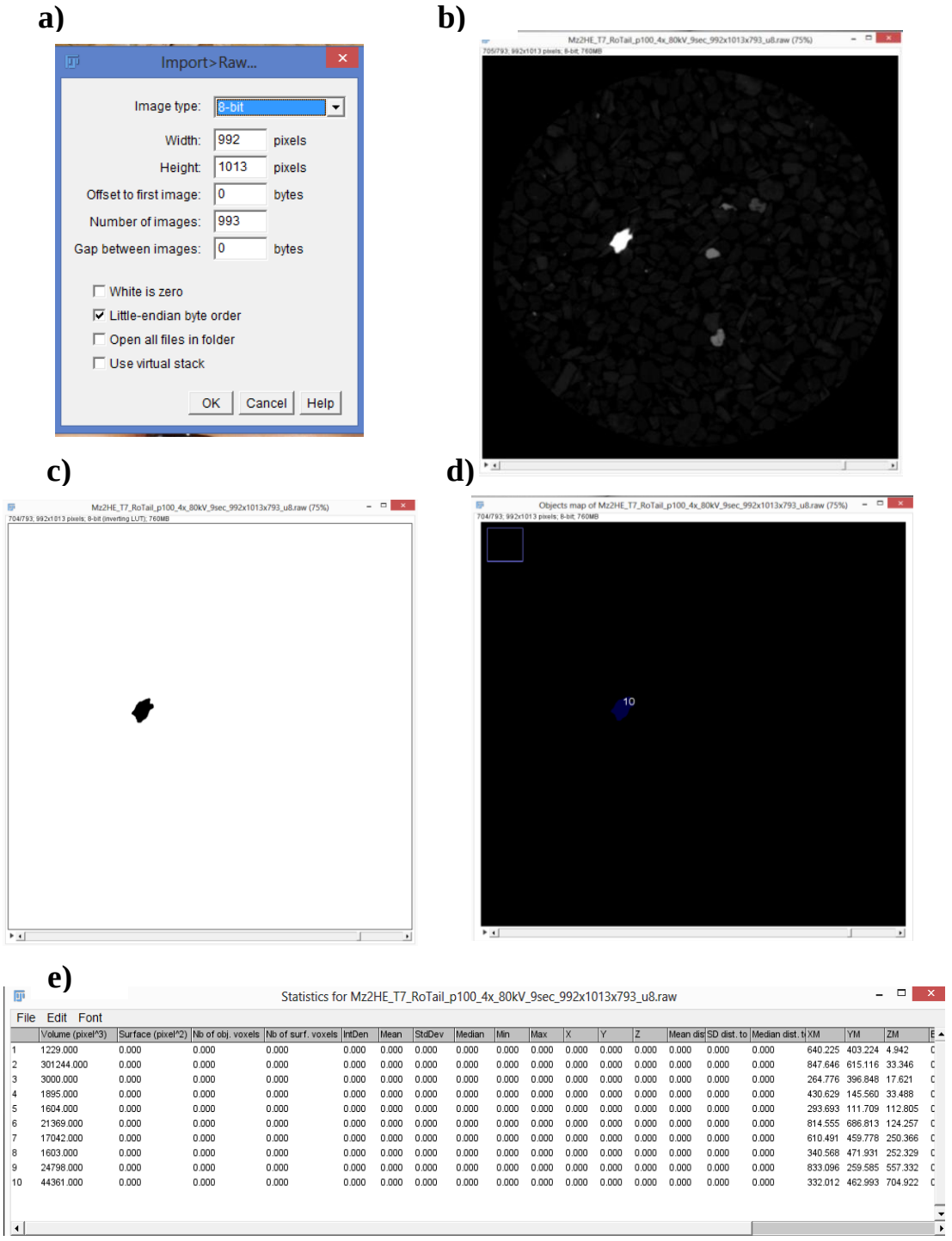

	Volume (pixel^3)	Surface (pixel^2)	Nb of obj. voxels	Nb of surf. voxels	IntDen	Mean	StdDev	Median	Min	Max	X	Y	Z	Mean dis	SD dist. to	Median dist. t	XM	YM	ZM
1	1229.000	0.000	0.000	0.000	0.000	0.000	0.000	0.000	0.000	0.000	0.000	0.000	0.000	0.000	0.000	0.000	640.225	403.224	4.942
2	301244.000	0.000	0.000	0.000	0.000	0.000	0.000	0.000	0.000	0.000	0.000	0.000	0.000	0.000	0.000	0.000	847.646	615.116	33.346
3	3000.000	0.000	0.000	0.000	0.000	0.000	0.000	0.000	0.000	0.000	0.000	0.000	0.000	0.000	0.000	0.000	264.776	396.848	17.621
4	1895.000	0.000	0.000	0.000	0.000	0.000	0.000	0.000	0.000	0.000	0.000	0.000	0.000	0.000	0.000	0.000	430.629	145.560	33.488
5	1604.000	0.000	0.000	0.000	0.000	0.000	0.000	0.000	0.000	0.000	0.000	0.000	0.000	0.000	0.000	0.000	293.693	111.709	112.805
6	21369.000	0.000	0.000	0.000	0.000	0.000	0.000	0.000	0.000	0.000	0.000	0.000	0.000	0.000	0.000	0.000	814.555	686.813	124.257
7	17042.000	0.000	0.000	0.000	0.000	0.000	0.000	0.000	0.000	0.000	0.000	0.000	0.000	0.000	0.000	0.000	610.491	459.778	250.366
8	1603.000	0.000	0.000	0.000	0.000	0.000	0.000	0.000	0.000	0.000	0.000	0.000	0.000	0.000	0.000	0.000	340.568	471.931	252.329
9	24798.000	0.000	0.000	0.000	0.000	0.000	0.000	0.000	0.000	0.000	0.000	0.000	0.000	0.000	0.000	0.000	833.096	259.585	557.332
10	44361.000	0.000	0.000	0.000	0.000	0.000	0.000	0.000	0.000	0.000	0.000	0.000	0.000	0.000	0.000	0.000	332.012	462.993	704.922

Figure 5.9 ImageJ 3D object counter plug-in. Image of particles counted as part of analysis and data table generated by ImageJ. a) 3D object counter dialog box; b) image of molybdenite particles prior to tresholding; c) threshold adjustment to match particles; d) thresholded particles are numbered as shown to allow for exact measurement tracking of molybdenite particles; e) data table can be saved as .xls and imported into a spreadsheet software such as Excel.

a) Size class – 300x150 µm

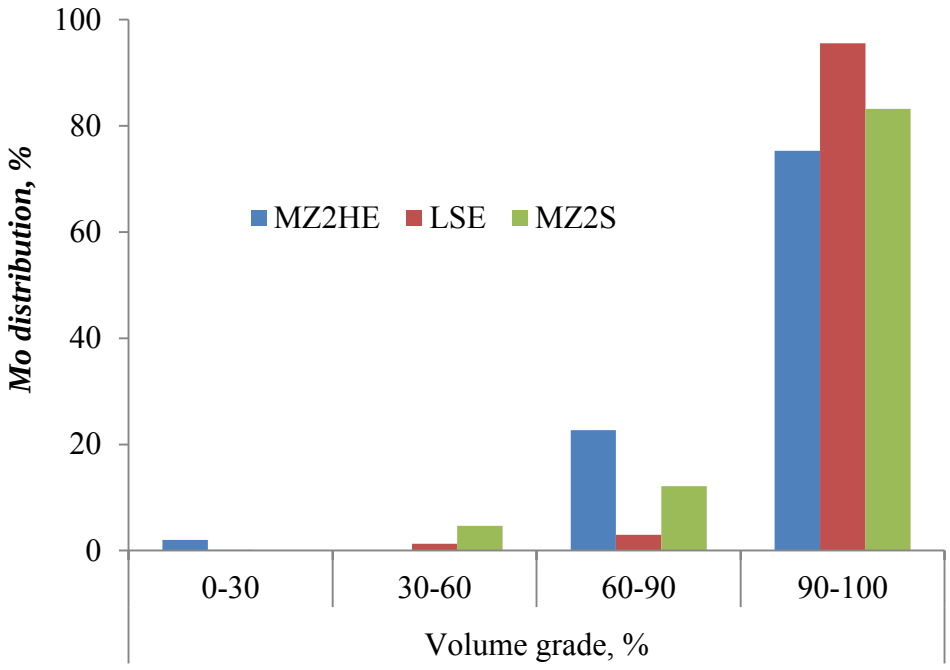

a) Size class – 150x75 µm

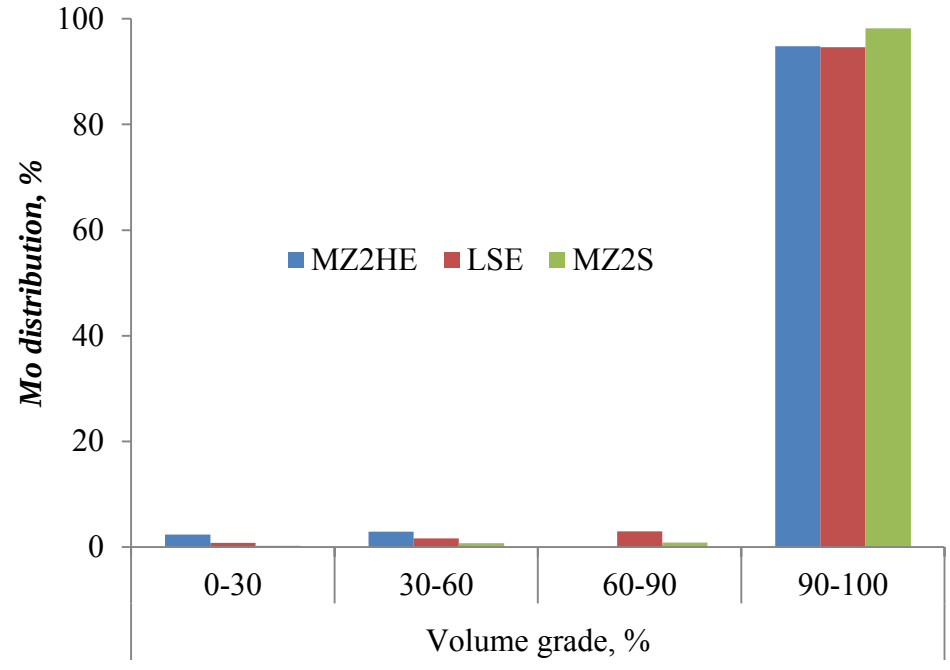

Figure 5.10 Molybdenum distributions in the rougher tailings of the MZ2HE, LSE and MZ2S ores.

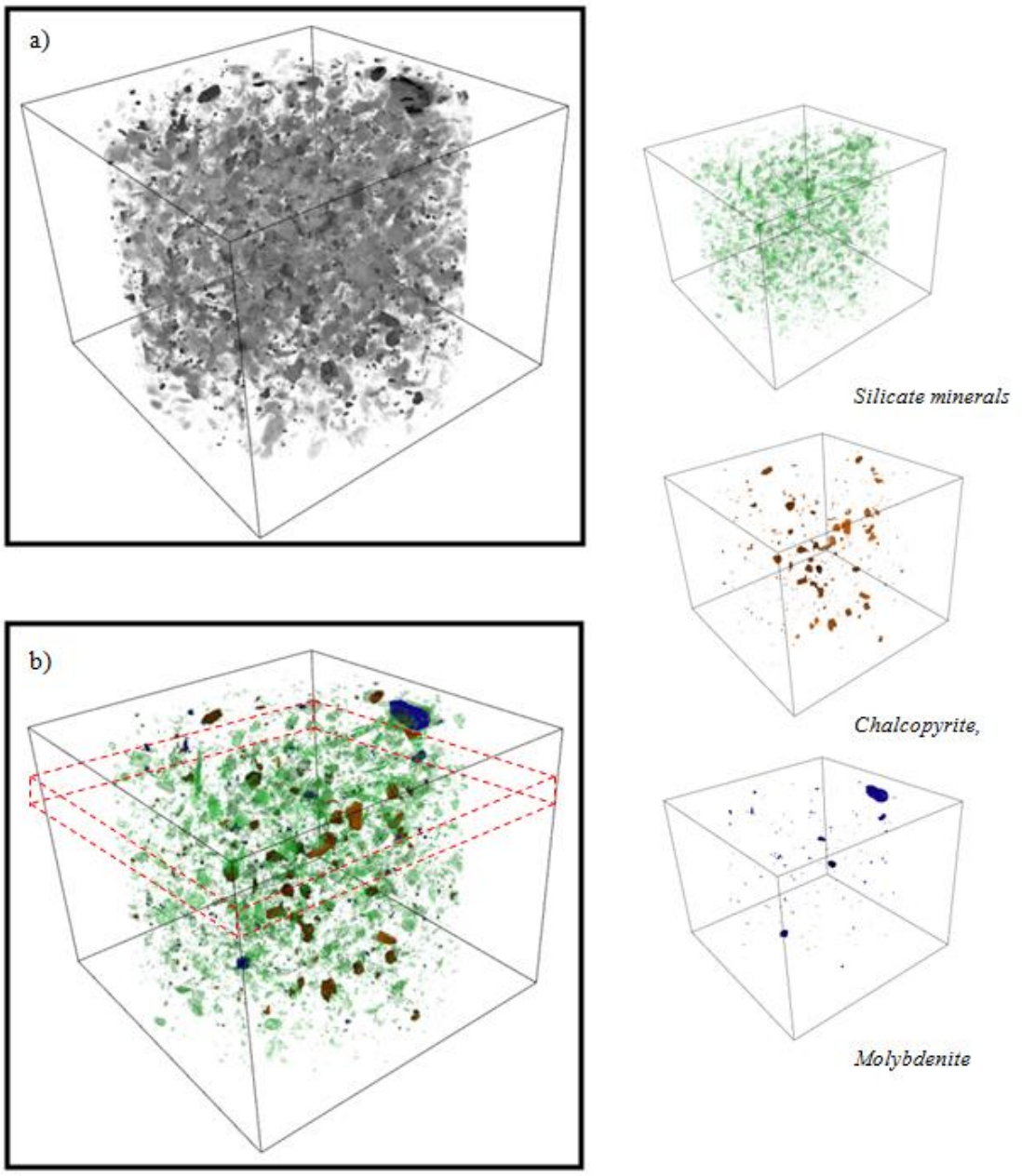

Figure 5.11 Reconstructed 3D rendered image of the packed bed of rougher tailings samples (250x150 µm) with a voxel resolution of 4.59 µm from HRXMT scans. The figures on the left show a complete view of the original (a) and segmented (b) HRXMT reconstructed image. The images on the right show separated low, medium, and high atomic number minerals. Image created with Drishti software.

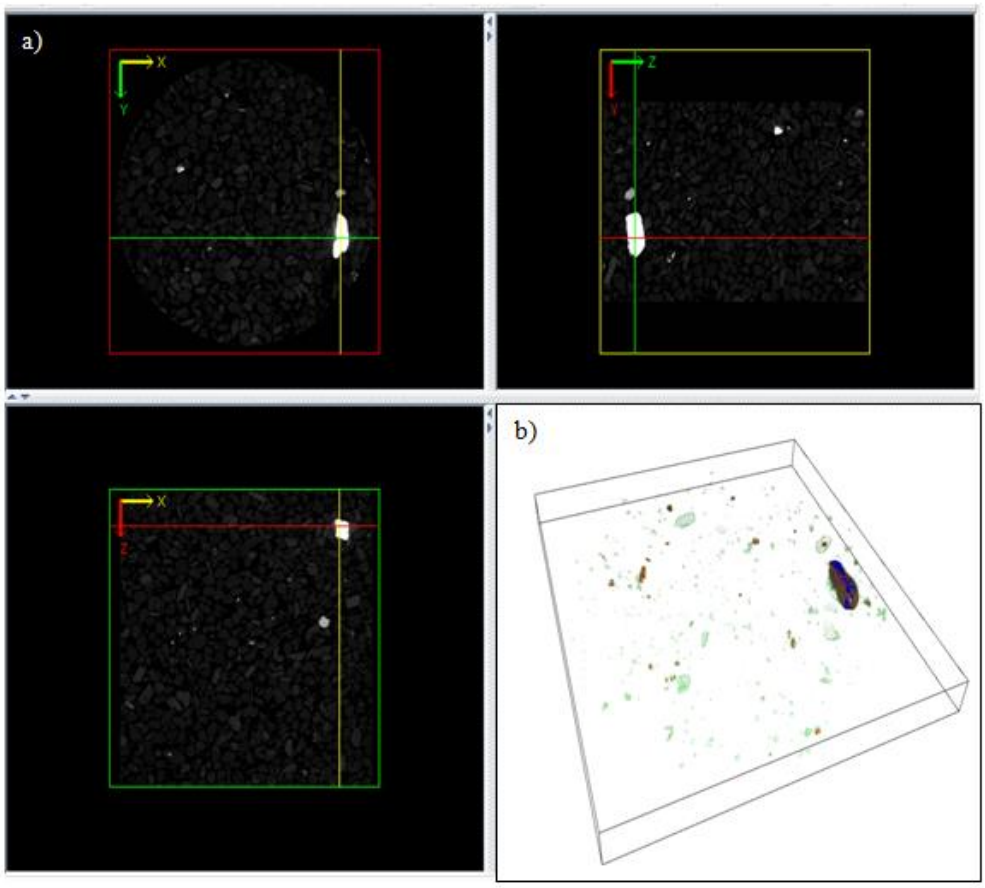

Figure 5.12 3D projections (a) showing the cross cursor locating at a detected molybdenite particle, (b) the cross section containing molybdenite particles (dark blue) taken out from the 3D reconstructed image shown in Figure 5.12. Image created with Drishti software.

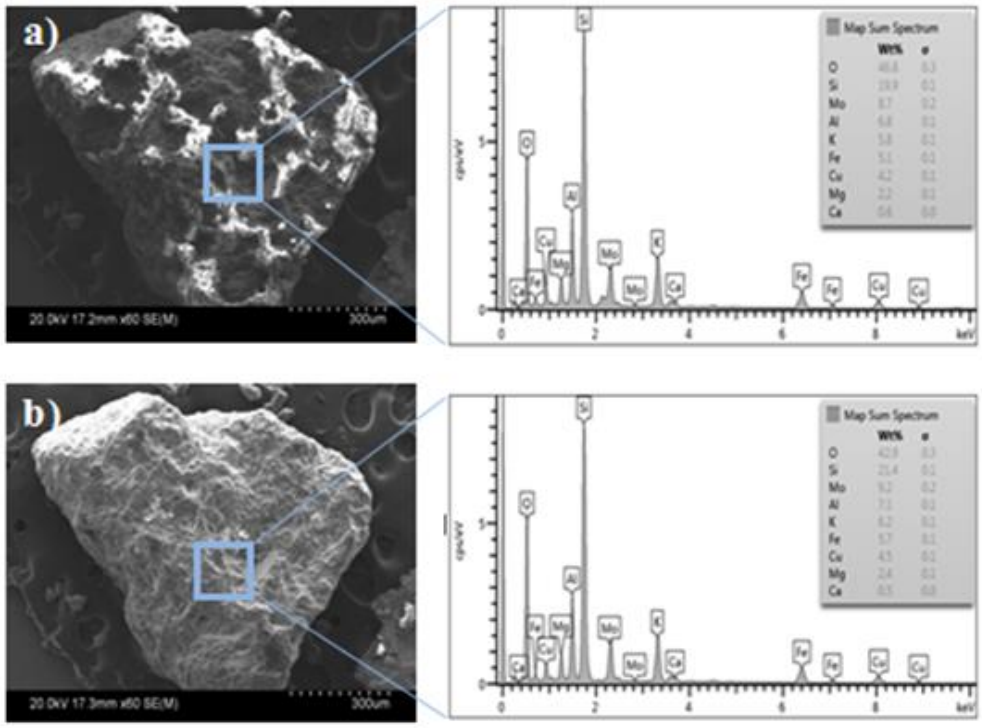

Figure 5.13 SEM image and corresponding EDS spectra of uncoated (a) and coated (b) molybdenite particle.

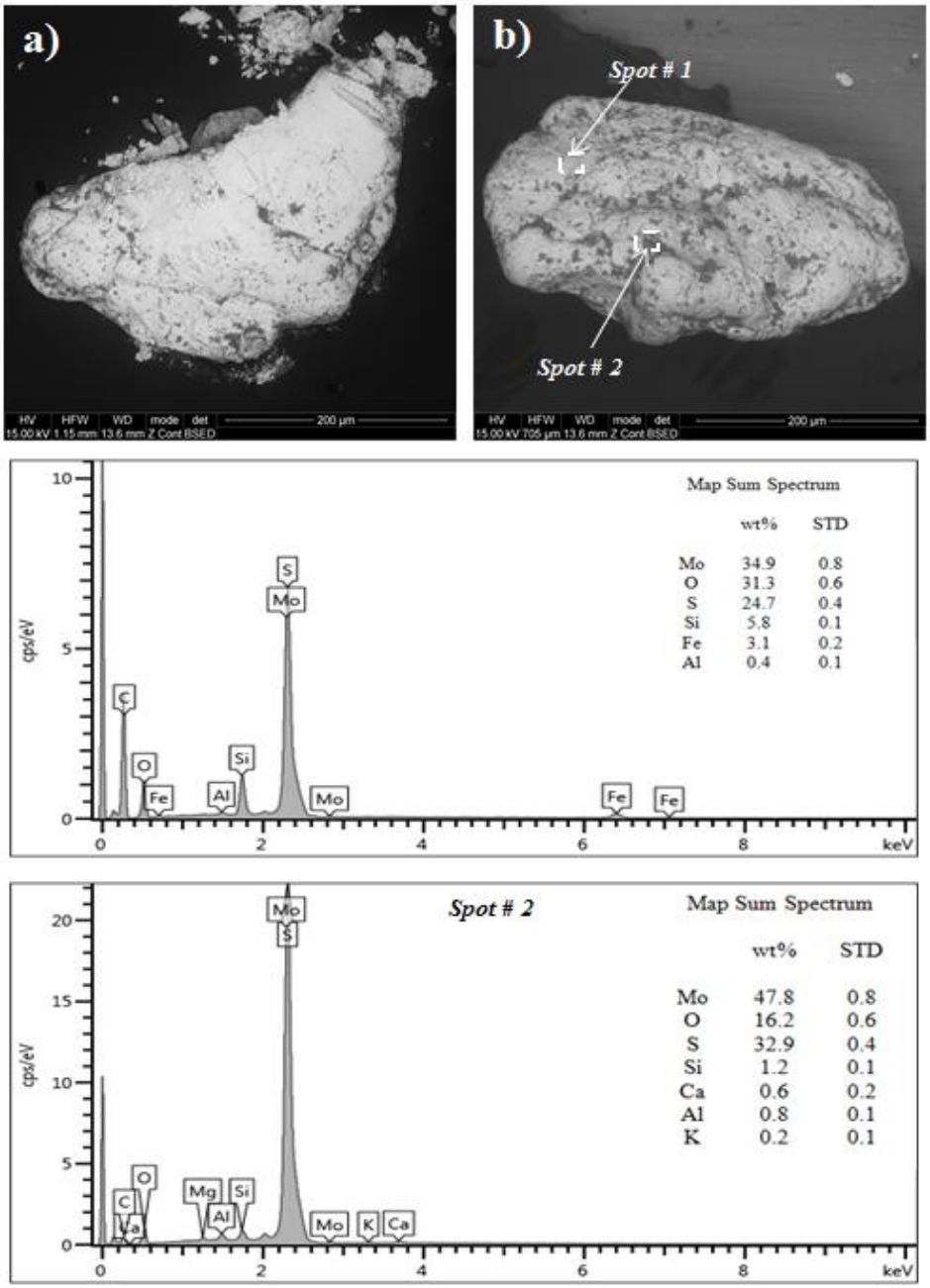

Figure 5.14 SEM back scattered images of LSE molybdenite particles from: rougher concentrate (a), rougher tailings (b). EDS spectra from the Spot # 1 and Spot # 2 indicating that slime minerals predominantly cover the molybdenite surface.

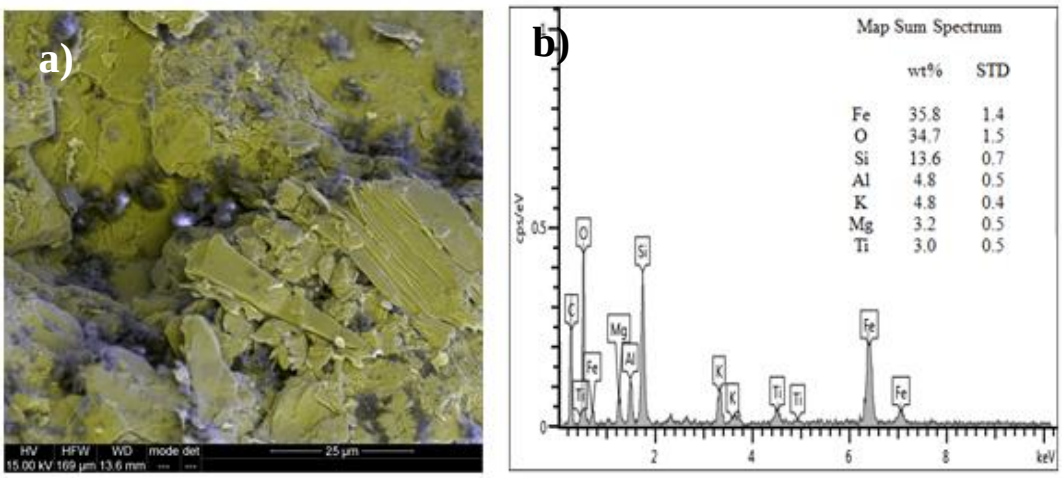

Figure 5.15 Magnified and X-ray mapped SEM image (a) of Spot # 2; distribution map for three different elements, in this case Mo (yellow), Si (grey) and O (white), can be combined in a three-band image. Composite colors are produced where different combinations of the elements are present in different phases in the sample. The EDS spectrum (b) indicates that slime minerals predominantly cover the molybdenite.

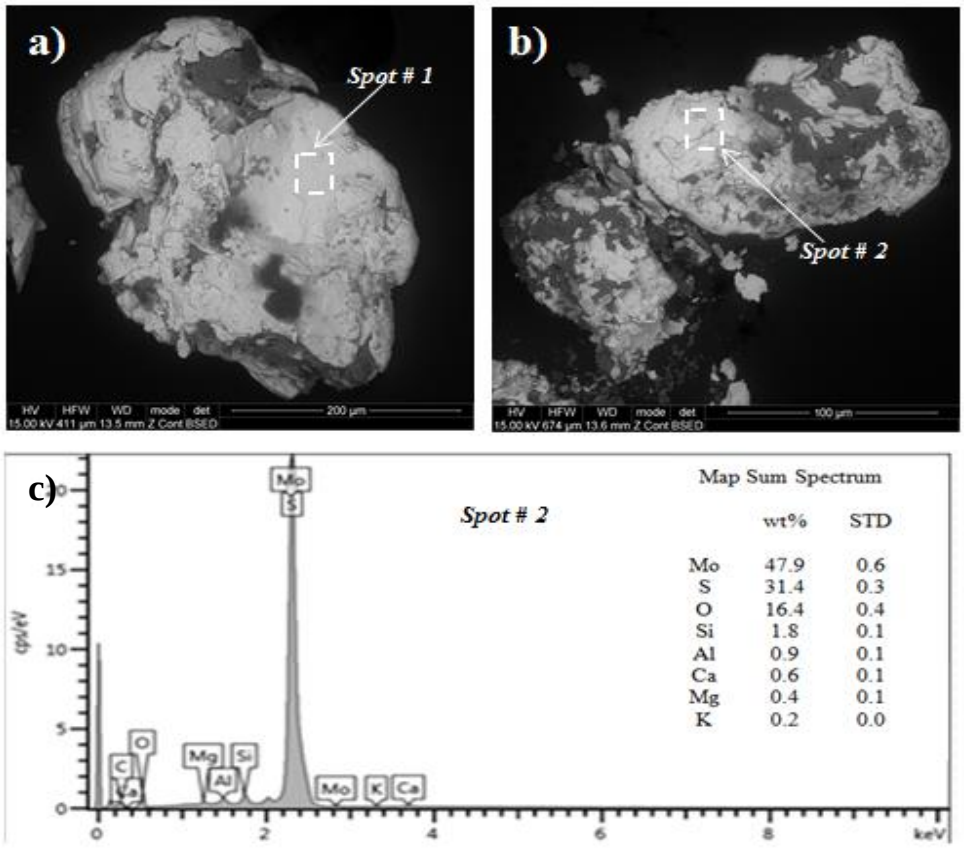

Figure 5.16 SEM back scattered images of the MZ2S molybdenite particles from: rougher concentrate (a), and rougher tailings (b). The EDS spectrum (c) from the region is shown in Figure 5.17 (b) indicating the heavily oxidized layer on the molybdenite.

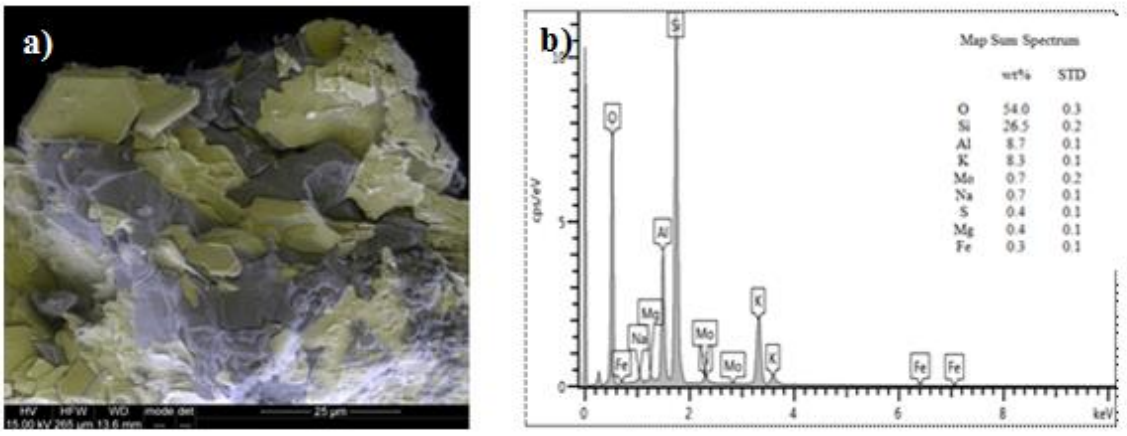

Figure 5.17 Magnified SEM micrograph (a) of the molybdenite surface from Spot # 2 shown in Figure 5.16. SEM back scattered electron micrograph of the surface of a molybdenite particle (150x75 µm), isolated from the MZ2S rougher tailings. The EDS spectrum (b) from the region shown in Figure 5.17 (a) indicates that the molybdenite surface was entirely oxidized.

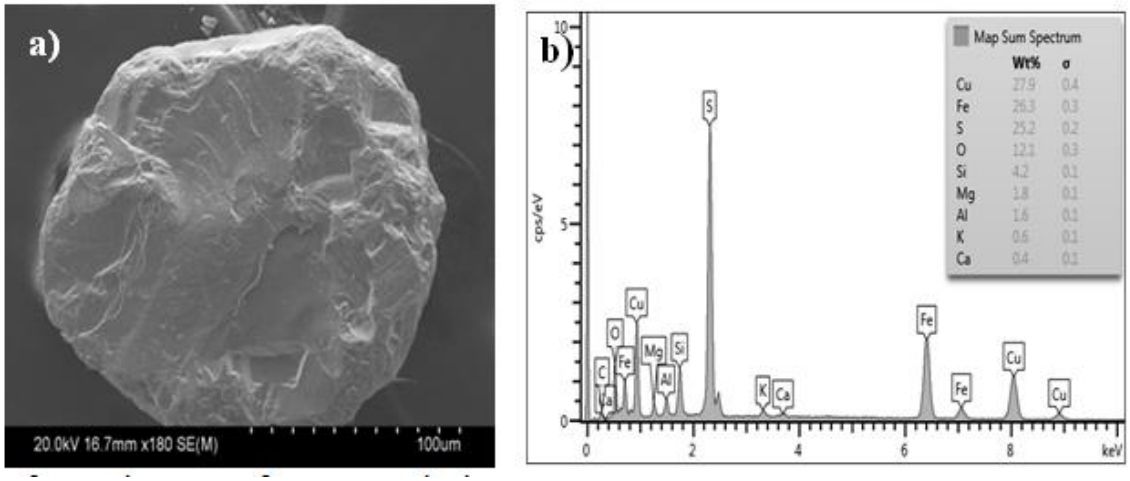

Figure 5.18 SEM image (a) and EDS (b) of a selected chalcopyrite particle, isolated from MZ2S rougher tailings. The corresponding EDS spectrum (b) from the region shown in Figure 5.18 (a) indicate that the chalcopyrite is strongly oxidized due to surface oxidation.

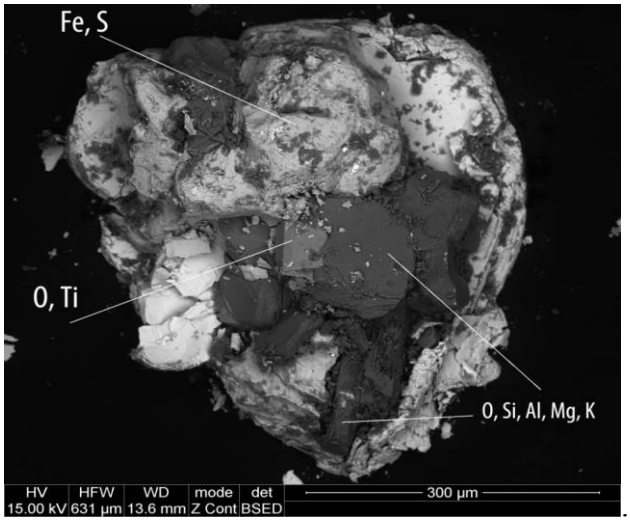

Figure 5.19 SEM image and EDS of a coarse molybdenite particle, isolated from MZ2S rougher tailings

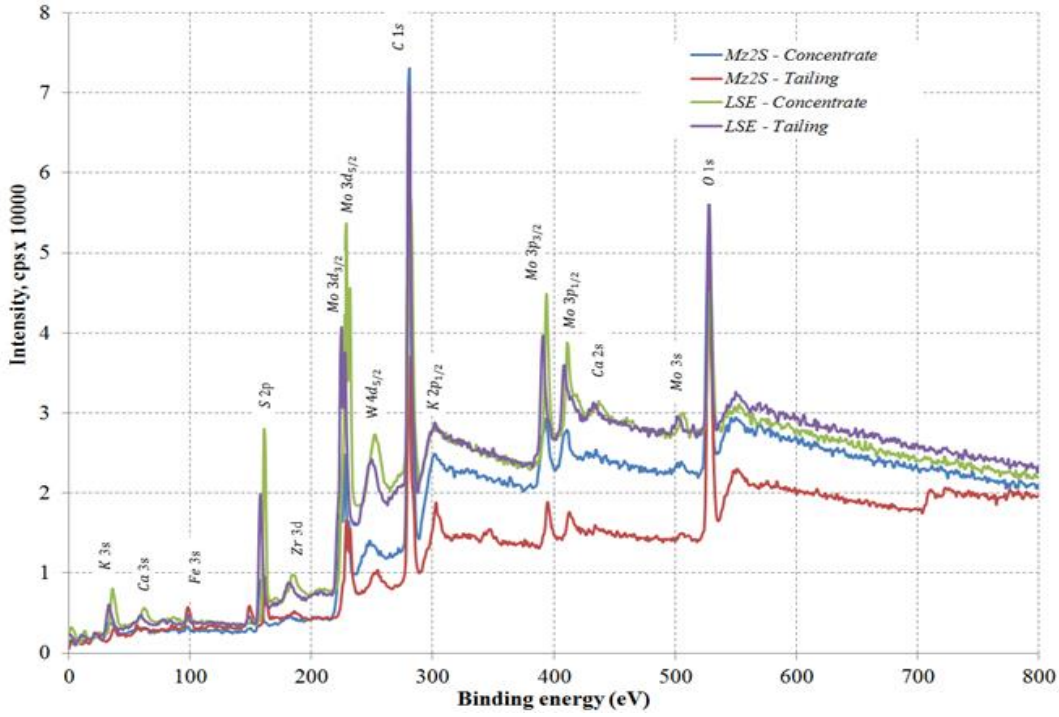

Figure 5.20 A survey (full range) XPS spectrum of molybdenite particles isolated from the MZ2S and LSE rougher concentrate and tailings.

a) LSE ore

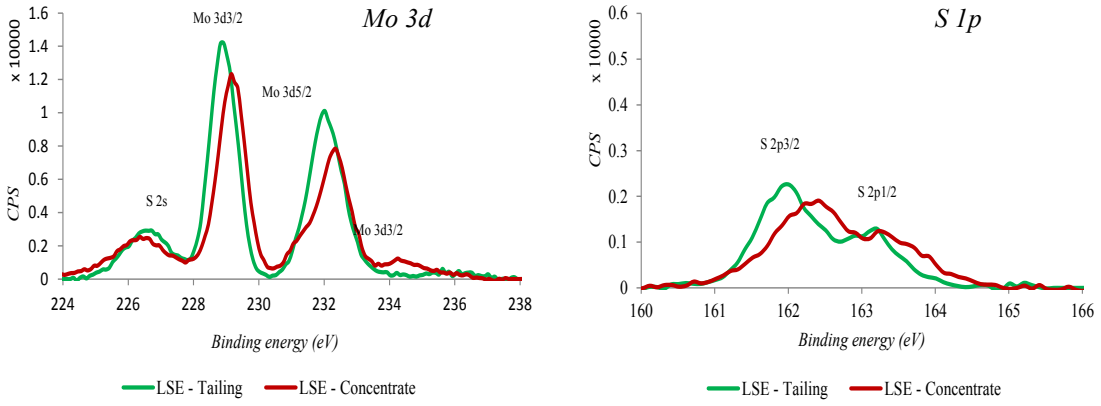

b) MZ2S ore

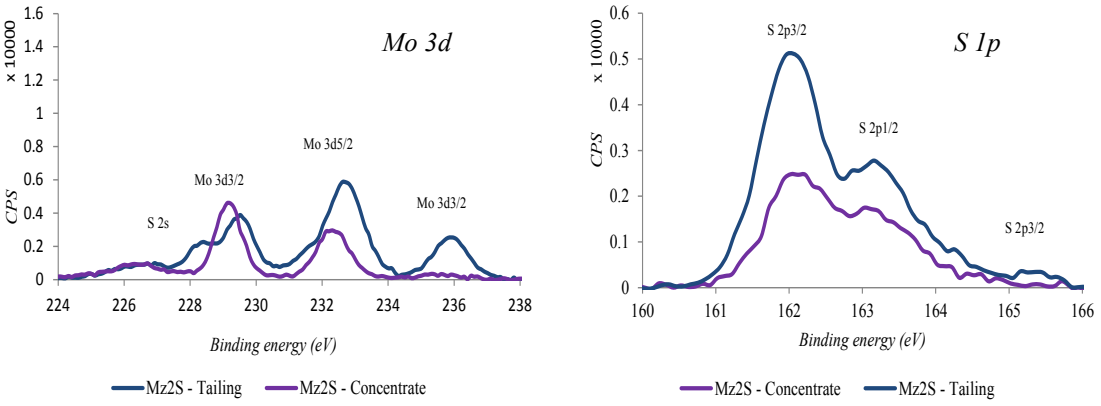

Figure 5.21 High resolution XPS spectra of Mo 3d and S 2s peaks and S 2p peaks, on the MoS_2 samples isolated from the LSE (a) and MZ2S (b) samples.

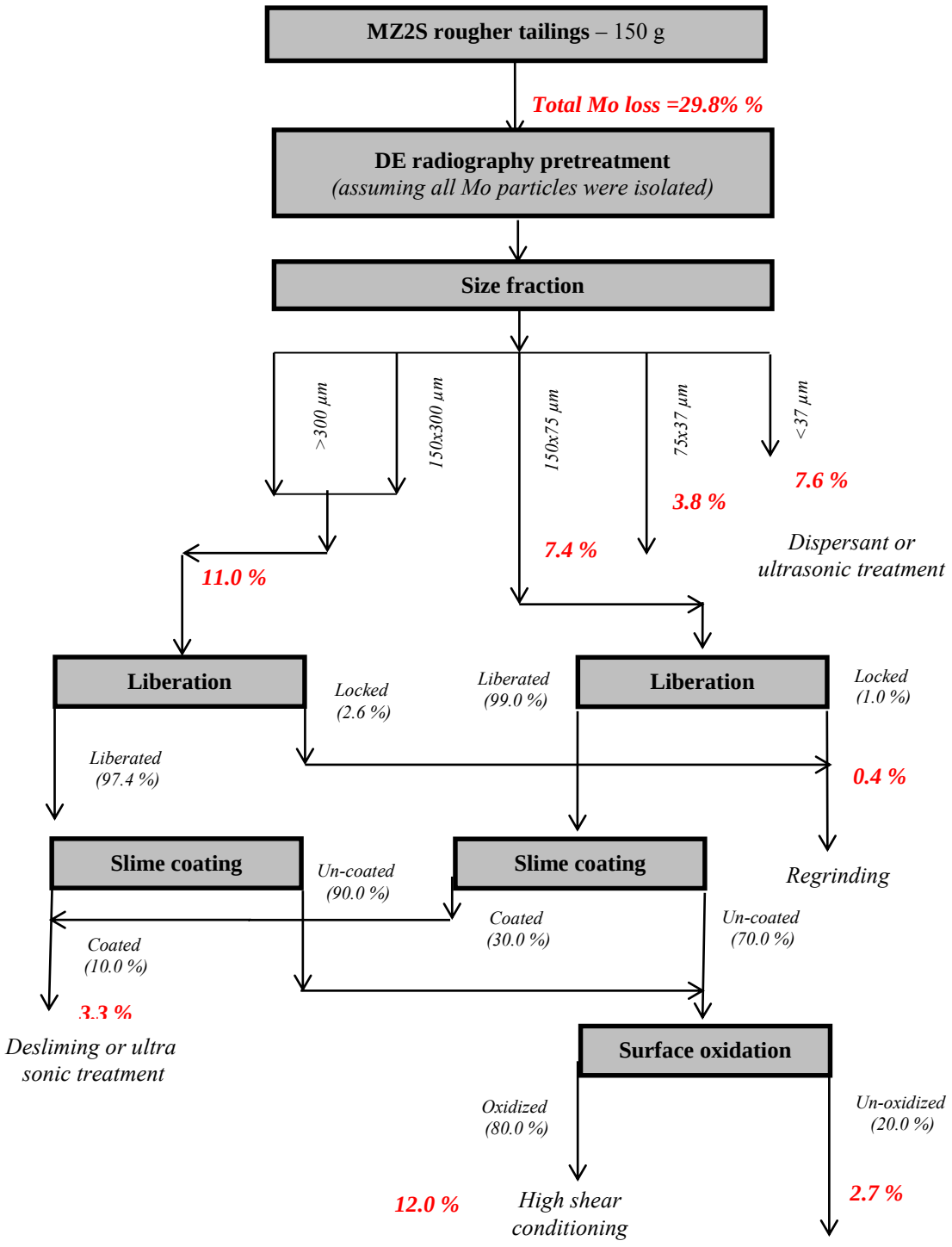

Figure 5.22 Summary of detailed characterization analysis of Mo loss in the MZ2S sample.

Table 5.1 Scan conditions for the MicroXCT-400 in the analysis of lost particles in KUC rougher tailings samples. Table made by following the scanning procedure of Lin and Miller, 1996

	Material		Rougher tailings
1	Objective		4X
2	Total Scan Time	hour	4
3	Source Settings (kV/W)	kV/Watts	80/10
4	Pixel size (m)	µm	4.59
5	Start and End Angle	degree	360
6	Number of Views		1000
7	Time per View (sec)	second	9
8	Source/Detector Positions	mm	-44/20
9	Camera Binning		2
10	Physical Filter(glass)	µm	150

Table 5.2 CT number distribution/frequency of each mineral phase.

	Name	Chemical formula	CT number	
			original	rescaled
1	Air		200	5
2	Silicate	SiO_2	2000	50
3	Pyrite	FeS_2	4400	110
4	Chalcopyrite	$CuFeS_2$	5040	126
5	Bornite	Cu_5FeS_4	7400	185
6	Molybdenite	MoS_2	9600	240

Table 5.3 Size-by-size chemical analysis for the MZ2HE rougher feed (fine grinding).

	Size class, µm	Weight		Assays, %		Distribution, %	
		gram	%	Cu	Mo	Cu	Mo
1	>300	7.9	5.2	0.06	0.010	0.6	1.1
2	300x150	36.6	24.4	0.26	0.039	11.8	20.3
3	150x75	38.0	25.3	0.83	0.052	39.4	28.1
4	75x37	35.3	23.6	0.98	0.086	43.4	43.2
5	<37	32.2	21.5	0.12	0.016	4.8	7.2
	Total	150.0	100.0	0.53	0.047	100.0	100.0

Table 5.4 Size-by-size chemical analysis for the MZ2HE rougher tailings (fine grinding).

	Size class, µm	Weight		Assays, %		Distribution, %	
		gram	%	Cu	Mo	Cu	Mo
1	>300	8.1	5.4	0.02	0.008	2.7	6.7
2	300x150	33.8	22.6	0.04	0.016	22.5	54.5
3	150x75	39.8	26.5	0.05	0.005	35.8	21.8
4	75x37	38.8	25.9	0.03	0.002	19.4	8.7
5	<37	29.4	19.6	0.04	0.003	19.6	8.3
	Total	150.0	100.0	0.04	0.007	100.0	100.0

Table 5.5 Size-by-size chemical analysis for the LSE rougher feed (fine grinding).

	Size class, µm	Weight		Assays, %		Distribution, %	
		gram	%	Cu	Mo	Cu	Mo
1	>300	2.0	1.3	0.67	0.056	1.1	1.7
2	300x150	21.9	14.6	0.47	0.048	8.6	16.2
3	150x75	40.3	26.9	1.10	0.052	35.5	32.6
4	75x37	47.0	31.3	1.09	0.048	43.1	34.8
5	<37	38.8	25.9	0.36	0.024	11.7	14.6
	Total	150.0	100.0	0.80	0.043	100.0	100.0

Table 5.6 Size-by-size chemical analysis for the LSE rougher tailings (fine grinding).

	Size class, µm	Weight		Assays, %		Distribution, %	
		gram	%	Cu	Mo	Cu	Mo
1	>300	1.6	1.0	0.28	0.039	3.3	5.6
2	300x150	17.0	11.4	0.15	0.028	19.6	43.1
3	150x75	43.0	28.7	0.06	0.003	20.4	9.9
4	75x37	48.1	32.1	0.06	0.001	22.8	5.7
5	<37	40.3	26.9	0.11	0.010	33.9	35.8
	Total	150.0	100.0	0.09	0.007	100.0	100.0

Table 5.7 Size-by-size chemical analysis for the MZ2S rougher feed (fine grinding).

	Size class, µm	Weight		Assays, %		Distribution, %	
		gram	%	Cu	Mo	Cu	Mo
1	>300	2.3	1.5	0.22	0.002	0.4	0.1
2	300x150	23.3	15.6	0.35	0.023	6.0	7.7
3	150x75	54.0	36.0	0.95	0.044	37.2	34.7
4	75x37	36.8	24.6	1.70	0.078	45.5	41.9
5	<37	33.6	22.4	0.45	0.032	11.0	15.7
	Total	150.0	100.0	0.92	0.046	100.0	100.0

Table 5.8 Size-by-size chemical analysis for the MZ2S rougher tailings (fine grinding).

	Size class, µm	Weight		Assays, %		Distribution, %	
		gram	%	Cu	Mo	Cu	Mo
1	>300	1.7	1.1	0.04	0.003	0.5	0.2
2	300x150	18.4	12.2	0.07	0.025	9.7	23.0
3	150x75	47.4	31.6	0.08	0.019	28.0	44.0
4	75x37	44.3	29.5	0.08	0.005	27.2	10.5
5	<37	38.3	25.5	0.12	0.012	34.5	22.3
	Total	150.0	100.0	0.09	0.014	100.0	100.0

Table 5.9 The qualitative summary results of liberation characteristics of molybdenite in the rougher tailings of the MZ2HE, LSE and MZ2S ore types.

Ore type	Grind condition	Size class, μm	Detected numbers of molybdenite	Liberation grade, %			
				0-30	30-50	50-90	90-100
MZ2HE	*25 % + 100 mesh*	300x150	8	2.0	-	12.7	85.3
		150x75	14	2.3	2.9	-	94.8
LSE		300x150	68	0.2	1.3	3.0	95.5
		150x75	114	0.9	1.5	3.0	94.6
MZ2S		300x150	121	-	2.6	4.1	93.2
		150x75	243	0.2	0.7	0.8	98.2

Table 5.10 The binding energy and FWHM values from standard samples of MoS_2 and MoO_3.

Product	Line	BE (eV)	FWHM (eV)
MoS_2	Mo $3d_{5/2}$	229.81	0.42
	Mo $3d_{3/2}$	232.94	0.63
	S 2s	226.99	1.87
	S $2p_{3/2}$	162.66	0.43
MoO_3	Mo $3d_{5/2}$	233.15	0.86
	Mo $3d_{3/2}$	236.28	0.9

Table 5.11 Atomic fractions, atomic ratios and the percentages of different Mo and S species with their corresponding totals, derived from the XPS spectra.

Component	LSE ore		MZ2S ore	
	Concentrate	Tailings	Concentrate	Tailings
Atomic fraction (%)				
O	56.4	62.5	42.9	73.5
S	24.5	21.0	29.9	18.9
Mo	13.5	11.7	16.4	12.3
Mo^{4+}	13.0	9.9	14.3	5.2
Mo^{6+}	0.5	1.8	2.1	7.1
Atomic ratio				
S/Mo	1.81	1.80	1.82	1.53
O/S	2.3	3.0	1.4	3.9
O/Mo	4.2	5.4	2.6	6.0

Here $S = S^{2-} + S^{6+}$, *and* $Mo = Mo^{4+} + Mo^{6+}$, *respectively*

CHAPTER 6

CONCLUSIONS

Although mineral resources are nonrenewable, they are indispensable materials for the development and survival of human societies. The characterization of mineral resources is a critical component for optimization of the mine-to-mill process, and now can be accomplished with advanced instrumentation. Each ore body is unique, and has to be treated as such. The development of advanced characterization technology in recent years has had direct bearing on the automated analysis systems now available that can make mineral characterization faster and more accurate. The variability of the feed quality delivered to flotation plants in mining operations can present challenges to the operational staff in attempting to achieve satisfactory recovery and grade efficiency. When faced with variables or difficult ores, plant operators are often required to implement operational parameter changes to maintain flotation efficiency.

The goal of this research was to improve the understanding of the variables or factors affecting the flotation efficiency of copper and molybdenum minerals from porphyry copper ores and to provide some possible solutions to these challenges. Specifically, the identification and characterization of lost mineral particles using a rapid scan DE radiography method for the analysis of flotation products was considered to investigate

the significance of these problems associated with the flotation efficiency of selected KUC ore types. According to flotation testing, the Cu and Mo recoveries of some ore types such as the LSE and MZ2S ore types are far inferior to the more traditional, well-behaved ore types at the Copperton concentrator, KUC. Significant amounts of Cu and Mo minerals in these ore types are lost to tailings streams due to many variables that influence the flotation process and affect the process of mineralization of air bubbles. These lost trace minerals, mostly unliberated and entrapped in gangue minerals, are present as fine slimes, or report to tailings due to problems in process operations during flotation. Tailings evaluation is an area where it is possible to define the actual losses in a mineral processing plant. However, because of the trace concentrations of these trace minerals, sample collection and integrity become one of the major concerns in any project relating to tailings characterization analysis. For a trace mineral such as molybdenite, the content in the flotation products is in the range of parts per million (ppm), which means that several millions of particles must be examined to provide statistical reliabillity, accuracy and confidence in the advanced characterization analysis. Of course, working with such products is never easy. The process of selecting and preparing an appropriate, representative sample can be more work than undertaking the direct characterization analysis.

This research primarily focused on a new radiographic inspection method and especially the characterization and isolation of lost trace minerals based on measured X-ray intensities in a relative reflex and the effective atomic number. In particular, an HRXMT-based technique was developed in order to characterize the lost trace mineral particles in flotation tailings and/or any other particulate materials. Although the atomic

number is well defined for chemical elements, the definition of an atomic number for any compound is not an easy task. After reviewing the different definition methods available in the literature, a definition related to the method of X-ray relative reflex measurement was suggested. For help in determining the relative reflex and the effective atomic number of unknown minerals, a new concept of mineral identification was introduced in real flotation practice and advanced mineral characterization analysis. Finally, this research suggested implementing the accurate, rapid and reliable DE radiographic inspection method for the isolation of trace mineral particles in flotation products using an X-ray system. Also, DE radiography inspection is beneficial for characterizing lost trace mineral particles, and improving data accuracy and reliability of advanced instrumentation. This especially could reduce sampling errors, experimental cost and experimental lead time in the plant. As described by Gy (1979), "the failure of mining or metallurgical undertakings can nearly always be attributed to unaccountable sampling errors." This could help researchers to better understand the general characteristics of lost minerals such as their liberation/exposure state, surface chemistry issues, effect on the flotation environment and to better control their flotation efficiency. It is expected that in the near future, DE radiography will be used more and more as a routine research or sample preparation tool and be successfully integrated with other analytical instruments in various geological, mining and metallurgical disciplines. In this regard, all objectives of this research have been achieved.

Tailings from three ore types (LSE, MZ2S and MZ2HE) were characterized in detail using DE radiography to isolate lost particles. Characterization of the lost particles according to size was accomplished using optical microscopy, SEM-EDS, XPS and

HRXMT and the results used to explain flotation recovery. It was found that copper losses for each ore type were due to lack of sufficient liberation. Such was not the case with respect to molybdenum losses. Molybdenum losses for the LSE ore type were found to be primarily due to slime coating and particle size, whereas molybdenum losses for the MZ2S ore type were found to be primarily due to surface oxidation and variation in process water chemistry.

APPENDIX A

RESULTS OF FLOTATION TESTING

Table A.1. A summary of the test objectives, conditions and notable results for the rougher kinetic tests.

Test # / Conditions	Product	Weight, %	Grade, %			Recovery, %		
			Cu	Mo	Fe	Cu	Mo	Fe
T1a – LSE 25 % + 100 mesh P80 = 168 microns	Ro conc - 1	2.32	31.11	1.25	28.7	72.3	65.0	5.8
	Ro conc - 2	0.58	18.92	0.80	20.8	11.3	10.8	1.1
	Ro conc - 3	0.27	9.68	0.49	15.7	2.5	2.9	0.4
	Ro conc - 4	0.45	6.57	0.46	14.2	2.9	4.6	0.6
	Ro tail	96.38	0.11	0.008	10.9	10.9	16.8	92.2
	Head calc.	100.00	1.00	0.045	11.5	100.0	100.0	100.0
T2a – LSE 35 % + 100 mesh P80 = 220 microns	Ro conc - 1	1.85	29.7	1.30	27.7	51.9	49.5	4.3
	Ro conc - 2	0.75	22.5	0.79	23.7	15.4	11.9	1.4
	Ro conc - 3	0.33	14.4	0.59	18.5	4.6	4.1	0.5
	Ro conc - 4	0.67	12.8	0.63	18.5	8.6	9.2	1.1
	Ro tail	96.40	0.22	0.012	11.2	19.6	25.3	92.6
	Head calc.	100.00	1.043	0.048	11.7	100.0	100.0	100.0
T3a – MZ2S 25 % + 100 mesh P80 = 146 microns	Ro conc - 1	2.28	30.5	0.78	23.9	63.6	30.2	32.5
	Ro conc - 2	0.87	22.4	1.35	18.0	18.0	20.1	9.4
	Ro conc - 3	0.42	11.9	0.93	13.6	4.5	6.6	3.4
	Ro conc - 4	0.86	5.36	0.90	7.51	4.2	13.2	3.9
	Ro tail	95.58	0.11	0.0	0.89	9.7	29.9	50.8
	Head calc.	100.00	1.089	0.059	1.67	100.0	100.0	100.0
T4a – MZ2S 35 % + 100 mesh P80 = 205 microns	Ro conc - 1	2.12	27.60	1.17	22.78	52.9	41.5	27.9
	Ro conc - 2	1.08	22.11	1.22	18.54	23.3	23.8	12.5
	Ro conc - 3	0.41	14.89	0.98	11.80	5.8	7.1	2.9
	Ro conc - 4	0.89	7.76	0.50	7.24	6.3	7.6	3.7
	Ro tail	95.50	0.13	0.01	0.92	11.7	20.0	53.0
	Head calc.	100.00	1.06	0.057	1.65	100.0	100.0	100.0
T5a – MZ2HE 25 % + 100 mesh P80 = 120 microns	Ro conc - 1	2.28	18.5	1.53	18.8	65.9	62.8	15.1
	Ro conc - 2	1.27	11.2	0.84	13.2	21.6	18.7	5.7
	Ro conc - 3	0.58	3.98	0.29	7.20	3.7	3.1	1.5
	Ro conc - 4	0.82	1.28	0.11	4.26	1.7	1.6	1.3
	Ro tail	95.05	0.05	0.01	2.16	7.2	13.7	76.4
	Head calc.	100.00	0.607	0.053	2.69	100.0	100.0	100.0

Table A.1 continued

T6a – MZ2HE 35 % + 100 mesh P80 = 180 microns	Ro conc - 1	2.13	17.3	1.56	18.8	58.0	63.1	14.6
	Ro conc - 2	1.03	11.9	0.86	13.0	19.2	16.7	4.9
	Ro conc - 3	0.40	5.68	0.38	8.27	3.5	2.9	1.2
	Ro conc - 4	0.65	2.11	0.14	5.11	2.2	1.7	1.2
	Ro tail	95.80	0.11	0.01	2.24	17.1	15.5	78.2
	Head calc.	100.00	0.636	0.053	2.75	100.0	100.0	100.0

Table A.2. A summary of results for the scavenger flotation after desliming.

Test#/ Conditions	Product	Weight, %	Grade, %			Recovery, %		
			Cu	Mo	Fe	Cu	Mo	Fe
T1b – LSE Fine grind	Scav. conc	0.92	2.60	0.164	28.99	21.73	25.09	2.53
	Scav. tail	68.06	0.05	0.003	11.36	32.87	35.99	73.52
	Slime	26.85	0.19	0.009	9.38	45.40	38.91	23.94
	Rougher tail.	95.83	0.11	0.006	10.98	100.00	100.00	100.00
T2b – LSE Coarse grind	Scav. conc	0.81	2.19	0.110	14.56	9.72	9.40	1.00
	Scav. tail	75.48	0.17	0.009	13.01	70.95	72.61	83.38
	Slime	19.60	0.18	0.009	9.39	19.33	17.99	15.62
	Rougher tail.	95.89	0.19	0.010	12.28	100.00	100.00	100.00
T3b – MZ2S Fine grind	Scav. conc	1.12	1.74	0.142	3.20	18.26	12.45	3.48
	Scav. tail	68.95	0.08	0.012	0.93	50.27	64.72	62.58
	Slime	25.51	0.13	0.011	1.37	31.47	22.83	33.94
	Rougher tail.	95.58	0.10	0.019	0.89	100.00	100.00	100.00
T4b – MZ2S Coarse grind	Scav. conc	0.96	1.08	0.110	7.11	8.35	10.10	7.76
	Scav. tail	73.02	0.12	0.008	0.70	71.39	55.98	57.92
	Slime	21.87	0.12	0.016	1.38	20.26	33.92	34.32
	Rougher tail.	95.85	0.129	0.011	0.92	100.00	100.00	100.00
T7b – MZ2HE Fine grind	Scav. conc	0.91	1.46	0.17	5.23	30.48	21.05	2.31
	Scav. tail	75.18	0.03	0.011	2.10	51.56	70.06	76.55
	Slime	19.62	0.04	0.003	2.22	17.96	8.89	21.14
	Rougher tail.	95.710	0.05	0.008	2.15	100.00	100.00	100.00
T8b – MZ2HE Coarse grind	Scav. conc	1.25	1.11	0.168	6.12	12.33	22.99	3.03
	Scav. tail	76.48	0.12	0.007	2.72	78.76	61.96	82.57
	Slime	17.62	0.06	0.008	2.10	8.91	15.05	14.39
	Rougher tail.	95.35	0.12	0.010	2.64	100.00	100.00	100.00

APPENDIX B

RAPID SCAN RADIOGRAPHY SCANNING PROCEDURE

Sample preparation

Plastic plates (76.2x25.4x1.0 mm) and double-sided sticky tape were used to prepare the sample for DE radiography scans. First, narrowly sized particles were spread on the flat surface. Then, the plastic plate with double-side sticky tape on its surface was tapped on the particle bed. Finally, a single layer of particles was stabilized with the second plastic plate.

Scanning operating procedures

The XRadia Micro XCT-400 is the main operating device of the experiments in rapid scan radiography. Standard operating procedure will be discussed step-by-step in order to convey a general idea of the HRXMT scan operation:

- Click the Start button and open XMController 7.0.2817
- Go to the X-RAY SOURCE DIALOG box as shown in Figure B.1 and click ON. The red light on the top of the machine will turn on while the X-ray source is powered. Voltage and power can be adjusted. In this study, high- (140 kV) and low- (80 kV)

energy level will be used for dual energy radiography with 10 W power. Clicking ON or APPLY will switch the machine to Standby mode (fully warmed up) or Warming up mode. The warming up process will take 15 minutes.

- During the warming up process, the sample material is being prepared and fastened onto the sample holder and also check the filter in the filter holder. In this case, we used a 150 μm glass filter for reducing a specific element effect.
- The red light on the top of the machine will shut off after the machine is fully warmed up. Open the chamber and put the sample with the holder on the stage. Close the chamber and check if the green light is on.
- Check and adjust the MAGNIFICATION LEVEL; it should be 4X, as shown in Figure B.2.
- Go to the X-RAY SOURCE DIALOG box and click on the X-Ray On button again. This time the machine reaches a specific power level in only a few seconds after being fully warmed up. Set up voltage and power to first selected level (voltage - 140 kV and power - 10W) and click APPLY. The machine will raise the energy the selected level in a few seconds. When the power is raised to the selected level, turn on the internal light and the surveillance camera.
- Open the MOTION CONTROLLER window, as shown in Figure B.3; adjust distances of source and detector. In this case, the scan conditions are set at 4X magnification with 5 second exposure time; source voltage is set at 140kV; distance between source and detector is -44 mm and 20mm; camera binning is set at 2 with a 150 μm glass filter.
- Go to the ACQUISITION SETTING dialog box and select Continuous Scan with 1

second exposure time, binning 4, as shown in Figure B.4. Keep the rest of the settings unchanged and press the START ACQUISITION button. This step will acquire an initial position of projections for field of view calibration. The sample image will be acquired and refreshed every second (depending on the exposure time). Binning 4 helps to reduce the file size and the image acquisition time, however, it loses the pixel resolution and increases X-ray intensity on the detector.

- Go to the MOTION CONTROLLER window and select SAMPLE section. The sample itself can move on the x axis (from door side to inner side), y axis (sample raises or descent) in micron precision. Find the pinhole, which is on the sample slide and click on the center of pinhole.
- Go to VIEW and click Highlight Center of FOV; a central cross line will show up and indicate the center of the pinhole image. Move the field of view from pinhole to the region of interest (initial position of first radiography image) by double clicking the left mouse key on the acquired image shown in Figure B.3. Make sure the region of interest is covered by the sample as much as possible on field of view. The field of view will be reallocated to a new central point on which the cursor clicks. The field of view can be also adjusted by pushing forward or pulling back the joystick on the control panel. If the field of view is well calibrated, then press STOP in the icon bar. Then write down an initial coordinate in the MOTION CONTROLLER on your student note or blank sheet.
- Go to the ACQUISITION SETTING dialog box again and select the AVERAGING mode this time. Image noise can compromise the level of detail in the radiography images, so reducing this noise can greatly enhance our final image. The exposure

time is set at 5 seconds according to the applied CT standard for the scan. The binning is set at 2 for a regular scan. Keep the rest of the settings unchanged and press the START ACQUISITION button. This step will provide a single radiographic image.

- If the image quality and scan conditions are satisfactory for the scan requirements, the SAVE AS window will automatically open after pressing the START ACQUISITION, save this image and name the image:

  LSE_fine_p100_slide_1_N1_Se1x1_HE.xrm.

- The naming rule, here is followed by Ore type, Grind condition, Slide #, Test #, Section #, and Energy level. Click the SAVE button to start the scan.
- The scanning process will take 25 - 40 seconds depending on averaging numbers (3-5 images).
- Go to the X-Ray Source dialog box again and set up voltage to second selected level (voltage - 80 kV and power – 10W). This time the machine reaches a specific power level in only a few seconds. Wait 60 seconds for stabilizing energy output in the machine.
- Go to the ACQUISITION SETTING dialog box and select AVERAGING again. Keep the rest of the settings unchanged except voltage and press START ACQUISITION. The scanning process will also take 25 - 40 seconds, same as the previous scan.
- If the image quality and scan conditions are satisfactory, save this image and name it LSE_fine_p100_slide_1_N1_Se1x1_LE.xrm. Now we have two images with the same coordinate and same scan conditions, both a high- (140 kV) and a low- (80 kV)

energy level.

- After the scanning process at high- and low-energy levels establish averaged references (Figure B.5.). It should be prepared on both high- and low- energy level.
- Go to the Image controls window and click the REFERENCE button and then choose the BROWSE section. The OPEN FILE window will be automatically opened after choosing BROWSE section. To apply the reference with the same scan condition to interest of point (radiographic image).
- After applying reference into interest of point, go to File and click on Export and it will then open the SAVE FILE window. We need to convert file type from *.xrm to *.bin, as shown in Figure B.6 for image data analysis.

Reference preparation

Because the environment for the HRXMT scan is neither in a vacuum nor isolated, reference states are measured to remove X-ray attenuation of background, air and other effects associated with the lens like dirty spots and dust. The reference can be shot before or after the scan following the same scan condition. Each sample (slide) should have their own references both on high- and low-energy level; save them on the same folder with sample scans. Reference preparation procedure will be discussed step-by-step in order to convey a scan operation:

- Go to the X-RAY SOURCE DIALOG box and click on the X-Ray Off button if the X-ray source did not turn off. Then, the orange light on the top of the machine will turn off;
- Remove a sample with holder from stage;

- Go to the X-RAY SOURCE DIALOG box and click on the X-Ray On button, again. The orange light on the top of the machine will turn on. Make sure the scan conditions are set the same as high-energy level at 4X magnification with 5 second exposure time; source voltage is set at 140kV; distance between source and detector are -44 mm and 20mm; camera binning is set at 2 with a 150 μm glass filter and click APPLY. This time the machine reaches a specific power level in only a few seconds;
- Go to the ACQUISITION SETTING dialog box and select AVERAGING. Then press the START ACQUISITION button and save this reference and name it:

  LSE_fine_p100_slide_1_N1_ reference_140kV.xrm;

- Repeat steps 1-5 for the second reference for low-energy level but remember to change voltage to 80 kV and keep the rest of the settings unchanged;
- Save this reference and name the image:

  LSE_fine_p100_slide_1_N1_reference_ 80kV.xrm.

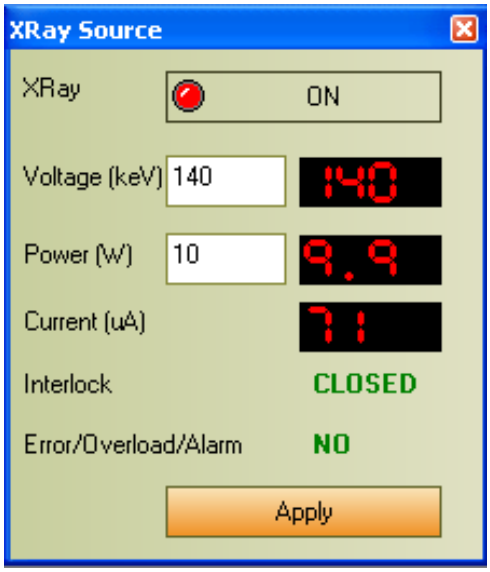

Figure B.1 The X-Ray source dialog icon.

Figure B.2 The magnification icon in the XMController.

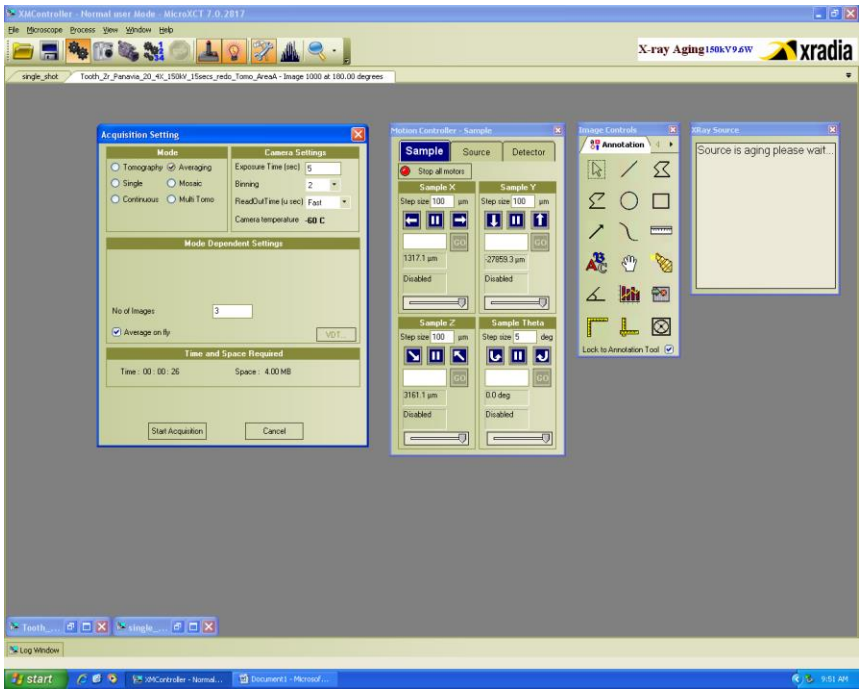

Figure B.3 The acquisition setting, motion control, image control window.

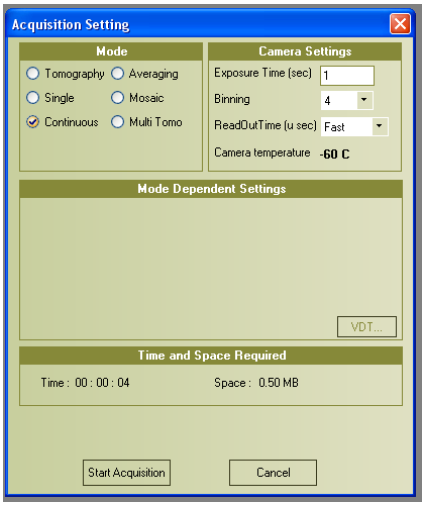

Figure B.4 The acquisition control setting in the continuous mode.

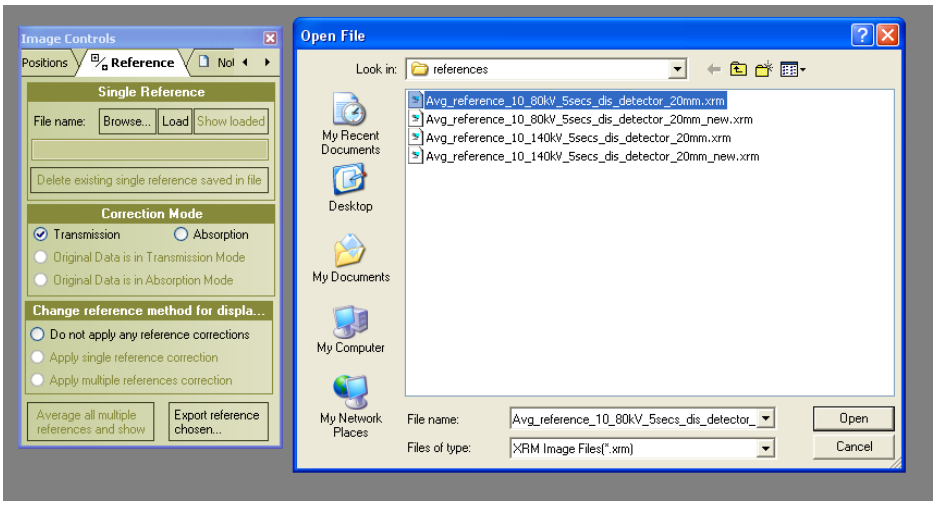

Figure B.5 Image control setting.

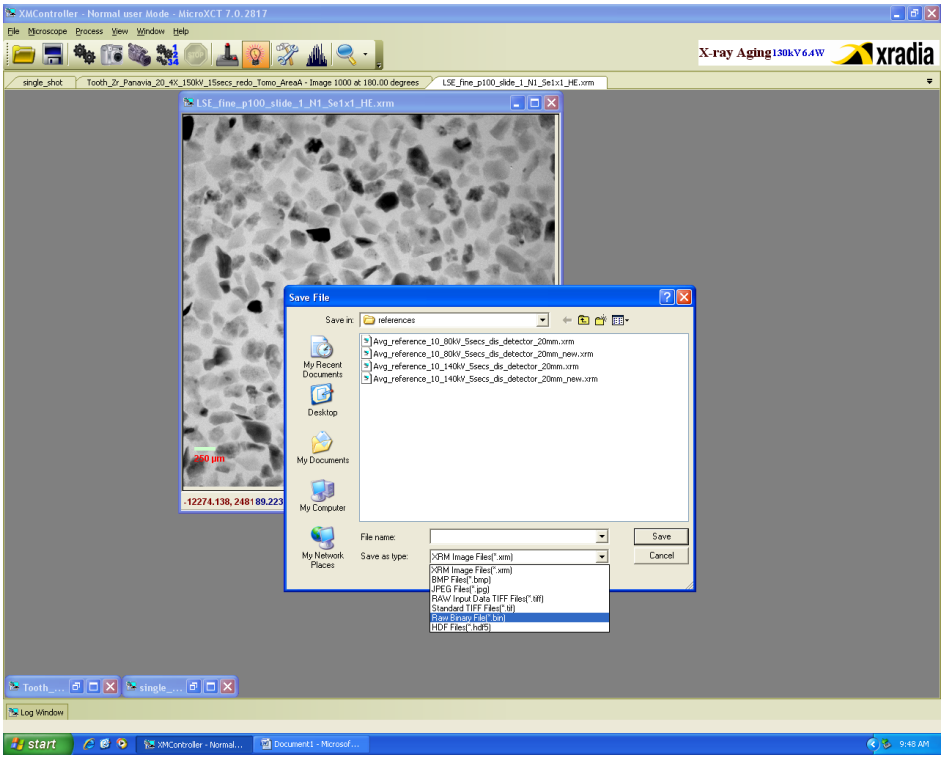

Figure B.6 Reference applying method.

APPENDIX C

MATHLAB CODE - RAPID SCAN RADIOGRAPHY

```
clear; clc; close all; Size = 1014; p=3.8;
%% HE
                fid = fopen('../../Zeff on standard/Mo_Pb_Cu_Al_Si_Au
                standard_HER.bin','rb');
                HER = fread(fid, Size * Size,'float32'); fclose(fid);
                 fid = fopen('../../Zeff on standard/Mo_Pb_Cu_Al_Si_Au
                standard_HE.bin','rb');
                HE = fread(fid, Size * Size,'float32'); fclose(fid);
HE = reshape(log(HER./HE), Size, Size);
                PbH=HE(700:760,600:660); mPbH=mean(PbH(:));
                 CuH=HE(650:710,350:410); mCuH=mean(CuH(:));
                 AlH=HE(390:440,260:440); mAlH=mean(AlH(:));
%% LE
                fid = fopen('../../Zeff on standard/Mo_Pb_Cu_Al_Si_Au
                standard_LER.bin','rb'); LER = fread(fid, Size * Size,'float32'); fclose(fid);
                 fid = fopen('../../Zeff on standard/Mo_Pb_Cu_Al_Si_Au
```

```
standard_LE.bin','rb'); LE = fread(fid, Size * Size,'float32'); fclose(fid);
LE = reshape(log(LER./LE), Size, Size);
PbL=LE(720:780,600:640); mPbL=mean(PbL(:));
CuL=LE(650:730,350:440); mCuL=mean(CuL(:));
AlL=LE(360:430,260:440); mAlL=mean(AlL(:));
%% Determination of relative reflexes =(X1, X2, X3) of standart samples
X1=mPbL/mPbH
X2=mCuL/mCuH
X3=mAlL/mAlH
%% Determination of coefficients ( k1, k2, k3, k4) of Equation # 15
Z1=82^p;  Z2=29^p;  Z3=13^p;
k1=Z1*Z2*(X1-X2)-Z1*Z3*(X1-X3)+Z2*Z3*(X2-X3)
k2=X1*X2*Z3*(Z1-Z3)-X1*X3*Z2*(Z1-Z3)+X2*X3*Z1*(Z2-Z3)
k3=X1*(Z2-Z3)-X2*(Z1-Z3)+X3*(Z1-Z2)
k4=X1*X2*(Z1-Z2)-X1*X3*(Z1-Z3)+X2*X3*(Z2-Z3)
%% Isolation and identification of unknown minerals based on the relative reflex (Zeff
sample)

for i=1:1
   for j=1:1
name=sprintf('LSE_fine_p100_slide_1_N1_Se%ix%i_HE.bin', i, j);
fid=fopen(name,'rb');
HE=fread(fid, Size * Size,'float32');
fclose(fid);
```

```
                name=sprintf('LSE_fine_p100_slide_1_N1_Se%ix%i_LE.bin', i, j);
                 fid=fopen(name,'rb');
                 LE=fread(fid, Size * Size,'float32');
                 fclose(fid);
X=(LE)./(HE);
Zeff=((k1*X+k2)./(k3*X+k4)).^(1/p);
                Zeff = reshape(Zeff, Size, Size);
                figure,imshow(Zeff,[0,50]);colormap(lines);
                 name=sprintf('Zeff_%ix%i.bin',i,j);
                fid=fopen(name,'wb');
                fwrite(fid,Zeff,'float32');
                fclose(fid);
                disp([num2str(i),'',num2str(j)])
  end
end
```

REFERENCES

Alvarez, R.E., and Macovski, A. 1976. Energy selective reconstructions in X-ray computerized tomography. *Phys. Med. Biol.* 21: 733-744.

Alvarez, R.E., Seibert, J.A., and Thompson, S.K. 2004. Comparison of dual energy detector system performance. *Med Phys.* 3: 56-65.

Ametov, I., Grano, S.R., Zanin, M., Gredelj, S., Magnuson, R., Bolles, T., Triffett, B., Zuo, W.D., Yao, S.C., Liang, W.F., Cheng, Z.L., and Long, H. 2008. Copper and molybdenite recovery in plant and batch laboratory cells in porphyry copper rougher flotation. *Proceedings of XXIV IMPC,* Beijing, China. 1: 1129–1137.

Arnold, B.J., and Aplan, F.F. 1986. The effect of clay slimes on coal flotation, part ii: the role of water quality. *Int. J. Miner. Process.* 17 (3–4): 243–260.

Babcock, R.C., Ballantyne, G., and Phillips, C. 1997. Summary of the geology of the Bingham District, Utah. Geology and ore deposits of the Oquirrh and Wasatch mountains. *Utah Society of Economic Geologists*.

Barzyk, W., Malysa, K., and Pomianowski, A. 1981. The influence of surface oxidation of chalcocite on its floatability and ethyl xanthate sorption. *Int. J. Miner. Process.* 8 (1): 27–29.

Basilio, C.I., Kartio, I.J., and Roon, R.H. 1996. Lead activation of sphalerite during galena flotation. *Miner. Eng.* 9: 869–879.

Bradshaw, D.J., Triffett, B., and Kashuba, D. 2011. The role of process mineralogy in identifying the cause of the low recovery of chalcopyrite at KUC. *Proceedings of X ICAM.* Trondheim, Norway, 73-80.

Briggs, D., and Seah, M.P. 1990. *Practical Surface Analysis: Auger and X-ray photoelectron spectroscopy*. John Wiley & Sons.

Brody, W.R., Butt G., Hall A., and Macovski, A.A. 1981. Method for selective tissue and bone visualization using dual-energy scanned projection radiography. *Med. Phys.* 8 (3): 353–357.

Broman, P.G. 1980. Water reuse at sulfide ore concentrators in Sweden: practice, experience and current development. Jones, M.J. Ed. Complex Sulphide Ores. *The Institution of Mining and Metallurgy,* London. 28–39.

Brown, A.M. 2001. Step-by-step guides to nonlinear regression analysis of experimental data using a Microsoft excel spreadsheet. *Computer Methods Programs in Biomedicine*. 65: 191-200.

Brozek, M., and Mlynarczykowska, A. 2006. Analysis of kinetics models of batch flotation. *Physicochemical Problems of Mineral Processing*. 41: 51–65.

Bulatovic, M. 2007. *Handbook of flotation reagents: chemistry, theory and practice: Flotation of sulphides ores*. Elsevier Scientific Pub. Co.

Bulled, D., and McInnes, C. 2005, Flotation plant design and production planning through geometallurgical modeling. *Centenary of Flotation Symposium,* Brisbane, QLD. 6-9.

Canepa, C., and Bernuy, O. 1981. Mineral beneficiation and ore microscopy, some relevant methodological aspects. *Proceedings of Process Mineralogy, The Metallurgical Soc. of AIME*. 191-200.

Cardinal, H.N., and Fenster, A. 1990. An accurate method for direct dual energy calibration and decomposition. *Med. Phys.* 17: 327.

Castro, S., Venegas, I., Landero, A., and Laskowski, J. 2010. Frothing in seawater flotation systems. *Proceedings of XXV IMPC 2010,* Brisbane, Australia. 4039–4047.

Celik, M.S. 1988. Effect of ultrasonic treatment on the floatability of coal and galena, *J. Sep. Science and Technology*. 24 (14): 1159-1166.

Chander, S. 1999. *Fundamentals of sulfide mineral flotation, in advances in flotation technology*. Parekh . B.K., and Miller J.D, Ed. *Society of Mining, Metallurgy and Exploration, Inc*., Littleton, Colorado, 129-165.

Chander, S., and Fuerstenau, D.W. 1974. The effect of potassium diethyldithiophoshate on the interfacial properties of molybdenite. *Trans. Inst. Min. Met*. 83: C180-C185

Changlian. X.1985. Kinetic models for batch and continuous flotation in a flotation column. *Proceedings of XV IMPC*, Cannes, 3: 16-27.

Coleman, R.G., Urtubia, H.E., Alexander, D.J., and Bailey, C.W. 2007. Integrated grinding and flotation simulations for the improvement of circuit performance at BHB-Billiton's Minera Escondida. *Proceedings of XXXIX Annual Canadian Mill*

Operators Conference, Ottawa, Canada.

Crozier, R.D. 1979. Flotation reagent practice in primary and by-product molybdenite recovery. *Mining Magazine*. 140: 174-178.

Crozier, R.D. 1992, *Flotation, theory, reagents and ore testing*. Permagon Press.

Das, A.S., Ratnakar Sahu, K.K., and Goswami, N.G. 2008. Importance of mineralogy in mineral processing. *Training course on mineral processing and nonferrous extractive metallurgy.* Jamshedpur, India.

Davy, P.J. 1984. Probability models for liberation. *Journal of Applied Probability*. 21(2): 260-269.

Favretto, S. 2009. *Applications of X-ray computed micro tomography to material science, devices and perspectives*. PhD dissertation, Universita of Degli Studi de Trieste.

FLSmidth Technical Report. 2012. Rio Tinto – Kennecott Utah Copper. Cornerstone project. Results of phase I flotation variability testing on the Bingham pit south pushback expansion including 32 core samples and 6 surface composite samples.

Forssberg, K.S.E., Jönsson, H.R., and Pualsson, B.I. 1985. Full scale test of process water reuse in a complex sulphide ore circuit. Forssberg, K.S.E. Ed. *Flotation of Sulphide Minerals.* Elsevier Scientific Pub. Co, Amsterdam, Netherlands. 197-217.

Fuerstenau, D.W. 2005, A century of developments in the chemistry of flotation processing. *Centenary of Flotation Symposium*. Brisbane, Australia. 245-301.

Fuerstenau, D.W. 2007. A century of developments in the chemistry of flotation processing. *Froth Flotation: A Century of Innovation*, SME, Denver, USA. 1–13.

Fuerstenau, D.W., and Chander, S. 1972. On the natural floatability of molybdenite. *Transactions SME*. 255 (1): 62-69.

Fuerstenau, D.W., and Herrera-Urbina, R. 1989. *Mineral separation by flotation: Surfactant based separation process*. Edited by Scamehorn J.F. and Harwell, J.H., New York, Marcel Dekker.

Fuerstenau, M.C. 1982. Sulphide mineral flotation, in principles of flotation. R.P. King, Ed. *Proceedings of SAIMM*, Johannesburg. 159-182.

Fuerstenau, M.C. 2003. *Principles of mineral processing*. SME Publications.

Fuerstenau, M.C., Miller, J.D., and Kuhn, M.C. 1985. Chemistry of flotation. *Society of mining, Metallurgy and Exploration, Inc*. Littleton, Colorado, 74-78.

Fullston, D., Fornasiero, D., and Ralston, J. 1999. Zeta potential study of the oxidation of copper sulfide minerals, physicochemical and engineering aspects. *Colloids and Surfaces*. 146-113.

Garcia, D., Lin, C.L., and Miller, J.D. 2009. Quantitative analysis of grain boundary fracture in the breakage of single multiphase particles using X-ray microtomography procedures. *Miner. Eng.* 22: 236.

Gauntt, D.M., and Barnes, G.T. 1994. X-ray tube potential, filtration, and detector considerations in dual-energy chest radiography. *Med. Phys.* 21, 203–218.

Gay, S.L., and Latti, A.D. 2006. Representation of particle multi-mineral distributions. *Proceedings of XXII IMPC*. Istanbul, Turkey.

Gerson, A.R., Smart, R.S.C., Li, J., Kawashima, N., Weedon, Triffett, D., and Bradshaw, D. 2012. Diagnosis of the surface chemical influences on flotation performance: copper sulfides and molybdenite. *Int. J. Miner. Process.* 106–109, 16–30.

Goodall, W.R., Scales, P.S., and Butcher, A.R. 2005. The use of QEMSCAN and diagnostic leaching in the characterization of visible gold in complex ores. *Miner. Eng.* 18: 877-886.

Grano, S., Zanin, M., and Ametov, I. 2009. A study of mechanisms affecting molybdenite recovery in a bulk copper-molybdenum flotation circuit. *Int. J. Miner. Process.* 93: 256-266.

Greet, C., and Smart, R.St.C. 1996. The effect of size separation by cyclosizing and sedimentation on mineral surfaces. *Miner Eng*, in press.

Gribble, C.D., and Hall, A.J. 1992. *Optical mineralogy, principles and practice*. UCL Press. London.

Gu, Y. 2003. Automated scanning electron microscope based mineral liberation analysis an introduction to JKMR/FEI mineral liberation analyzer. *J. Minerals and Materials Characterization and Engineering*, 2 (1): 33 - 41.

Gu,Y., and Napier-Munn, T. 1997. JK/Philips mineral liberation analyzer – an introduction. *In Minerals Processing '97 Conf.* Cape Town, SA.

Guy, P.J., and Trahar, W.J. 1984. The influence of grinding and flotation environments on the laboratory batch flotation of galena. *Int. J. Miner. Process.* 12: 15.

Gy, P.M. 1979. *Sampling of particulate materials: theory and practice*. Elsevier Scientific Pub. Co.

Harris, C.C. 1976. *Flotation machines*, in Flotation, A.M. Gaudin Memorial, Fuerstenau

M.C. Ed. *Proceedings of AIME*. New York, 753-815.

Heaven, T.J., Sharon L., White, David, M., Gauntt, Richard, A., Weems., Mark, S., and Litaker. 2010. Density measurements of dentin by dual-energy radiography. *J. Dent. Edu.* 109 (4):604-14.

Herrera-Urbina, R. 2003. Recent developments and advances in formulations and applications of chemical reagents used in froth flotation. *Mineral Processing and Extractive Metallurgy Review*. 24 (2): 139-182.

Herrera-Urbina, R., F.J. Sotillo,. and Fuerstenau, D.W. 1999. Effect of sodium sulfide additions on the pulp potential and amyl xanthate flotation of cerussite and galena*, Int. J. Miner. Process.* 55 (3): 157.

Hsieh, C.H. 2012. *Procedure and analysis of mineral samples using high resolution X-ray micro tomography*, MS thesis, University of Utah, Salt Lake City, Utah, USA.

Huynh, L., Feiler, A., Michelmore, A., Ralston, J., and Jenking, P. 2000. Control of slime coatings by the use of anionic phosphates, a fundamental study. *Miner. Eng.* 13 (10-11): 1059–1069.

ICSG. 2014. The world copper factbook. *International Copper Study Group*. http://www.icsg.org/ Accessed 12/20/2014.

ImageJ. 2011. Image processing and analysis in Java. *National Institutes of Health*. http://rsb.info.nih.gov/ij/index.html. Accessed 12/30/2014.

Imaizumi, T., and Inoue, T. 1963. Kinetic consideration of froth flotation. *Proceedings of the VI IMPC*. Pergamon Press, Cannes.

Kahn, S.L., and Gaskin, C. 2012. *Radiographic atlas of skeleton maturation*. Lippincott Williams & Wilkins, Thieme Medical publishers, Inc.

Kennecott Utah Copper, Rio Tinto Annual Report. http://www.kennecott.com Accessed 3/15/2014.

King, R.P. 1982. The prediction of mineral liberation from mineralogical texture. *Proceedings of XIV IMPC*. Toronto, Canada, 11-7.

King, R.P., and Schneider, C.L. 1993. An effective SEM-based image analysis for quantitative mineralogy. *KONA*. 11: 165-177.

King, R.P., and Schneider, C.L. 1998. Stereological correction of linear grade distributions for mineral liberation. *Powder Technol.* 98: 21-37

Klimpel, R.R., and Hansen, R.D. 1988. Frothers, in reagents in mineral technology. *P.*

Somasundaran, B.M. Moudgil, Marcel Dekker, New York. 385 – 409.

Klimpel, R.R., Dhansen, R, and Fee, B.S. 1986. Selection of flotation reagents for mineral flotation. In Design and installation of concentration and dewatering circuit. *Mular, AL Ed.* 26: 384-404.

Kniss, J., Kindlmann, G., and Hansen, C. 2001. Interactive volume rendering using multidimensional transfer functions and direct manipulation widgets. *Proceedings of IEEE Visualization.* 1: 255-262.

Laskowski, J.S., and Castro, S. 2008. Flotation in concentrated aqueous electrolyte solutions. *Proceedings of XI IMPC*. Antalya, Turkey, 281–290.

Lazic, P., and Calic, N. 2000. Boltzmann's model of flotation kinetics, *Proceedings of XXI IMPC.* Rome, Italia. B (8): 87-93.

Leavay, G., Smart, R., and Skinner, W.M. 2001. The impact of water quality on flotation performance. *J. S. Afr. Inst. Min. Metall.* 101.

Lehmann, L.A., Alvarez, R.E., Macovski, A., Brody, W.R., Pelc, N.J., Rieder, S.J., and Hall, A.L. 1981. Generalized image combinations in dual KVP digital radiography, *Med. Phys.* 8 (5).

Leja, J. 1982. *Surface chemistry of froth flotation*, Plenum Press. New York, 758.

Lenkovskaya, G.L., and Stepanov, B.A. 1969. Effect of the ion composition of the pulp on molybdenite floatation. *Chem. Abstr*. 71: 155-222.

Limaye, A. 2006. *Drishti-volume exploration and presentation tool.* Poster presentation. Baltimore.

Lin, C.L. 1987. *Measurement and prediction of mineral liberation during grinding*. PhD dissertation. University of Utah, Salt Lake City, Utah. USA.

Lin, C.L., and Miller, J.D. 1996. Cone beam X-ray micro tomography for three-dimensional liberation analysis in the 21st century. *Int. J. Miner. Process.* 47: 61-73.

Lin, C.L., and Miller, J.D. 2001. A new cone beam X-ray micro tomography facility for 3D analysis of multiphase material. *Proceedings of II Proceedings of VI WCIPT.* Hannover, Germany.

Lin, C.L., Hsieh, C.H., Tserendagva, T., and Miller, J.D. 2013. Dual energy rapid scan radiography for geometallurgy evaluation and isolation of trace mineral particles. *Miner Eng.* 40: 30-37.

Lin, C.L., Miller, J.D., Herbst, J.A., and Rajamani, K. 1987. Comparison of methods for the measurement of linear grade distributions in liberation analysis. *Particle and particle systems characterization*. 4, 78-82.

Lin, C.L., Miller, J.D., Hsieh, C.H., Tiwari, P., and Deo, M.D. 2010. Pore scale analysis of oil shale pyrolysis by X-ray CT and LB simulation. *Proceedings of VI WCIPT*. Beijing, China.

Liu, L., Rao, S.R., Finch, J.A. 1993. Technical note: laboratory study effect of recycle water on flotation of a Cu/Zn sulphide ore. *Miner. Eng.* 6 (11): 1183 – 1190.

Maksimov, I.I., and Emeljanov, I.I. 1983. The effect of turbulence on detachment process in the flotation pulp. *Obogascenie rud*. 2: 16-19.

Martensen, K.M. 2010. *Radiographic Image Analysis*. Elsevier Scientific Pub. Co - Health Sciences Division.

MathLab. 2012. Bioinformatics Toolbox. *User's Guide* . http://www.mathworks.com/

McAuliffe, M.J., Francois, M., and Lalonde. 2012. Medical image processing, analysis & visualization in clinical research, *Proceedings of XXVI International Symposium on Computer-Based Medical Systems National Institutes of Health*. Bethesda, Maryland.

McCullough, E.C. 1975. Photon attenuation in computed tomography. *Med Phys.* 2: 307-320.

Mckinsey Global Institute, Preparing for China's urban billion. Accessed 3/1/2009.

Medina, J.H. 2012. *Liberation-limited grade/recovery curves for auriferous pyrite ores as determined by high resolution X-ray Microtomography*. PhD dissertation. University of Utah.

Miller, J.D. 2012. Advances in X-ray tomography in the processing of mineral resources, *Proceedings of XXVI IMPC.* New Delhi, India

Miller, J.D., and Lin, C.L. 1988. Treatment of polished section data for detailed liberation analysis. *Int. J. Miner. Process.* 22: 41-58.

Miller, J.D., and Lin, C.L. 2004. Three-dimensional analysis of particulates in mineral processing systems by cone-beam X-ray micro tomography, *Minerals and Metallurgical Processing.* 21: 113-124.

Miller, J.D., and Lin, C.L. 2009. High resolution X-ray micro CT (HRXMT) – advances in 3D particle characterization for mineral processing operations. *Mineral processing plant design.* Ventana Canyon Resort, Tucson, Arizona.

Miller, J.D., and Lin, C.L. 2013. 3D characterization, analysis, and simulation of multiphase systems using high resolution X-ray micro tomography. *First International Meeting*, *Metallurgy*, Lima, Peru.

Miller, J.D., and Lin, C.L., Al-Wakeel, M.I., Hupka, L. 2009. Liberation-limited grade/recovery curves from X-ray micro CT analysis of feed material for the evaluation of separation efficiency, *Int. J. Miner. Process*. 93 (1): 48–53.

Miller, J.D., Lin, C.L., Videla, A., and Medina, J.H. 2009. Three dimensional liberation analysis of feed and products from copper flotation circuits using high-resolution X-ray micro CT (HRXMT). *Proceedings of VI IMPC*. Santiago, Chile.

Mineral Resources Authority of Mongolia. 2012. Industrial minerals and selected rare metals in Mongolia. *Investor's guide*.

Mineral Resources Authority of Mongolia. 2012. Mongolia—the land of opportunities: Ulaanbaatar, Mongolia. *Mineral Resources Authority of Mongolia*, 30.

Minitab Statistical Software Features-Minitab. Software for statistics, process improvement. http://www.minitab.com/en-US/products/minitab/. Accessed 4/11/2011.

MIPAV, 2007. Medical image processing, analysis and visualization, *National Institutes of Health*, http://mipav.cit.nih.gov/.

Mongolian Extractive Industries Transparency Initiative, 2010. *Proceedings of V EITI Reconciliation Report.* Ulaanbaatar, Mongolia, http://www.eitimongolia.mn.

Muganda, S., Zanin, M., and Grano, S.R. 2011. Influence of particle size and contact angle on the flotation of chalcopyrite in a laboratory batch flotation cell. *Int. J. Miner. Process.* 98 (3-4): 150-162.

Muzenda, E. 2010. An investigation into the effect of water quality on flotation performance, *Proceedings of WASET* 45: 237-241.

National Institutes of Health. *Image processing and analysis in Java.* http://rsbweb.nih.gov/ij/. Accessed 5/24/2014

National Statistical Office of Mongolia, 2012, Monthly bulletin of statistics. *National Statistical Office of Mongolia*, December, 133p.

Naydenov, S.V., and Ryzhikov,V.D. 2002. Determining chemical compositions by method of multi-energy radiography. *Technical Physics Letters*. 28: 357-360.

Naydenov, S.V., and Ryzhikov,V.D. 2003. Multi-energy techniques for radiographic monitoring of chemical composition: theory and applications. *Nuclear Instrum*

and Meth. A (505): 556-558.

Naydenov, S.V., Ryzhikov,V.D., and Seminozhenko,V.P. 2002. Multi-energy approach in non-destructive testing of functional materials. *Reports of NANU*. 11: 95-100.

Naydenov, S.V., Ryzhikov,V.D., and Smith, C.F. 2003. Direct reconstruction of the effective atomic number of materials by the method of multi-energy radiography. *Nuclear Instrum and Meth.* B (215): 552-560.

Naydenov, S.V., Ryzhikov,V.D., and Smith, C.F. 2006. Multi-energy ZnSe-based radiography against terrorism: theory and experiments. *Proceedings of SPIE 6319*. A1-A8.

Nelson, S. 2007. Kennecott Utah Copper. Internal email communication.

NIST (National Institute of Standards and Technology)

Nowotny, R. 1998, XMuDat: photon attenuation data on PC, *Tech. Rep. IAEA*. Vienna, Austria, https://www-nds.iaea.org/publications/iaea-nds/iaea-nds-0195.htm.

Peng, Y., and Grano, S. 2010. Effect of iron contamination from grinding media on the flotation of sulphide minerals of different particle size. *Int. J. Miner. Process.* In press. Corrected proof.

Raghavan, S., and Hsu, L.L. 1984. Factors affecting the flotation recovery of molybdenite from porphyry copper ores. *Int. J. Miner. Process*. 12(1–3): 145–162.

Ralph., and Chau. 1993. *Jolyon & Katya Ralph's Mindat Home Page***.** Online database, http://en.wikipedia.org/wiki/mindat.org.

Rao, S.R., and Finch, J.A. 1989. A review of water re-use in flotation. *Miner. Eng.* 2 (1): 65–85.

Rasband, W.S. 1997-2014. *ImageJ, U. S. National Institutes of Health*, Bethesda, Maryland, USA, http://imagej.nih.gov/ij/.

Rey, M., and Raffinot, P. 1966. Flotation of ore in seawater: high frothing, soluble xanthate collecting. *World. Min.* 18.

Rio Tinto Annual Report. 2014. http://www.riotinto.com/annualreport2013/ Accessed 3/5/2014.

Rio Tinto. 2014. *Copper fact sheet*, Rio Tinto, Eastbourne Terrace, London, United Kingdom.

Roman, L.A. 2008. *Limitations to recovery in the flotation of sulfide ores*. MS thesis, University of Utah, Salt Lake City, Utah, USA.

Runge, K.C., Dunglison, M.E., Manlapig, E.V., and Franzidis, J.P. 2001. Floatability component modeling–a powerful tool for flotation circuit diagnosis. *Proceedings of the IV UBC-McGill-UA*, 93-107.

Runge, K.C., McMaster, J.K., Ijsselstijn, M., and Vien, A. 2007. Establishing the relationship between grind size and flotation recovery using modeling techniques. *Proceedings of IMPC.* Cape Town.

Ryzhikov V.D., Naydenov S.V., Grinyov B.V., Lisetskaya E.K., Kozin D.N., Opolonin A.D., and Starzhinskiy N.G. 2003. Multi-energy radiography on the basis of scintillator–photodiode detectors. *Nuclear Instrum and Meth.* 549–551.

Santana, R.C. 2008. Influence of particle size and reagent dosage on the performance of apatite flotation, *Separation and Purification Technology*. 64: 8-15.

Schena, G., Chiaruttini, C., Dreossi, D., Olivo, A., and Pani, S. 2002. Grade of fine composite mineral particles by dual-energy X-ray radiograph. *Int. J. Miner. Process.* 67: 101-122.

Schena, G., Dreossi, D., Montanari, F., Olivo, A., and Pani, S. 2003. Multiple-energy X-ray radiography and digital subtraction for a particle-composition sensor. *Miner. Eng.* 16: 609-617.

Schneider, C.L. 1995. *Measurement and calculation of liberation in continuous grinding circuits.* Ph.D dissertation, University of Utah.

Schneider, C.L. 2003. Prediction of liberation from unbroken 3-phase texture: a case study on a coal sample, *Proceedings of XXII IMPC*.

Senior, G.D., and Trahar, W.J. 1991. The influence of metal hydroxides and collector on the flotation of chalcopyrite. *Int. J. Miner. Process.* 33: 321–341

Shirley, J.F., and Sutulov, A. 1985. By-product molybdenite. Weiss, N.L. (Ed.), *SME Mineral Processing Handbook.* AIME, New York, 16-17 and 16-36.

Sillitoe, R., and Petersen, R. 1996. *Andean copper deposits: New discoveries, mineralization, styles and metallogeny*. Littleton, CO, USA.

SME, 2012, *Theory and practice of sampling particulate materials*. Elsevier Scientific Pub. Co.

SNL-Metals Economic Group. 2013. Worldwide exploration trends. http://go.snl.com/rs/snlfinanciallc/images/MEG_WETbrochure2013.pdf.

Accessed 10/22/2014.

SolGold. 2014. *SolGold Annual Report*. http://www.solgold.com.au/page/investor-centre/annual-reports/. Accessed 11/07/2014.

Spevak, P. 1993. *Chemistry of molybdenum oxide and sulphide surfaces*. PhD dissertation, University of Western Ontario.

Sutherland, D.N. 1998. Application of quantitative process mineralogy through the mining cycle, *Proceedings of AusIMM Annual Conference - 98*. Mount Isa, 333 – 337.

Szatkowski, M., and Freyberger, W.L. 1985. A model describing mechanism of flotation process. *Transactions of the Institution of Mining and Metallurgy*. C (94): C129-C135.

Szatkowski, M., and Freyberger, W.L. 1985. Kinetics of flotation with fine bubbles. *Transactions of the Institution of Mining and Metallurgy*. C (94): C61-C70.

Taylor, P.R., Spiller, E., Levier, M., and Melhotra, D. 2009. 3D Particle characterization for mineral processing operations. *Recent advances in Mineral Processing Plant Design.* SME: 48-59.

Trahar, W.J. 1981. A rational interpretation of the role of particle size in flotation. *Int. J. Miner. Process.* 8: 289–327.

Trahar, W.J., and Warren, L.J. 1976. The floatability of very fine particles-a review, *Int. J. Miner. Process.* 3: 103-131.

Triffett, B., and Bradshaw, D. 2008. The role of morphology and host rock lithology on the flotation behavior of molybdenite at Kennecott Utah Copper. *AusIMM Publication Series, Proceedings of IX ICAM.* 465-473.

Triffett, B., Veloo.C., Adair,B.J.I., and Bradshaw, D. 2008. An investigation of the factors affecting the recovery of molybdenite in the Kennecott Utah Copper bulk flotation circuit, *Miner. Eng.* 21: 832–840.

US patent. 2000. Method and an apparatus for analyzing a material. Technological Resources Pty Limited. http://patents.com/us-6122343.html. Accessed 2/15/2015.

USGS, 1996-2014. Copper statistics and information for nation.

Van Geet, M., Swennen, R., and David, P. 2001. Quantitative coal characterization by means of micro focus X-ray computer tomography, color image analysis and back scatter scanning electron microscopy. *Int. J. Coal. Geol.* 46: 11-25.

Vanangamudi, M., and Rao, T.C. 1986. Modeling of batch coal flotation operation. *Int. J. Miner. Process.* 16: 231-243

Videla R., Lin C.L., and Miller J.D. 2003. Watershed functions applied to a 3D image segmentation problem for the analysis of packed particle beds. *Part. Syst. Charact.* 23: 237-245.

Videla R., Lin C.L., and Miller J.D. 2007. 3D characterization of individual multiphase particles in packed particle beds by X-ray microtomography (XMT). *Int. J. Miner. Process.* 84: 321-326.

Wagner, C.D., Gale, L.H., and Raymond, R.H. 1979. Two-dimensional chemical state plots: a standardized data set for use in identifying chemical states by X-ray photoelectron spectroscopy. *Anal. Chem.* 51: 466-482.

Wei, Y.H., Zhou, G.Y., and Roelf, F.S. 2006. Effects of recycled water on flotation of a complex sulphide ore. *Nonferrous Met.* 58 (2): 82–85.

Wills, B.A., and Napier-Munn, T.J. 2006. *Mineral processing technology.* VII Ed. Butterworth-Heinemann, Oxford, United Kingdom.

World Bank. 2012, Mongolia quarterly economic update: Washington, DC. *The World Bank*, February 31.

XRadia. 2010. *MicroXCT-200 and MicroXCT-400 User's Guide*. 283-284.

Yates, J.T., Jr. 1998. *Experimental innovations in surface science - a guide to practical laboratory methods and instruments*. Springer, New York.

Yin, X., Gupta, V., Du, H., Wang, X., and Miller, J.D. 2012. Surface charge and wetting characteristics of layered silicate minerals. *Advances in Colloid and Interface Science*. 179: 43-50

Zanin, M. 2008. Increasing copper and molybdenum recovery from low recovery ores. *Final report for KUC*.

Zanin, M., Ametov, I Grano, S., Zhou, L., and Skinner, W. 2009. A study of mechanisms affecting molybdenite recovery in a bulk copper and molybdenum flotation circuit. *Int. J. Miner. Process.* 93: 256-266.

Zanin, M., Wightman, E., Grano, S.R., and Franzidis, J.P. 2009. Quantifying contributions to froth stability in porphyry copper plants. *Int. J. Miner. Process*. 91: 19–27.

Zhou, L., 2010. *Molybdenite flotation.* PhD dissertation, University of South Australia.